Neutrino Oscillation Parameters from ν_e Appearance in the T2K Experiment

Abigail V. Waldron

St. Catherine's College, Oxford



Thesis submitted in partial fulfilment of the requirements for the degree of Doctor of Philosophy at the University of Oxford

Trinity Term, 2012

Neutrino Oscillation Parameters from ν_e Appearance in the T2K Experiment

Abigail V. Waldron
St. Catherine's College, Oxford

Thesis submitted in partial fulfilment of the requirements for the degree of Doctor of Philosophy at the University of Oxford

Trinity Term, 2012

Abstract

The T2K Experiment is a long-baseline accelerator neutrino oscillation experiment, whose primary aim is to look for ν_e appearance in a ν_μ beam. A predominantly ν_μ beam is produced at J-PARC in Tokai on the east coast of Japan, and neutrino interactions are measured both by a near detector complex, 280 m from the neutrino production target, and by a large water Čerenkov detector, Super-Kamiokande, 295 km away. This thesis is concerned with oscillations $\nu_\mu \rightarrow \nu_e$, within both a standard three neutrino model and a model in which there is one additional sterile neutrino.

By looking at ν_e appearance over the T2K baseline, this thesis looks for oscillations involving one additional sterile neutrino. A region of the short baseline neutrino oscillation parameter space favoured by other experiments is excluded at $3\,\sigma$.

The ND280 is also used to search for ν_e appearance over a short baseline. A ν_e selection is developed, and limits on the short baseline oscillation parameter space are set. Sensitivity predictions are also made for future T2K running. The T2K ND280 is interesting for this work since the detector technology is different to that of other experiments that have seen indications of short baseline electron-neutrino appearance.

In the standard three-flavour neutrino oscillation picture, a combined analysis of the electron-neutrino appearance results of T2K and another long-baseline accelerator neutrino experiment, MINOS, is presented. Combining the two results with the Feldman-Cousins method results in $\sin^2 2\theta_{13} = 0$ being excluded at $2.7\,\sigma$, assuming the normal neutrino mass hierarchy.

Declaration

I declare that this thesis and the work presented in it are my own and were produced by me as the result of my own original research. The work was done while a candidate for a degree at the University of Oxford, and has not been submitted for any other qualification. Results and figures from published works have been clearly attributed.

I developed the calibrations described in Chapter 4, which are now used to calibrate all of the ND280 off-axis TRIP-t subdetectors' electronics. The analysis presented in Chapter 5 is my own, but the electron neutrino selection criteria used were developed by others. I developed the ND280 ν_e selection in Chapter 6, but the ND280 reconstruction used was developed by others. The analysis in Chapter 7 was performed by myself, Martin Haigh and Alfons Weber and has been published in [137].

Acknowledgements

During the four years of my D. Phil I have come into contact with many inspirational people, and made many friends who have helped me through it! I can't possibly list everyone, but will make the attempt anyway, as is traditional.

First, of course, I'd like to thank my family, Mum, Dad and James, for all their love and support.

I couldn't have hoped for a better D. Phil supervisor than Alfons Weber. He has taught me so much, given me fantastic opportunities and also allowed me the space to run with my own ideas. I'd also like to thank Giles Barr, who has always been very generous with his time.

I was really lucky to arrive into the "Oxford MINOS Office", as Phil helpfully reminded us every time the phone rang. Gemma, Phil, Chris and Rebekah quickly became not only my office mates but great friends. A large fraction of what I know about physics can be attributed to the twice daily long coffee breaks!

Later the Oxford T2K group gained two great post docs, Martin and Helen, who quickly became my close friends. Martin in particular deserves thanks for taking over my calibration duties and allowing me to work on the analysis needed to finish this thesis.

I'd also like to thank Antonin for employing me as a post doc for 3 months during my D. Phil, giving me the opportunity to break the containment of a large neutron source...

A huge thank you to Lee and Steve for letting me, as an over-excited first year, take a big part in the test beam at CERN. Also to Phill for all his help and encouragement (except for assigning me to be database expert - you're still not forgiven!).

There are a few other people on T2K who have been especially supportive, here I would like to thank Istvan, Morgan, Christos, Kendall and Sarah.

I'd also like to thank those that came earlier and without whom I may never have made it to start a D. Phil: Dr Pullen, my inspirational high school maths teacher, and my undergraduate physics tutors, especially Dave Green and Karl Sandeman.

Lastly of course I have to thank all of my other physicist and non-physicist friends and the Oxford tango community for keeping me as close to sane as possible during these four years!

Contents

1 Introduction **1**

1.1 Outline of this Thesis 1

1.2 Acronyms in this Thesis 3

2 Neutrino Physics **5**

2.1 Neutrinos 5

2.2 Neutrino Oscillations 8

2.2.1 The Solar Neutrino Problem 8

2.2.2 Evidence for Neutrino Oscillations from SNO 9

2.3 Theory of Neutrino Oscillations 11

2.3.1 Two Flavour Approximation 15

2.3.2 Matter Effects 16

2.4 Atmospheric Neutrino Oscillations 18

2.4.1 Super-Kamiokande 18

2.4.2 Long-Baseline Accelerator Neutrino Experiments 19

2.4.3 Non-zero θ_{13} 21

2.4.4 $\mathcal{CP}$-Violation 22

2.5 Sterile Neutrinos 23

2.5.1 The LSND Anomaly 24

2.5.2 The Reactor Antineutrino Anomaly 26

2.5.3 The Gallium Anomoly 28

2.6 Non-Oscillation Neutrino Physics 29
2.6.1 Neutrino Mass Measurements from Decays 30
2.6.2 Neutrinoless $\beta\beta$-Decay 31
2.6.3 Neutrino Velocity Measurements 33

3 The T2K Experiment **36**
3.1 Overview of Experimental Setup 36
3.2 Neutrino Beam 38
3.2.1 The Off-Axis Technique 39
3.3 The Near Detectors: ND280 and INGRID 41
3.3.1 INGRID 41
3.3.2 ND280 43
3.3.3 Scintillator Read-Out 48
3.4 The Far Detector: Super-Kamiokande 50
3.4.1 Particle Identification from Čerenkov Radiation 51
3.5 Monte Carlo Simulation 52
3.6 T2K Physics 54
3.6.1 Electron Neutrino Appearance: The Search for θ_{13} 54
3.6.2 Muon Neutrino Disappearance: Precision Measurement of θ_{23} and Δm^2_{32} 55

4 ND280 TRIP-t Electronics Calibration **60**
4.1 The TRIP-t Electronics 60
4.2 Pedestal Subtraction 63
4.2.1 Variation of Pedestal 67
4.2.2 Pedestal Calibration Strategy 70
4.3 Non-Linearity Calibration 71
4.3.1 Switching Between High and Low Gain Channels 79

5 Far Detector ν_e Appearance from Short Baseline Oscillations **81**

5.1 Possible Models for Including Sterile Neutrinos 81

5.2 Theory of Sterile Neutrino Mixing 84

5.2.1 $P(\nu_\mu \to \nu_e)$ for LSND L/E 87

5.2.2 $P(\nu_\mu \to \nu_e)$ for Long Baseline with $\theta_{13} = 0$ 88

5.2.3 $P(\nu_\mu \to \nu_e)$ for Long Baseline with $\theta_{13} \neq 0$ 88

5.3 T2K $\nu_\mu \to \nu_e$ Analysis 89

5.3.1 Super-Kamiokande ν_e Reconstruction 90

5.3.2 Energy Reconstruction 92

5.3.3 Total Backgrounds 93

5.4 Implementation of 3+1 Neutrino Oscillations 95

5.4.1 Matter Effects between Active and Sterile Neutrinos 95

5.5 Oscillation Probabilities for Different Δm^2_{LSND} and $\sin^2 2\theta_{\text{LSND}}$ . . . 96

5.5.1 Degeneracy between θ_{14} and θ_{24} 97

5.5.2 Constraint from $P(\nu_\mu \to \nu_\mu)$ at the ND280 101

5.6 Excluding models in terms of N_{exp} 101

5.6.1 Signal Shapes and Systematic Errors 102

5.7 Results 104

6 Near Detector ν_e Appearance from Short Baseline Oscillations **108**

6.1 Motivation for $\nu_\mu \to \nu_e$ Search using the ND280 108

6.2 ND280 Tracker ν_e Reconstruction 109

6.2.1 Efficiency to Reconstruct and Select Events 116

6.2.2 Energy Reconstruction 117

6.3 Dataset 117

6.4 Selection Results 119

6.5 Oscillation Probabilities for Different Δm^2_{LSND} and $\sin^2 2\theta_{\text{LSND}}$ . . . 121

6.6 Systematic and Statistical Errors 125

6.7 Results 126
6.8 Future Sensitivity and Possible Improvements 129

7 Combined MINOS and T2K Standard ν_e Appearance Analysis 134
7.1 Motivation 134
7.2 The T2K ν_e Appearance Measurement 135
7.3 The MINOS ν_e Appearance Measurement 136
7.4 The Feldman-Cousins Method 138
7.4.1 Inputs from MINOS and T2K 143
7.4.2 Toy Experiment Generation 144
7.4.3 The Likelihood Function 148
7.5 Considerations for the Combination 151
7.5.1 Oscillation Parameters and the Choice of x-Axis 151
7.5.2 Systematic Errors in the Likelihood Function 152
7.5.3 Combining Correlated Systematic Errors 153
7.6 Reproducing the Individual Results 156
7.7 Combined Fit Results 157
7.7.1 Significance of Excluding $\sin^2 2\theta_{13} = 0$ 159
7.7.2 Finding the Limits on $\sin^2 2\theta_{13}$ 159
7.7.3 Working out Significance of Mass Hierarchy Preference . . 161
7.7.4 Comparison to fixed $\Delta \log \mathcal{L}$ Elevation Contours 161
7.8 Inclusion of Other Experiments 162

8 Summary and Outlook 164

List of Figures

2.1 Hadron Production Cross-Section from LEP 7
2.2 SSM Solar Neutrino Flux Predictions 9
2.3 Schematic of SNO 11
2.4 Super-Kamiokande Oscillation Deficit 18
2.5 Super-Kamiokande Atmospheric Oscillation Contours 19
2.6 Combined LSND and KARMEN Allowed Parameter Space 26
2.7 MiniBooNE Results 27
2.8 The Reactor Antineutrino Anomaly 28
2.9 Electron Energy Spectrum from Tritium β-Decay 31

3.1 Schematic of the T2K Experiment 37
3.2 The T2K Neutrino Beamline 38
3.3 Neutrino Energy against Parent Pion Energy at Different Off-Axis Angles 40
3.4 Effect of Changing Off-Axis Angle 40
3.5 A Diagram of INGRID 42
3.6 A Neutrino Event in INGRID 43
3.7 Schematic of the T2K ND280 44
3.8 A Schematic of the PØD 46
3.9 Energy Loss of Different Particles in the TPC 47
3.10 Schematic of the TPC 48

3.11 A Photo of an MPPC 49
3.12 Schematic of Super-Kamiokande 51
3.13 Typical ν_μ Event in Super-Kamiokande 52
3.14 Typical ν_e Event in Super-Kamiokande 53
3.15 T2K Sensitivity to θ_{13} as a Function of Protons on Target 55
3.16 T2K ν_e Run 1+2 Appearance Result 56
3.17 T2K ν_e Run 1+2+3 Candidates 57
3.18 T2K ν_e Run 1+2+3 Appearance Result 58
3.19 T2K ν_μ Disappearance Result 59

4.1 Photo of TFB: Top and Bottom Views 61
4.2 Schematic of TFB Channel Pair 62
4.3 High and Low Gain Pedestals 64
4.4 Pedestals in Beam and Cosmic Trigger Modes 66
4.5 Pedestals in Different Cosmic Trigger Readout Cycles 67
4.6 Results of Applying the Pedestal Subtraction 68
4.7 Temperature Variation of Pedestals 69
4.8 Time Variation of Pedestals over Ten Hours 70
4.9 Demonstration of Pedestal Drift Correction 72
4.10 Non-Linearity of TFB Charge Response 73
4.11 Spread of Non-Linearity Curves and Cross-Talk 75
4.12 Charge Injection Circuit not Reacting to Low Inputs 76
4.13 Low and High Gain Non-Linearity Fits 77
4.14 Residuals from Non-Linearity Fits 78
4.15 Relationship between Linearised ADC for High and Low Gain Channels 79
4.16 Linearised ADC for a Cosmic Run 80

5.1 The MiniBooNE Joint Neutrino and Antineutrino Data Allowed Regions 83
5.2 Charged Current Neutrino Event Rates at the T2K Far Detector . 89
5.3 Efficiency for CC ν_e Reconstruction 92
5.4 Relationship between True and Reconstructed Neutrino Energy . 94
5.5 Total Backgrounds for Run 1+2 $\nu_\mu \to \nu_e$ Search 94
5.6 $P(\nu_\mu \to \nu_e)$ for SK ($\sin^2 2\theta_{13} = 0.089$) 96
5.7 $P(\nu_\mu \to \nu_e)$ for SK, MiniBooNE Best Fit 98
5.8 $P(\nu_\mu \to \nu_e)$ for SK with MiniBooNE Best Fit to Neutrino Data only 99
5.9 $P(\nu_\mu \to \nu_e)$ with 3+1 Neutrinos, with $\sin^2 2\theta_{13} = 0., 0.089$ 100
5.10 Example signals from Three and Four Flavour Neutrino Oscillations, True Energy, no Efficiency Correction 102
5.11 Example signals from Three and Four Flavour Neutrino Oscillations, True Energy 103
5.12 Example signals from Three and Four Flavour Neutrino Oscillations 104
5.13 Values of $\Delta \log \mathcal{L} - \Delta \log \mathcal{L}_{\text{crit}}$ in terms of Expected ν_e Candidates at SK 105
5.14 Maximum and Minimum N_{exp} as a Function of the LSND Oscillation Parameters 106
5.15 T2K Confidence Limits on LSND Oscillation Parameter Space from $\nu_\mu \to \nu_e$ 107

6.1 TPC Electron and Muon Pulls for True CCQE ν_e Events 111
6.2 TPC Electron and Muon Pulls for True CCQE ν_μ Events 112
6.3 PID Cut in TPC Electron and Muon Pulls 112
6.4 Invariant Mass of e^+e^- Reconstructed Pairs 114
6.5 Reconstructed Mass Distributions for Signal and Background . . 115

6.6 Reconstruction and Selection Efficiency for all CC ν_e Interactions in the FGDs . . . 116
6.7 Relationship between True and Reconstructed Neutrino Energies for CCQE and CC non-QE ν_e Interactions in the FGDs . . . 118
6.8 Spectra of Different Background Event Predictions and Data ν_e Candidates . . . 120
6.9 Spectra of Different Background Event Predictions and Data ν_e Candidates without the Upstream Veto . . . 121
6.10 Spectra of Different Background Event Predictions and Data ν_e Candidates without the PID . . . 122
6.11 $P(\nu_\mu \to \nu_e)$ for ND280, MiniBooNE Best Fit . . . 123
6.12 Expected Numbers of ν_e Candidates at the ND280 for Run 2 . . . 124
6.13 Uncertainty in Expected Number of ν_e Candidates . . . 127
6.14 Limit on Short Baseline Oscillations $\nu_\mu \to \nu_e$ from T2K ND280 ν_e Appearance . . . 130
6.15 ND280 Future Sensitivity to Short Baseline Oscillations $\nu_\mu \to \nu_e$, 90% CL . . . 132
6.16 ND280 Future Sensitivity to Short Baseline Oscillations $\nu_\mu \to \nu_e$, 99% CL . . . 133

7.1 T2K ν_e Appearance Result . . . 136
7.2 Schematic of MINOS Baseline . . . 138
7.3 Image of MINOS Far Detector . . . 139
7.4 MINOS ν_e Candidates . . . 140
7.5 MINOS ν_e Results . . . 141
7.6 T2K Expected ν_e Candidates . . . 144
7.7 Example of a Covariance Matrix for Combined Fit . . . 145
7.8 Calculation of Critical Value of $\Delta \log \mathcal{L}$ . . . 149

7.9 Critical values of $\Delta \log \mathcal{L}$ 149
7.10 Plot of $\Delta \log \mathcal{L}_{\text{data}}$ 151
7.11 Plot of $\Delta \log \mathcal{L}_{\text{data}} - \Delta \log \mathcal{L}_{\text{crit}}$ 152
7.12 Effect of Including a Correlated Cross-Section Error 155
7.13 Reproduction of the T2K Results 156
7.14 Reproduction of the MINOS Results 157
7.15 Combined Fit Results 158
7.16 Effect of Taking Profile Likelihood over δ 160
7.17 Comparison to Fixed $\Delta(2 \log \mathcal{L})$ Elevation Contours 162
7.18 Difference between Critical and Fixed $\Delta(2 \log \mathcal{L})$ Elevations 163

List of Tables

6.1 Summary of T2K Run Periods 119
6.2 Relative Cross Section Errors for Different Neutrino Interaction Modes 125

Chapter 1

Introduction

This thesis is concerned with neutrino oscillations, in particular oscillations from muon neutrinos (ν_μ) into electron neutrinos (ν_e). The Tokai to Kamioka (T2K) experiment was designed to search for oscillations of this kind. A beam of mostly muon-type neutrinos is produced on the east coast of Japan in Tokai, where it is sampled by near detectors after 280 m, before travelling 295 km across Japan to the far detector, Super-Kamiokande. An excess of electron-neutrino like events in Super-Kamiokande implies $\nu_\mu \rightarrow \nu_e$ neutrino oscillations.

1.1 Outline of this Thesis

This thesis begins with a brief history of neutrino physics, with particular emphasis on the discovery of neutrino oscillations. Aspects of the theory of neutrino oscillations relevant to the topics in this thesis will also be presented in Chapter 2.

The T2K experiment, including the neutrino beam, the near and far detectors and the Monte Carlo simulations, is described in Chapter 3. The main physics analyses ($\nu_\mu \rightarrow \nu_e$ appearance and ν_μ disappearance) are also described

at the end of this chapter and the latest results are summarised.

A detailed description of the T2K near detector electronics follows in Chapter 4, including details of work done by the author to calibrate the electronics. Two calibrations are discussed in particular: the pedestal subtraction and the correction for the non-linearity of the electronics' response to input charges.

Short-baseline oscillations $\nu_\mu \rightarrow \nu_e$ and $\overline{\nu}_\mu \rightarrow \overline{\nu}_e$, if they exist, could cause a ν_e appearance signal to be seen, even without standard neutrino oscillations. The differences in the far detector electron neutrino appearance spectra that could be expected between standard neutrino oscillations and those driven by an additional sterile neutrino will be discussed in Chapter 5. The T2K long-baseline electron-neutrino appearance results will be used to place limits on the short baseline neutrino oscillation parameter space for the case where there is one sterile neutrino.

A search for short-baseline ν_e appearance in the T2K beam, due to short baseline neutrino oscillations $\nu_\mu \rightarrow \nu_e$, using the ND280 is presented in Chapter 6. Sensitivity plots for the projected future running of T2K are also shown.

In Chapter 7 the ν_e appearance results from T2K and MINOS are combined using the Feldman-Cousins method, to get combined confidence intervals on the parameters governing ν_e appearance in the standard neutrino oscillation model, $\sin^2 2\theta_{13}$ and δ. An investigation of whether this combination gives any significant information about the neutrino mass hierarchy is also performed. Finally, the possible inclusion of other experiments in such a combination is discussed.

The main contributions of the author to the T2K experiment are the calibration of the ND280 TRIP-t electronics, presented in Chapter 4, and the sterile neutrino analyses, presented in Chapters 5 and 6.

1.2 Acronyms in this Thesis

Many acronyms are used throughout this thesis, particularly in the description of the ND280 electronics. Those most commonly used are summarised here:

- **T2K** Tokai to Kamioka
- **SK, Super-K** Super-Kamiokande
- **ND280** Near Detector at 280 m. Predominantly used to describe the off-axis part of the detector complex, but can also mean the whole complex including INGRID.
- **INGRID, PØD, ECal, SMRD, FGD, TPC** ND280 sub-detectors, described in Chapter 3.
- **PØD** π^0 Detector
- **ECal** Electro-magnetic Calorimeter
- **SMRD** Side Muon Range Detector
- **FDG** Fine-Grained Detector
- **TPC** Time Projection Chamber
- **MPPC** Multi-Pixel Photon Counter
- **TFB** TRIP-t Frontend Board
- **RMM** Readout Merger Module
- **DAQ** Data AcQuisition
- **DPT** Data Processing Task
- **ADC** Analogue to Digital Converter

- **PID** Particle IDentification
- **CC** Charged Current
- **NC** Neutral Current
- **CCQE** Charged Current Quasi Elastic
- **MC** Monte Carlo
- **POT** Protons On Target
- **CL** Confidence Level
- **LEM** Library Event Matching

Chapter 2

Neutrino Physics

2.1 Neutrinos

The existence of the neutrino was first suggested in 1930, by Pauli, in a letter addressing the delegates at a radioactivity conference in Tübingen [1]. Pauli proposed that an, as yet unseen, electrically neutral particle, initially called the neutron, be emitted during nuclear β-decay to preserve the conservation of energy. After Chadwick's discovery of the neutron [2, 3], Fermi renamed Pauli's neutron the neutrino [4].

The neutrino was first detected by Reines and Cowan in 1953 [5] (a result later confirmed in 1956 [6]), using reactor electron antineutrinos in the inverse β-decay, $\overline{\nu}_e + p \rightarrow n + e^+$, on a cadmium-loaded scintillator target. The prompt signal from the positron annihilation on an electron in the solution coupled with the delayed signal from the de-excitation of a cadmium nucleus following capture of the neutron (a few micro seconds later) allowed neutrino events to be tagged by observing a "delayed coincidence". The rate of such events was found to be consistent with the predicted neutrino interaction rate from the reactor.

In 1956, an experiment by Goldhaber, Grodzins and Sunyar [7] showed that

the neutrino has negative helicity. They studied decays of ^{152}Eu (spin 0) to ^{152}Sm (spin 1) via electron capture. Due to the conservation of momentum and angular momentum, the photon emitted immediately after the electron capture as the nucleus de-excites will have the same helicity as the neutrino emitted during the electron capture. The helicity of these photons was found to be negative, thus showing that the neutrino has negative helicity.

The muon neutrino was discovered in 1962 at the Brookhaven laboratory [8]. A ν_μ beam was created by colliding protons on a beryllium target and allowing the resultant charged pions to decay in flight. The pions mostly decay to ν_μ as decays to (electron)positron and electron (anti-)neutrino pairs are suppressed as the electron must be created with the wrong helicity. The muons, and remaining hadrons, were then stopped using a 13.5 m iron shield. The muon neutrinos were detected via their charged current reactions, leading to an isolated muon track, in a segmented spark chamber.

Evidence that there were three active neutrino species first came from the Z^0 width measurement at the CERN Large Electron-Positron Collider (LEP) [9]. Four different LEP experiments measured the width of the Z^0 production peak, and the branching fractions to the kinematically allowed visible final states: $q\bar{q}$ ($q = u, d, s, c, b$) and l^+l^- ($l = e, \mu, \tau$). The invisible width, assumed to be the branching fraction to neutrinos, is given by,

$$\Gamma_{\text{inv}} = \Gamma_Z - (\Gamma_{q\bar{q}} + \Gamma_{l^+l^-}) \tag{2.1}$$

Assuming that this invisible width was made up entirely of decays to neutrinos, and using the theoretically calculated neutrino branching fraction, the number of light (less than half the Z^0 mass), active neutrino species was found to be:

$$N_\nu = 2.9840 \pm 0.0082 \tag{2.2}$$

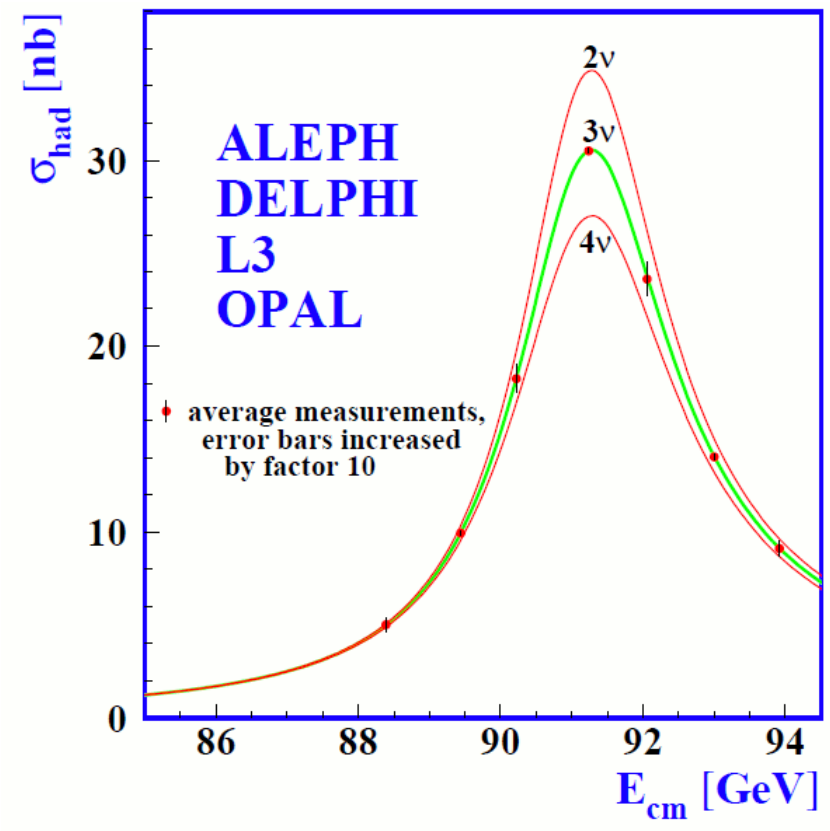


Figure 2.1: The LEP hadron production cross-section, as a function of energy, around the Z^0 production peak. Predictions for different numbers of neutrino species are shown, with the three neutrino-flavour model providing an excellent fit to the data. Image from [9]

A plot of the Z^0 width that would be expected with different numbers of neutrino species can be seen in Figure 2.1.

Evidence for a third generation of leptons, the tau and its neutrino, first came from the SLAC-LBL experiment in 1975 [10]. Events of the form $e^+ + e^- \rightarrow e^\pm + \mu^\mp +$ missing energy were observed, due to a $\tau^+\tau^-$ pair being created and decaying leptonically. Scattering of the ν_τ was first directly observed in 2001 by the DONUT experiment [11] at Fermilab. A partly ν_τ beam was produced from decays of charmed mesons created when the Tevatron beam was collided into the beam dump. Heavy shielding, consisting of magnets, concrete, iron and lead, had to be used to shield the DONUT detector, 36 m downstream, from all

the muons and hadronic debris created by the beam dump. The ν_τ were detected via their charged current interactions, which was particularly challenging as the created τ-leptons traveled less than 2 mm in the detector on average. The dominant decay mode of the τ is to a single charged daughter particle plus some number of neutral daughter particles. Due to this difficulty, the detector was made up of nuclear emulsion targets, so that the kink in the track from the τ's decay to the charged daughter particle could be imaged. DONUT observed 4 ν_τ candidates, against an expected background of 0.34 events, an event rate consistent with the Standard Model expectation.

2.2 Neutrino Oscillations

2.2.1 The Solar Neutrino Problem

Electron neutrinos are produced by nuclear fusion processes in the Sun. In the 1960s, hints started to emerge that all was not right with our understanding of neutrinos, the fusion processes inside the Sun, or both. In 1968 the Homestake experiment of Ray Davis *et al.* reported an upper limit on the interaction rate of solar neutrinos on chlorine [13] that was much lower than the predicted rate at the time [12]. Since then the flux predictions have been updated, but updated results from the Homestake Experiment [14] observed a significantly lower neutrino interaction event rate.

Quantum mechanical neutrino oscillations were first postulated in the late 1950s by Pontecorvo [16], when only the electron neutrino had been discovered. He thus suggested that oscillations $\nu_e \leftrightarrow \overline{\nu}_e$ could occur. Later, after the discovery of the ν_μ in 1962, Maki, Nakagawa and Sakata [17] proposed that neutrinos could oscillate between the different flavours.

In this new oscillation physics, the deficit of electron neutrinos observed by

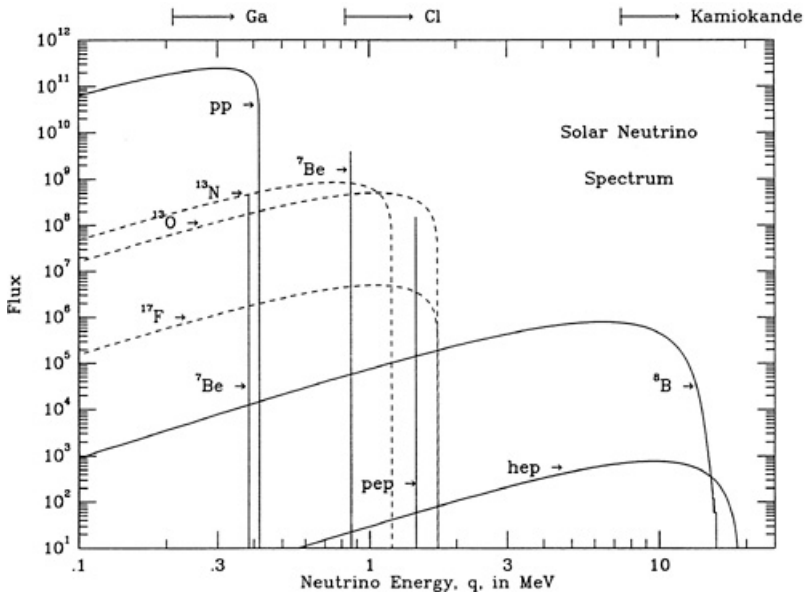


Figure 2.2: SSM Solar neutrino flux predictions [15]: flux is in units of neutrinos per square centimeter per second per MeV at 1AU, unless the process has mono-energetic neutrinos, then it is neutrinos per centimeter squared per second.

Homestake could be explained by oscillations of the solar neutrinos to a sterile neutrino, or to an active neutrino that the experiment wasn't sensitive to, *i.e.* ν_μ or ν_τ. However, it wasn't until 2002 that unambiguous evidence for neutrinos changing flavour [18] was found by the Sudbury Neutrino Observatory (SNO).

2.2.2 Evidence for Neutrino Oscillations from SNO

SNO is a heavy water Čerenkov detector located in the Creighton mine near Sudbury in Canada [19]. Their first physics run was from 1999-2001 and aimed to observe for the first time the difference between the total active neutrino flux from the Sun, via neutral current (NC) reactions, as well as the electron neutrino

flux [18]. Specifically, they studied three processes:

$$\nu_e + \mathrm{d} \rightarrow \mathrm{p} + \mathrm{p} + \mathrm{e}^- \tag{2.3}$$

$$\nu_\alpha + \mathrm{d} \rightarrow \mathrm{p} + \mathrm{n} + \nu_\alpha \tag{2.4}$$

$$\nu_\alpha + \mathrm{e}^- \rightarrow \nu_\alpha + \mathrm{e}^- \tag{2.5}$$

Where $\alpha = e, \mu, \tau$.

The experiment is very deep underground (6010 m water equivalent overburden) so there are very few cosmic muons (70/day) in the detector. In addition, the water and heavy water used were ultra-pure, and contamination in all areas of naturally occurring uranium and thorium was kept to a minimum, as deuterium break-up, caused by gammas from the thorium and uranium decay chains, was a major source of background to the neutral current reactions.

The fiducial volume is a 12 m diameter acrylic sphere holding 1000 tonnes of D_2O. Surrounding the sphere of heavy water is a light water veto of 22 m diameter and 34 m height. Within the light water is a 17.8 m diameter geodesic structure containing 9438 PMTs to detect the Čerenkov light. The setup is depicted in Figure 2.3.

Electrons (of sufficient energy) are detected as they emit Čerenkov radiation as they travel faster than the local speed of light through the heavy water. Neutrons are detected from the Čerenkov radiation of the electrons from the Compton scattering of the 6.25 MeV gamma emitted when they are absorbed on deuterium.

SNO found that the rate of NC neutrino interactions was consistent with the predictions from the Standard Solar Model, verifying that it provided a correct description of the neutrino flux from the Sun. Additionally, they, like Homestake before them, saw a significant deficit of electron neutrino interactions (the charged current interactions, Equation 2.3, were used to unambiguously mea-

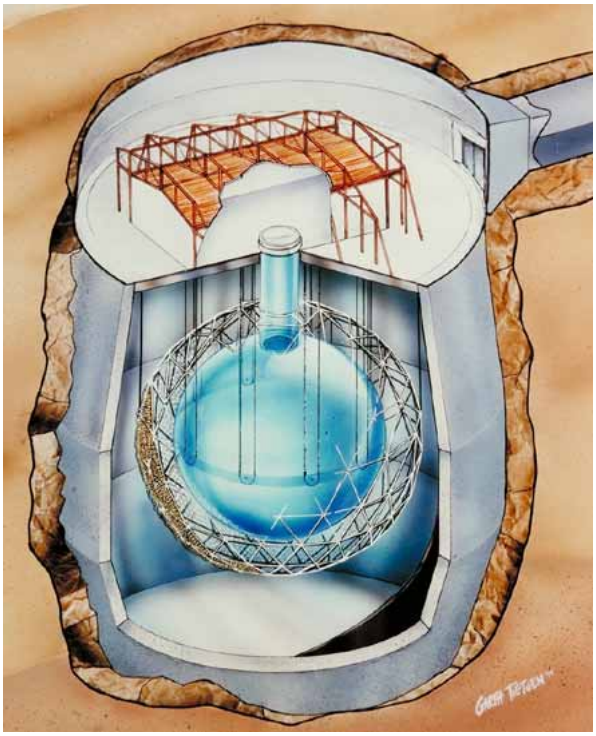


Figure 2.3: A schematic of the Sudbury Neutrino Observatory (SNO) [20]. The D_2O acrylic sphere is in blue, inside the larger volume of H_2O. The surrounding geodesic containing the PMTs is also visible.

sure this). Thus SNO provided the first direct evidence that neutrinos change flavour, the non-ν_e (*i.e.* ν_μ, ν_τ) component of the solar neutrino flux was measured to be non-zero at $5.3\,\sigma$. Earlier, Super-Kamiokande had seen evidence that ν_μ created by cosmic rays hitting the atmosphere were disappearing [31], but the total neutrino flux was not measured. This measurement is discussed in more detail in 2.4.1.

2.3 Theory of Neutrino Oscillations

It has now been established that neutrinos undergo quantum mechanical oscillations between their different flavour eigenstates. This implies that the neutrinos have non-zero mass, and that the neutrino flavour eigenstates are superpositions of the different neutrino mass eigenstates.

In this section we will derive an expression for neutrino oscillations in the vacuum, following that given in [21, 22]. It is also possible to reach the same result using a quantum field theoretic approach [23].

The neutrino flavour eigenstates (ν_e, ν_μ, ν_τ) are defined as being those that take part in charged current weak interactions, coupling to their charged lepton partners (e, μ, τ), and are a superposition of the different neutrino mass eigenstates, in which the neutrinos propagate through space, ($i = 1, 2, 3$ in the standard picture):

$$\mid \nu_\alpha \rangle = \sum_i U^*_{\alpha i} \mid \nu_i \rangle \tag{2.6}$$

Where $\alpha = e, \mu, \tau$, and the matrix U is the unitary PMNS matrix, named after Pontecorvo, Maki, Nakagawa and Sakata, which describes the relationship between the neutrino mass and flavour eigenstates. Now we want to calculate the amplitude for the flavour transition, $\nu_\alpha \rightarrow \nu_\beta$:

$$\begin{aligned} A_{\nu_\alpha \rightarrow \nu_\beta}(t) &\equiv \langle \nu_\beta \mid \nu_\alpha(t) \rangle & (2.7)\\ &= \sum_{i,\jmath} U_{\beta i} U^*_{\alpha \jmath} \Phi_\jmath(t) \langle \nu_i \mid \nu_\jmath \rangle & (2.8)\\ &= \sum_i U_{\beta i} U^*_{\alpha i} \Phi_i(t) & (2.9) \end{aligned}$$

Where $\Phi_\jmath(t)$ is the time-evolution of the $\jmath$th eigenstate. Now we need to work out the time propagation of the mass eigenstate using the Schrödinger equation:

$$i \frac{\mathrm{d}}{\mathrm{d}t} \mid \nu_i(t) \rangle = E_i \mid \nu_i(t) \rangle \tag{2.10}$$

Which gives:

$$\Phi_i(t) = e^{-iE_i t} \tag{2.11}$$

Substituting this into (2.9) and squaring to get the probability gives:

$$P_{\nu_\alpha \to \nu_\beta}(t) = \sum_{i,\jmath} U^*_{\alpha i} U_{\beta i} U_{\alpha \jmath} U^*_{\beta \jmath} e^{-i(E_i - E_\jmath)t} \tag{2.12}$$

We can re-express the neutrino energy eigenvalues in terms of mass using:

$$\begin{aligned} E_i &= \sqrt{\mathbf{p}^2 + m_i^2} && (2.13) \\ &= |\mathbf{p}| + \frac{m_i^2}{2|\mathbf{p}|} + \mathcal{O}(m_i^4) && (2.14) \end{aligned}$$

Neglecting higher order terms, and using that, in the ultra-relativistic limit, $E \gg m$, so that $|\mathbf{p}| = E$,

$$\begin{aligned} E_i - E_\jmath &= \frac{m_i^2 - m_\jmath^2}{2E} && (2.15) \\ &\equiv \frac{\Delta m^2_{i\jmath}}{2E} && (2.16) \end{aligned}$$

Then using that, in the relativistic limit, in natural units, $t = L$, we recover the neutrino oscillation probability:

$$P_{\nu_\alpha \to \nu_\beta} = \sum_{i,\jmath} U^*_{\alpha i} U_{\beta i} U_{\alpha \jmath} U^*_{\beta \jmath} e^{-i \frac{\Delta m^2_{i\jmath} L}{2E}} \tag{2.17}$$

Now, using the unitarity relation $UU^\dagger = \mathbb{1}$:

$$\sum_\jmath U_{\alpha \jmath} U^*_{\beta \jmath} = \delta_{\alpha\beta} \tag{2.18}$$

Squaring this gives:

$$\sum_k U^*_{\alpha k} U_{\beta k} \sum_\jmath U_{\alpha \jmath} U^*_{\beta \jmath} = \delta_{\alpha\beta} \tag{2.19}$$

Separating out the parts $k = \jmath$ and $k \neq \jmath$ and re-arranging gives:

$$\sum_k |U_{\alpha k}|^2 |U_{\beta k}|^2 = \delta_{\alpha\beta} - 2\sum_{k>\jmath} \Re\left[U^*_{\alpha k} U_{\beta k} U_{\alpha\jmath} U^*_{\beta\jmath}\right] \tag{2.20}$$

Now taking equation (2.17), separating out the parts $i = \jmath$ and $i \neq \jmath$, and defining $\phi_{i\jmath} \equiv \frac{\Delta m^2_{ij} L}{2E}$:

$$P_{\nu_\alpha \to \nu_\beta} = \sum_i |U_{\alpha i}|^2 |U_{\beta i}|^2 + \sum_{i\neq\jmath} \left[U^*_{\alpha i} U_{\beta i} U_{\alpha\jmath} U^*_{\beta\jmath}\right] e^{-i\phi_{i\jmath}} \tag{2.21}$$

Substituting in equation (2.20), and using $e^{-i\phi} = \cos\phi - i\sin\phi$:

$$\begin{aligned} P_{\nu_\alpha \to \nu_\beta} &= \delta_{\alpha\beta} - 2\sum_{i>\jmath} \Re\left[U^*_{\alpha i} U_{\beta i} U_{\alpha\jmath} U^*_{\beta\jmath}\right] \\ &\quad + \sum_{i\neq\jmath} \left[U^*_{\alpha i} U_{\beta i} U_{\alpha\jmath} U^*_{\beta\jmath}\right] (\cos\phi_{i\jmath} - i\sin\phi_{i\jmath}) \end{aligned} \tag{2.22}$$

Setting the imaginary parts to zero, since the probability must be real, and using that $1 - \cos\phi = 2\sin^2\frac{\phi}{2}$, we recover the standard form of the neutrino oscillation probability:

$$\begin{aligned} P_{\nu_\alpha \to \nu_\beta} &= \delta_{\alpha\beta} - 4\sum_{i>\jmath} \Re\left[U^*_{\alpha i} U_{\beta i} U_{\alpha\jmath} U^*_{\beta\jmath}\right] \sin^2\frac{\Delta m^2_{ij} L}{4E} \\ &\quad + 2\sum_{i>\jmath} \Im\left[U^*_{\alpha i} U_{\beta i} U_{\alpha\jmath} U^*_{\beta\jmath}\right] \sin\frac{\Delta m^2_{ij} L}{2E} \end{aligned} \tag{2.23}$$

The PMNS neutrino mixing matrix is usually parametrised in terms of three rotations involving three angles, θ_{12}, θ_{13} and θ_{23}, and one $\mathcal{CP}$-violating phase, δ, as follows [24]:

$$U = R_{23}(\theta_{23}) R_{13}(\theta_{13}, \delta) R_{12}(\theta_{12}) \tag{2.24}$$

$$U = \begin{pmatrix} 1 & & \\ & c_{23} & s_{23} \\ & -s_{23} & c_{23} \end{pmatrix} \begin{pmatrix} c_{13} & & s_{13}e^{-i\delta} \\ & 1 & \\ -s_{13}e^{i\delta_{13}} & & c_{13} \end{pmatrix} \begin{pmatrix} c_{12} & s_{12} & \\ -s_{12} & c_{12} & \\ & & 1 \end{pmatrix} \tag{2.25}$$

$$U = \begin{pmatrix} c_{13}c_{12} & c_{13}s_{12} & s_{13}e^{-i\delta} \\ -c_{23}s_{12} - s_{13}c_{12}s_{23}e^{i\delta} & c_{23}c_{12} - s_{13}s_{12}s_{23}e^{i\delta} & c_{13}s_{23} \\ s_{23}s_{12} - s_{13}c_{12}c_{23}e^{i\delta} & -s_{23}c_{12} - s_{13}s_{12}c_{23}e^{i\delta} & c_{13}c_{23} \end{pmatrix} \tag{2.26}$$

Where $s_{ij} = \sin\theta_{ij}$ and $c_{ij} = \cos\theta_{ij}$.

2.3.1 Two Flavour Approximation

In the case where oscillations are predominantly between two of the neutrino flavours at a given L/E, *e.g.* $\nu_\mu \leftrightarrow \nu_\tau$ at an atmospheric L/E ($\sim 500\,\text{km GeV}^{-1}$), a two flavour neutrino oscillation approximation can be made. The mixing matrix is then parametrised by a single angle, θ, and is given by:

$$U = \begin{pmatrix} \cos\theta & \sin\theta \\ -\sin\theta & \cos\theta \end{pmatrix} \tag{2.27}$$

The survival probability is then given by:

$$P_{\nu_\alpha \to \nu_\alpha} = 1 - \sin^2 2\theta \sin^2 \frac{\Delta m^2 L}{4E} \tag{2.28}$$

And the appearance probability is given by:

$$P_{\nu_\alpha \to \nu_\beta} = \sin^2 2\theta \sin^2 \frac{\Delta m^2 L}{4E} \tag{2.29}$$

2.3.2 Matter Effects

Neutrino oscillations are complicated by the presence of matter, due to the different coherent forward scattering interactions of the different neutrino flavours with the surrounding fermions. This was first suggested before neutrino oscillations had been confirmed in 1978 by Wolfenstein [25]. Whilst all active neutrino species can undergo weak neutral current scattering with the protons, neutrons and electrons in normal matter, only the electron neutrinos can scatter coherently via a weak charged current interaction. This effect can in fact lead to resonant neutrino oscillations, called the MSW effect, first suggested by Mikheyev and Smirnov in 1985 [26], the W is for Wolfenstein. Extracts from the treatments presented in [27, 28] will be presented here.

When electron neutrinos travel through matter they experience an effective potential from the electrons, given by:

$$V_m^{CC} = \pm\sqrt{2}G_F n_e \tag{2.30}$$

Where n_e is the number density of the electrons in the material. The positive sign is for ν_e, the negative sign for $\overline{\nu}_e$. When all active neutrinos travel through matter they experience a potential from coherent neutral current forward scattering, but since this is the same for all active flavours it cannot lead to resonant oscillations.

In the two flavour case, we can define the difference in the matter potentials as ΔV, *e.g.* for $\nu_e \leftrightarrow \nu_\mu$, $\Delta V = V_m^{CC} = \sqrt{2}G_F n_e$. Then the effective mixing angle between the two neutrino types in matter is given by:

$$\sin^2 2\theta_m = \frac{(\frac{\Delta m^2}{2E})^2 \sin^2 2\theta}{[\frac{\Delta m^2}{2E}\cos 2\theta - \Delta V]^2 + (\frac{\Delta m^2}{2E})^2 \sin^2 2\theta} \tag{2.31}$$

If the term in the square brackets is equal to zero, then the neutrino oscillations

in the matter will be maximal, $\sin^2 2\theta_m = 1$, regardless of the size of the oscillation probability in vacuo; this is known as the MSW effect. In general, the condition for resonance is:

$$\Delta V = \frac{\Delta m^2}{2E} \cos 2\theta \tag{2.32}$$

The observed deficit of ν_e from the Sun is caused by the MSW effect within the Sun. Neutrinos created, mostly in the core of the Sun, at different energies, travel outwards, traversing different regions of density. This means that neutrinos of all energies will undergo resonant oscillations at some point during their journey through the Sun. The solar neutrinos thus emerge maximally mixed, and any further vacuum oscillations do not change the flavour composition of the solar neutrino flux. This has been confirmed experimentally by the lack of any energy-dependent deficit in the ν_e flux observed by SNO, as would have been expected from a decreased ν_e flux solely due to vacuum oscillations [29]. Precise determination of the solar oscillation parameters is thus not possible only from observing neutrinos from the Sun; the solar neutrino oscillation parameters were determined by a reactor $\overline{\nu}_e$ experiment, the Kamioka Liquid Scintillator Neutrino Detector (KamLAND) [30]. KamLAND measured $\overline{\nu}_e$ from 55 nuclear reactors in Japan via inverse β-decay, $\overline{\nu}_e + p \rightarrow e^+ + n$. The energy range of the detected neutrinos was 20-100 MeV and the flux weighted average baseline was 180 km, giving a L/E of $\sim 3600\,\text{km GeV}^{-1}$. KamLAND found $\Delta m^2_{21} = 7.59^{+0.21}_{-0.21}\,\text{eV}^2$ and $\tan^2\theta_{12} = 0.47^{+0.06}_{-0.05}$, combining their data with results from solar experiments.

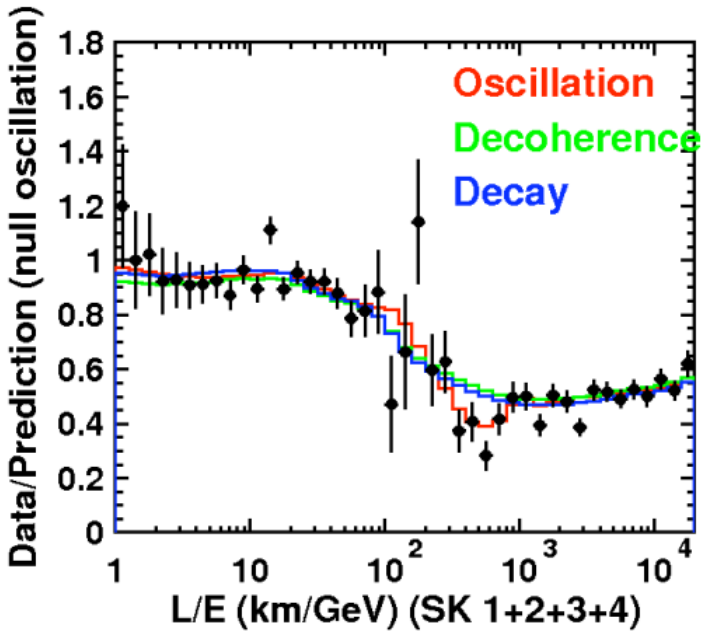


Figure 2.4: The ratio of observed to expected ν_μ in Super-Kamiokande [34] as a function of L/E. A clear oscillation dip can be seen starting at a few hundred km/GeV.

2.4 Atmospheric Neutrino Oscillations

2.4.1 Super-Kamiokande

The first evidence that atmospheric muon neutrinos, created in the upper atmosphere by incident cosmic rays, were disappearing came in 1998 from Super-Kamiokande [31]. Super-Kamiokande is a 50 kt water Čerenkov detector located under a mountain in Gifu Prefecture, Japan. Muon and electron neutrino charged-current interactions can be distinguished by the different shapes of the Čerenkov radiation rings, associated with muons and electrons, detected by the PMTs surrounding the water volume.

Super-Kamiokande saw a deficit of upward going ν_μ, *i.e.* those that had traveled all the way through the Earth, compared to the downward going ν_μ that had come straight from the atmosphere above, see Figure 2.4. No corresponding excess or deficit was seen in the flux of electron neutrinos coming from

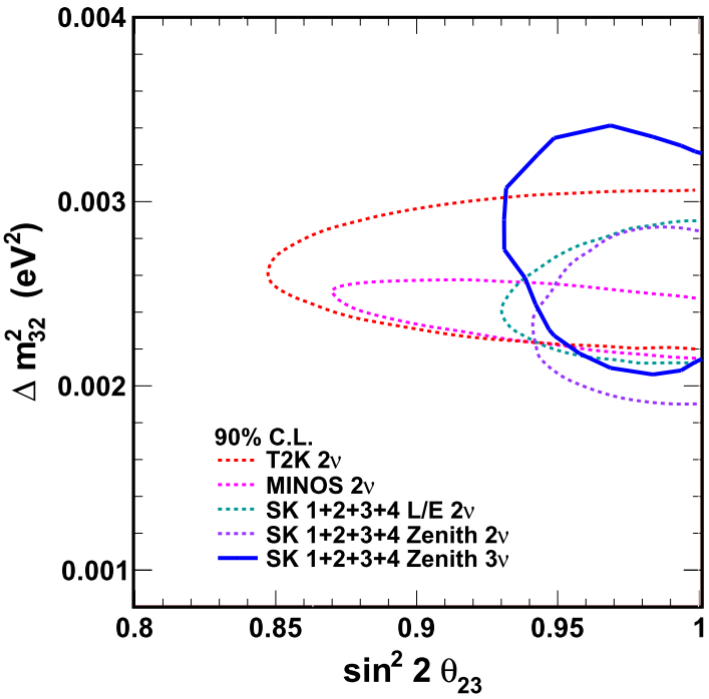


Figure 2.5: The allowed atmospheric oscillation parameter region in Super-Kamiokande [34] at 90% confidence level.

below compared to that of those coming from above. This implied that the ν_μ were disappearing as they travelled, presumably to be due to oscillations $\nu_\mu \rightarrow \nu_\tau$, although other explanations like decay were not ruled out.

Super-Kamiokande have since updated their results [32, 33, 34], see Figure 2.5. Super-Kamiokande have also shown that their data is inconsistent with no ν_τ appearance at 3.8σ [35].

2.4.2 Long-Baseline Accelerator Neutrino Experiments

More recently, the KEK to Kamioka long-baseline neutrino oscillation experiment (K2K) measured the same atmospheric L/E neutrino oscillations using an accelerator produced neutrino beam [37]. A mostly ν_μ beam was produced at KEK by colliding protons onto a target and then focusing the positively charged secondary hadrons (mostly pions) with magnetic horns. In this way it was pos-

sible to create an intense ν_μ beam, rather than a mixed ν_μ and $\overline{\nu}_\mu$ beam. The beam was directed at Super-Kamiokande, and oscillations were seen by observing a deficit of ν_μ events, as a function of reconstructed neutrino energy. They observed 112 ν_μ candidate events, against an expectation of $158.1^{+9.2}_{-8.6}$, in the null oscillation case. They rule out the null oscillation hypothesis at 4.3σ.

The MINOS experiment also uses an accelerator produced ν_μ beam to study atmospheric neutrino oscillations. A mostly ν_μ beam is produced at Fermilab (it is also possible to run the beam in mostly $\overline{\nu}_\mu$ configuration) and then sampled by two steel/scintillator magnetised tracking calorimeters, one at 1 km, and one at 735 km. Charged current ν_μ interactions can be distinguished from other interaction types by their event topology: they contain a long muon track and a hadronic shower. The charge of final state leptons can also be deduced using the direction of curvature in the magnetic field, so ν_μ charged current interactions can be distinguished from $\overline{\nu}_\mu$ charged current interactions. MINOS has the tightest bounds on Δm^2_{32}, from energy-dependent ν_μ disappearance (assuming two flavour oscillations $\nu_\mu \rightarrow \nu_\tau$); the final results for ν_μ disappearance [40] are $\Delta m^2 = 2.39^{+0.09}_{-0.10} \times 10^3\,\text{eV}^2$ and $\sin^2 2\theta = 0.96^{+0.04}_{-0.04}$. Running in antineutrino mode the $\overline{\nu}_\mu$ disappearance parameters are compatible with those in neutrino mode [40]. The MINOS $\nu_\mu \rightarrow \nu_e$ results are discussed in Chapter 7 of this thesis.

The OPERA experiment is designed to look for ν_τ appearance in oscillations $\nu_\mu \rightarrow \nu_\tau$. A mostly ν_μ neutrino beam from CERN travels to Gran Sasso, where a segmented emulsion tracker looks for ν_τ charged current interactions; these are distinguished by their containing a track with a "kink" from a τ-decay. Currently OPERA have seen two ν_τ candidate events, against an expectation of 2.1 and non-oscillation background of 0.2 [36].

2.4.3 Non-zero θ_{13}

The appearance of ν_e in neutrino oscillations $\nu_\mu \rightarrow \nu_e$, at an atmospheric L/E, only occurs if the PMNS matrix parameter θ_{13} is non-zero (although there is a small appearance probability driven by θ_{12} that peaks at a much larger L/E *e.g.* KamLAND equivalent). Ignoring the small contributions from the term involving Δm^2_{21} and assuming that $\Delta m^2_{31} = \Delta m^2_{32}$ the probability for ν_e appearance in a ν_μ beam is:

$$P_{\nu_\mu \rightarrow \nu_e} = \sin^2\theta_{23} \sin^2 2\theta_{13} \sin^2 \frac{\Delta m^2_{32} L}{4E} \tag{2.33}$$

Two long baseline accelerator neutrino oscillation experiments, T2K and MINOS, published hints that θ_{13} may be non-zero, at $2.5\,\sigma$ [113] and 89% CL [129] respectively, in 2011. These results are discussed extensively, and combined, in Chapter 7 of this thesis. In 2012, T2K updated this result, excluding $\theta_{13} = 0$ at $3.2\,\sigma$ (99.92% CL), providing the first evidence of ν_e appearance in a ν_μ beam [43]. T2K found a best fit value of $\sin^2 2\theta_{13} = 0.104^{+0.060}_{-0.045}$. MINOS have also updated their result, ruling out $\theta_{13} = 0$ at 96% CL [40] ($1.8\,\sigma$).

Earlier in 2012, however, θ_{13} was discovered to be non-zero by an entirely different type of experiment. Daya Bay is an $\overline{\nu}_e$ disappearance experiment, which uses the $\overline{\nu}_e$ flux provided by six commercial nuclear reactors in China, and six identical liquid scintillator detectors (three near and three far) to measure $\overline{\nu}_e$ disappearance without dependence on reactor flux calculations. They excluded $\theta_{13} = 0$ at $5.2\,\sigma$ [41], discovering non-zero θ_{13}, and their most recent results [44] give best fit:

$$\sin^2 2\theta_{13} = 0.089 \pm 0.010(\text{stat}) \pm 0.005(\text{syst}) \tag{2.34}$$

Shortly after would follow confirmation from a very similar experiment in Sou-

th Korea, RENO, with $\theta_{13} = 0$ excluded at $4.9\,\sigma$ [42]. A one detector reactor disappearance experiment in France, Double Chooz, has also shown evidence that θ_{13} is non-zero at $3.1\,\sigma$ [45]. That θ_{13} is now known to be non-zero is of great importance, as it opens the possibility of $\mathcal{CP}$-violation in neutrino oscillations.

2.4.4 $\mathcal{CP}$-Violation

There are three discrete symmetries that are often considered in particle physics: charge conjugation, parity and time reversal. The charge conjugation operator ($\mathcal{C}$) has the effect of changing a particle into its antiparticle, the parity operator ($\mathcal{P}$) reflects the spatial co-ordinates: $(ct, \boldsymbol{x}) \rightarrow (ct, -\boldsymbol{x})$ and the time reversal operator ($\mathcal{T}$) reflects time: $(ct, \boldsymbol{x}) \rightarrow (-ct, \boldsymbol{x})$. The effect of the charge conjugation operator on neutrino oscillations $\nu_\mu \rightarrow \nu_e$ is:

$$\mathcal{C}\left(\nu_\mu \rightarrow \nu_e\right) = \overline{\nu}_\mu \rightarrow \overline{\nu}_e \tag{2.35}$$

Since neutrinos are left-handed, and the charge conjugation affects neither spin nor momentum, the resulting antineutrinos are also left-handed, so the parity operator is needed to give them the correct helicity:

$$\mathcal{CP}\left(\nu_\mu^{LH} \rightarrow \nu_e^{LH}\right) = \overline{\nu}_\mu^{RH} \rightarrow \overline{\nu}_e^{RH} \tag{2.36}$$

$\mathcal{CP}$-violation in neutrinos therefore occurs when the probability:

$$P\left(\nu_\mu \rightarrow \nu_e\right) \neq P\left(\overline{\nu}_\mu \rightarrow \overline{\nu}_e\right) \tag{2.37}$$

This may be possible for any distinct pair of neutrino flavours. For the survival probability of one neutrino species, however, the operation $\mathcal{CP}$ is equivalent to $\mathcal{CPT}$, and thus violating $\mathcal{CP}$ symmetry also violates the $\mathcal{CPT}$ conservation theorem [46]. The proof of this theorem requires that the laws of special relativity,

quantum mechanics and unitarity are not violated. Consequently, reactor $\overline{\nu}_e$ disappearance experiments are not sensitive to $\mathcal{CP}$-violation, assuming that the $\mathcal{CPT}$ conservation theorem holds.

The reason that $\mathcal{CP}$-violation is such an interesting area of neutrino physics is actually cosmological. The Universe that we observe today is predominantly made up of matter, but there is no particular reason to assume that this was always the case; in fact it is generally assumed that matter and antimatter were created in equal quantities during the Big Bang. In 1967, Sakharov proposed that a matter-antimatter asymmetry could develop from an initially symmetric Universe [47]. One of the conditions required for this to occur is $\mathcal{CP}$-violation. The other conditions are that there be at least one process which violates the conservation of baryon number, that there be $\mathcal{C}$-violation and that the baryon-number violating processes occur out of thermal equilibrium.

2.5 Sterile Neutrinos

Neutrino oscillations are now a well established phenomenon, and have been observed to occur driven by two distinct values of Δm^2 in solar and atmospheric neutrino oscillation experiments. However, even before the definitive discovery of neutrino oscillations by SNO [18], hints were starting to appear that neutrinos might also be oscillating due to a third distinct Δm^2, requiring a fourth neutrino mass eigenstate. Due to the unitarity of the PMNS matrix, this would also require a fourth neutrino flavour eigenstate, which is ruled out by the Z^0 width results from LEP [9], unless the new neutrino is either heavy or sterile. The apparent new Δm^2 [49], along with the absolute mass scale of the active neutrinos [62, 63], means that the new neutrino would be light enough for the Z^0 to decay to pairs of them, requiring the new neutrino flavour eigenstate to be "sterile" (sterile here is defined as not coupling to the Z^0). The hints

for oscillations due to sterile neutrinos come from many different types of experiments: accelerator neutrino experiments ($\overline{\nu}_\mu \rightarrow \overline{\nu}_e$ and $\nu_\mu \rightarrow \nu_e$), reactor antineutrino experiments ($\overline{\nu}_e \rightarrow \overline{\nu}_e$) and gallium experiments ($\nu_e \rightarrow \nu_e$). These hints are summarised in the following sections.

2.5.1 The LSND Anomaly

The Liquid Scintillator Neutrino Detector (LSND) Experiment [48], at Los Alamos, saw an excess of $\overline{\nu}_e$ events in a partly $\overline{\nu}_\mu$ beam [49]. The LSND neutrino beam contained $\overline{\nu}_\mu$, and was created using pion and muon decay at rest (DAR). The neutrino beam was created by colliding protons onto a water target to create mostly π^+, which predominantly came to rest within the water target decaying:

$$\pi^+ \rightarrow \mu^+ + \nu_\mu \tag{2.38}$$

The muons then decayed:

$$\mu^+ \rightarrow e^+ + \nu_e + \overline{\nu}_\mu \tag{2.39}$$

The maximum energy of the $\overline{\nu}_\mu$ was 52.8 MeV, so a ν_μ beam was also considered by only looking at those events with energies greater than 60 MeV; this is called decay in flight (DIF). Hardly any $\overline{\nu}_e$ were produced by the decays of negative pions, since these were mostly absorbed in the target before they had the chance to decay.

The detector was located at 30 m from the neutrino production target and detected $\overline{\nu}_e$ via the inverse β-decay process:

$$\overline{\nu}_e + p \rightarrow e^+ + n \tag{2.40}$$

The neutron was then captured on a proton (in the mineral oil, CH_2) and a 2.2 MeV photon was released, resulting in a delayed co-incidence which identified the $\overline{\nu}_e$. ν_e interactions would not fake this signal as no neutron is emitted, and the beam was mostly too low in energy for muons to be created, so ν_μ and $\overline{\nu}_\mu$ charged current interactions were rare.

For the DAR $\overline{\nu}_\mu$ beam, an excess of $\overline{\nu}_e$ was observed in the region 20 to 60 MeV. The total excess was $87.9 \pm 22.4 \pm 6.0$ $\overline{\nu}_e$ candidate events [49]. The significance of this excess is $3.8\,\sigma$ [53]. From the DIF ν_μ beam no significant excess was seen, $8.1 \pm 12.2 \pm 1.7$ ν_e candidates were observed [50].

The Karlsruhe-Rutherford Medium Energy Neutrino (KARMEN) Experiment [51] ran from 1990-2001, at the Rutherford-Appleton Laboratory, with a similar neutrino beam, similar detector, and a slightly shorter baseline (17.6 m) than LSND. KARMEN did not observe any significant excess of $\overline{\nu}_e$ events, 15 events were observed against an expectation of 15.8 ± 0.5. Since LSND and KARMEN are at different baselines, there exist oscillation parameters that satisfy both experimental results [52], as can be seen in Figure 2.6.

MiniBooNE was designed to test the results of the LSND experiment; it has roughly the same L/E as LSND, but different peak neutrino energy and baseline [53]. Like LSND, MiniBooNE has a mineral oil (CH_2) liquid scintillator detector, but the neutrino beam is made by colliding protons onto a beryllium target and then focussing the positive (negative) daughter particles (mostly pions) and allowing them to decay in flight to create an muon-(anti)neutrino beam with mean energy 600 MeV. Charged-current quasi-elastic (CCQE) neutrino events can be seen from the Čerenkov and scintillation light produced by the final state charged lepton, and ν_μ can be distinguished from ν_e by the shape of the Čerenkov rings. No charge separation is possible however, so ν_e cannot be distinguished from $\overline{\nu}_e$ interactions; it is also not possible to distinguish between photons and electrons with the MiniBooNE detector.

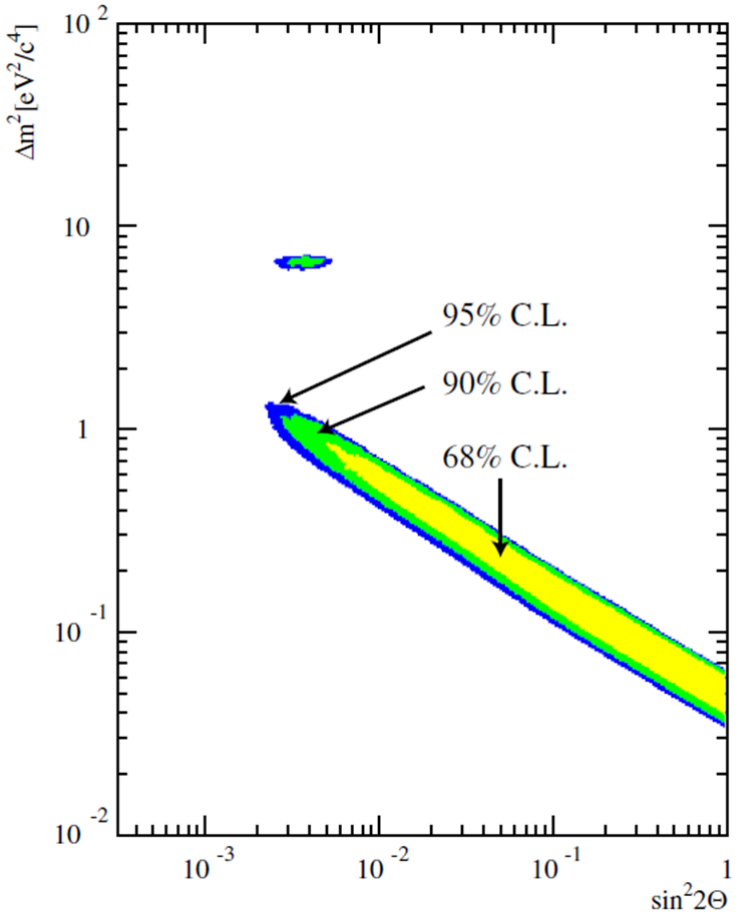


Figure 2.6: The combined allowed oscillation parameters, assuming one additional sterile neutrino, of the LSND and KARMEN experiments. Plot from [52]

MiniBooNE has run in both ν_μ and $\overline{\nu}_\mu$ beam configurations to search for both $\nu_\mu \to \nu_e$ and $\overline{\nu}_\mu \to \overline{\nu}_e$. In both searches, excesses of ν_e-like events are seen in the low energy region of the search region [54], as can be seen in Figure 2.7. For the neutrino mode, the significance of the excess is $3.0\,\sigma$ and for antineutrino mode it is $2.5\,\sigma$; the significance of the total event excess is $3.8\,\sigma$.

2.5.2 The Reactor Antineutrino Anomaly

Another hint that neutrinos may be oscillating over a short baseline (< 100 m) comes from the deficits of $\overline{\nu}_e$ observed by many different antineutrino detectors

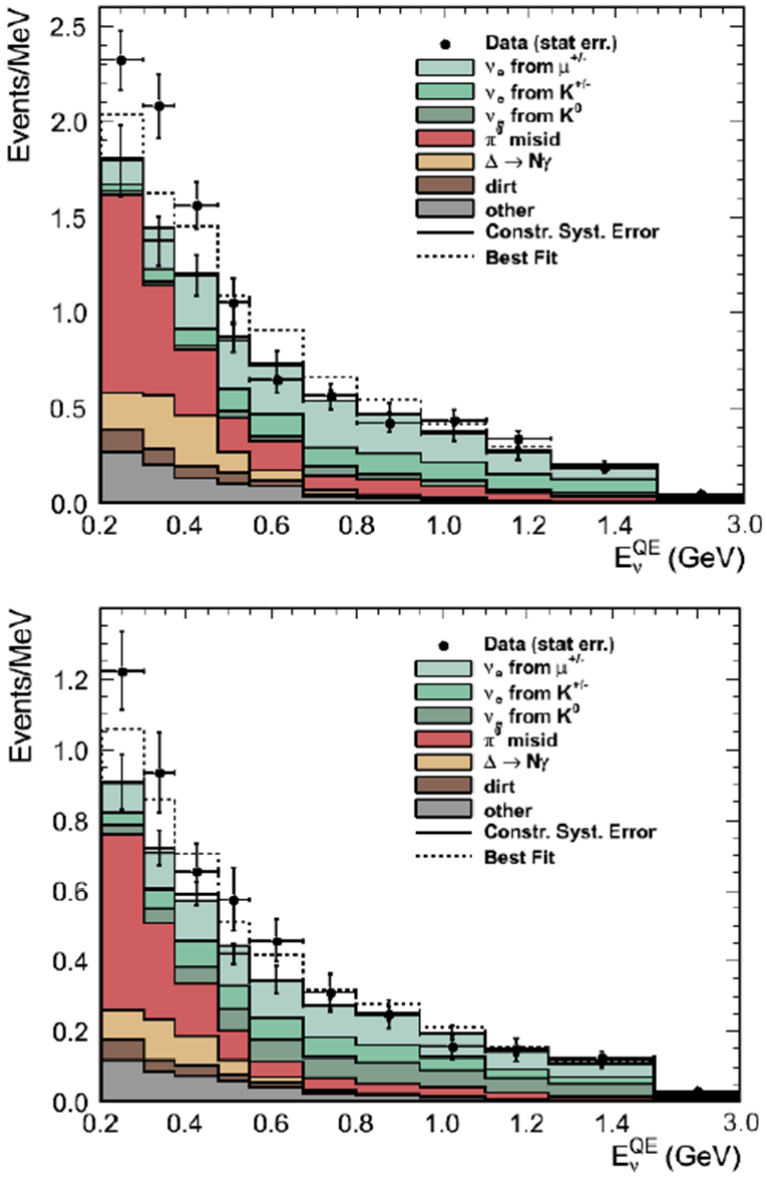


Figure 2.7: The low energy electron-neutrino-like event excesses seen in MiniBooNE neutrino (above) and antineutrino (below) runs. The best fit lines shown assume short baseline oscillations $\nu_\mu \rightarrow \nu_e$ and $\overline{\nu}_\mu \rightarrow \overline{\nu}_e$ respectively. Plots from [54]

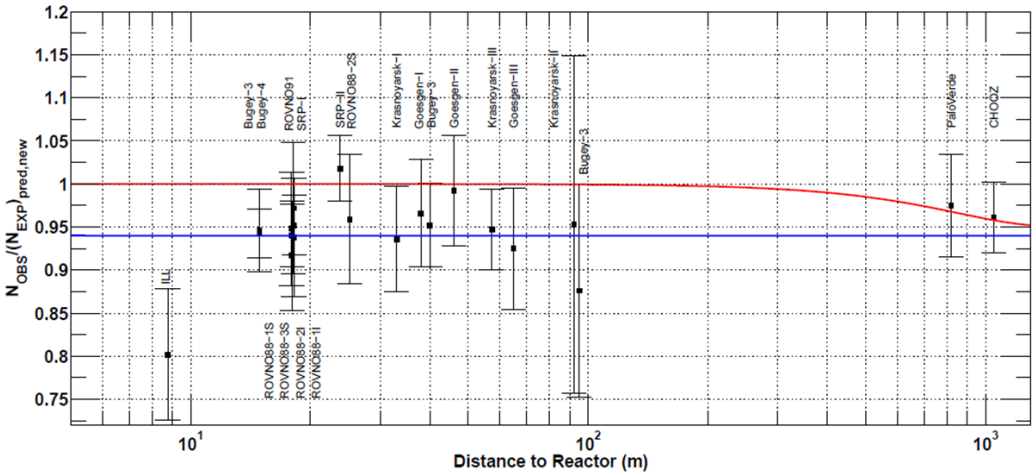


Figure 2.8: The ratios of observed to predicted electron antineutrino events seen by various different reactor neutrino experiments as a function of their baseline. An attempt to fit the data with a three active flavour solution ($\sin^2 2\theta_{13} = 0.06$) can be seen in the red line, whereas an example of a fit using an additional sterile neutrino ($\sin^2 2\theta_s = 0.12$, $|\Delta m_s^2| \gg 1\,\mathrm{eV}^2$) can be seen in the blue line. Plot from [55]

placed close to nuclear fission reactors. These deficits can be seen in Figure 2.8. The flux of antineutrinos from a nuclear reactor must be calculated from models of the fission of uranium and plutonium. These flux calculations have recently been revised upwards, leading to an average ratio of observed to predicted reactor antineutrinos of 0.943 ± 0.023 [55]. This means that either there are further problems with the calculation of the antineutrino flux from reactors, or that some of the neutrinos are not interacting in the detectors as electron antineutrinos.

2.5.3 The Gallium Anomoly

Two solar neutrino experiments, GALLEX [56] and SAGE [57, 58], both use gallium to detect neutrinos via the process:

$$\nu_e + {}^{71}\mathrm{Ga} \rightarrow {}^{71}\mathrm{Ge} + e^- \tag{2.41}$$

These experiments have seen deficits of ν_e from their calibration sources. GALLEX used a chromium source that decays through electron capture:

$$e^- + {}^{51}\mathrm{Cr} \rightarrow {}^{51}\mathrm{V} + \nu_e \tag{2.42}$$

The ratio of the number of observed ν_e to that predicted was found to be 0.882 ± 0.078. SAGE also used a chromium source, and found this ratio to be $0.95 \pm 0.12(\mathrm{expt})^{+0.035}_{-0.027}(\mathrm{theor})$. In addition, SAGE used an argon source which decays as:

$$e^- + {}^{37}\mathrm{Ar} \rightarrow {}^{37}\mathrm{Cl} + \nu_e \tag{2.43}$$

With this source the ratio of observed to predicted ν_e events was found to be $0.79^{+0.09}_{-0.10}$. The combined significance of the ν_e deficits of both experiments is $2.7\,\sigma$ [59], with one possible interpretation being short-baseline ν_e disappearance via oscillations.

2.6 Non-Oscillation Neutrino Physics

Following the discovery that neutrinos oscillate and are therefore massive, it is natural to wonder what the masses of the neutrinos actually are. Since neutrino oscillation experiments can only tell us about the mass squared splittings of the neutrino mass eigenstates, other types of experiments are needed. There are three main lines of attack: distortion of the electron energy end-point of tritium decays, described in Section 2.6.1, neutrino-less double beta decay, which is also concerned with the question of whether or not the neutrino is its own antiparticle, described in Section 2.6.2, and neutrino velocity measurements, described in Section 2.6.3.

2.6.1 Neutrino Mass Measurements from Decays

Neutrino mass can be measured using pion [60] and tau decays [61], by measuring the momentum of the non-neutrino final state particles and using conservation of four-momentum, but the best limits on the neutrino mass come from the β-decay of tritium:

$$^3\mathrm{H} \rightarrow {}^3\mathrm{He}^+ + e^- + \overline{\nu}_e \tag{2.44}$$

If neutrinos are massive, there is a modification in the energy spectrum of the electron from the β-decay, which is particularly significant around the end-point energy (the maximum possible energy of the electron), since less energy is available for the electron's momentum if the neutrino is massive. A plot of what this modification would look like for a 1 eV neutrino (where we here make the assumption that a neutrino mass eigenstate is produced in the β-decay; in reality we know it is a superposition of the three neutrino mass eigenstates) can be seen in Figure 2.9. This distortion occurs regardless of whether the neutrino is a Majorana or Dirac particle.

The current best limits on the mass of the neutrino using tritium β-decay come from the Mainz [62] and Troitzk [63] experiments:

$$m_{\nu_e} < 2.3\,\mathrm{eV}\ (95\%\ \mathrm{CL})\ [62] \tag{2.45}$$

$$m_{\nu_e} < 2.2\,\mathrm{eV}\ (95\%\ \mathrm{CL})\ [63] \tag{2.46}$$

Another tritium β-decay experiment, the KArlsruhe TRItium Neutrino Experiment (KATRIN) [64], is currently under construction and is expected to start taking physics data in 2015 [65]. KATRIN aims to reach a sensitivity to the effective neutrino mass in tritium β-decay of 200 meV, *i.e.* an order of magnitude

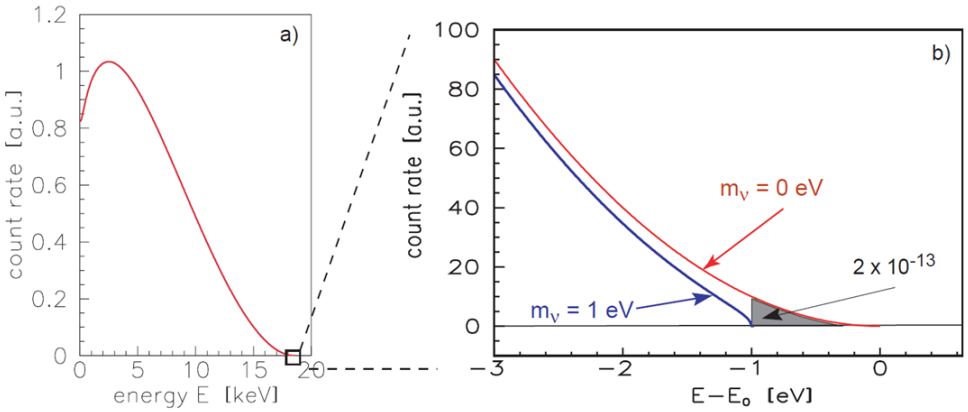


Figure 2.9: The electron energy spectrum from tritium β-decay. Plot (a) shows the total spectrum, and plot (b) shows a small region around the end-point energy, E_0. A massive neutrino will cause a distortion (blue line) in the energy spectrum, which is particularly significant close to the end-point energy. In this case the distortion for a 1 eV neutrino is shown: only 2×10^{-13} of the β-decays would be expected to be above this modified end-point energy if neutrinos were mass-less. Figure from [64]

better than the current measurements.

2.6.2 Neutrinoless $\beta\beta$-Decay

One of the fundamental questions remaining in neutrino physics is whether or not the neutrino is its own antiparticle. In the Standard Model of particle physics, all fermions are Dirac particles, that is, they have a distinct antiparticle. However, it has been suggested that neutral fermions could be their own antiparticle, in which case they would be Majorana particles rather than Dirac particles. If neutrinos are their own antiparticle then they can undergo neutrinoless double β-decay: an interaction that requires a neutrino (in the Dirac picture) to be emitted, and then requires the same particle to be absorbed as an antineutrino (in the Dirac picture).

So far, only one subset of the members of one neutrinoless double beta decay experiment, the Heidelberg-Moscow Experiment, have claimed to see a

signal [67, 68, 69]. The Heidelberg-Moscow experiment looked for the double and neutrinoless double beta decay of ^{76}Ge. The no neutrino decays $^{76}\text{Ge} \rightarrow ^{76}\text{Se} + 2e^-$ can be separated from the standard double beta decays $^{76}\text{Ge} \rightarrow ^{76}\text{Se} + 2e^- + 2\overline{\nu}_e$ from the energy of the final state electrons. The latest claim is a discovery at $> 6\sigma$ of the neutrinoless double beta decay of ^{76}Ge with half-life:

$$T_{1/2}(0\nu) = 2.23^{+0.44}_{-0.31} \times 10^{25}\,\text{yr} \tag{2.47}$$

However, these results have been questioned [70, 71] and another group from the same experiment have instead set a lower bound on the half-life of neutrinoless double beta decay [72]:

$$T_{1/2}(0\nu) \geq 1.55 \times 10^{25}\,\text{yr} \;\; (90\%\;\text{CL}) \tag{2.48}$$

The IGEX experiment [73] has also set a lower bound on the half-life of ^{76}Ge neutrinoless double beta decay of:

$$T_{1/2}(0\nu) \geq 1.57 \times 10^{25}\,\text{yr} \;\; (90\%\;\text{CL}) \tag{2.49}$$

Currently there are many neutrinoless double beta decay experiments running and planned with different elements and different detector technologies [74, 75, 76, 77], however none has yet to claim a signal. The only currently running experiment using ^{76}Ge is GERDA [77], which should eventually be able to reach a sensitivity of:

$$T_{1/2}(0\nu) \geq 2 \times 10^{26}\,\text{yr} \;\; (90\%\;\text{CL}) \tag{2.50}$$

The half life of neutrinoless $\beta\beta$-decay for a nucleus, $\mathcal{N}$, is related to the effective mass of the electron neutrino, $m_{\beta\beta}$ since the electron neutrino flavour

eigenstates is a superposition of the different neutrino mass eigenstates, by the relationship [66]:

$$\left[T_{1/2}(0\nu,\mathcal{N})\right]^{-1} = f\left(\mathcal{N}\right)\frac{|m_{\beta\beta}|^2}{m_e^2} \tag{2.51}$$

Where $f\left(\mathcal{N}\right)$ must be calculated and its error is dominated by the uncertainty on the nuclear matrix element. For the Germanium experiments, the best limit on the effective mass of the electron neutrino in neutrinoless $\beta\beta$-decay comes from IGEX [73]:

$$m_{\beta\beta} < 0.33 - 1.35 \text{ eV } (90\% \text{ CL}) \tag{2.52}$$

Depending on theoretical assumptions during the calculation of $f\left(\mathcal{N}\right)$.

2.6.3 Neutrino Velocity Measurements

Neutrino velocity measurements have recently been one of the more controversial aspects of neutrino research. There are two main ways to measure neutrino velocities: accelerator neutrino experiments and observations of neutrinos and photons from supernova SN1987A.

Supernova 1987A

When a star goes supernova, an intense burst of neutrinos with average energy $\mathcal{O}$(10 MeV), is emitted [78]. In 1987, three different neutrino detectors observed neutrinos from the supernova SN1987A in the Large Magnetic Cloud: Kamiokande-II saw 12 events in a 13 s window, with an average energy of 15 MeV [79], the IMB detector saw 8 events in a 6 s window with energies of 20-40 MeV [80] and the Baksan detector saw 5 events in a 10 s window, with energies of 10-25 MeV [81], the timing of which was compatible with the other two

observations.

By comparing the relative arrival times of the neutrinos and the photons, which were first detected a few hours later, an upper bound has been set on the difference between the velocity of the electron anti-neutrino and the speed of light [83],

$$|(v_\nu - c)/c| \leq 2 \times 10^{-9}$$

Since neutrinos from supernovae are emitted with a range of different energies, if they are massive their arrival times will be slightly different, and thus the neutrino burst will broaden in time. A combined analysis of the durations of the three observations [82] has found an upper bound on the electron neutrino mass of:

$$m_{\nu_e} < 5.7 \text{ eV } (95\% \text{ CL})$$

Accelerator Neutrino Experiments

Neutrino velocity was first measured using a neutrino beam at Fermilab in 1979 [88]. More recently, two long baseline neutrino oscillation experiments, MINOS [85, 86] and OPERA [84, 87] have also tried to measure neutrino velocity. Both experiments now find the neutrino velocity to be consistent with the speed of light (OPERA initially released results suggesting neutrinos were travelling faster than the speed of light [84], but have since traced this result back to problems with the timing [87]). The latest measurement from MINOS [86] is:

$$(v_\nu - c)/c = (0.7 \pm 1.3) \times 10^{-5} \ (68\% \text{ CL})$$

The updated measurement of OPERA is:

$$(v_\nu - c)/c = (2.7 \pm 3.1(\text{stat.}) \, ^{+0.38}_{-0.28}(\text{sys.})) \times 10^{-6} \ (68\% \text{ CL})$$

Both measurements use a ν_μ beam, a timing system close to the neutrino production point and another hundreds of kilometers away. These two timing systems are aligned with each other using sophisticated GPS techniques. In addition, the baseline is measured to very high precision by professional metrologists.

Current and future long baseline neutrino oscillation experiments *e.g.* T2K, MINOS+ and NOνA [138], will try to improve the precision of these measurements.

Chapter 3

The T2K Experiment

This chapter gives a description of the T2K experiment. An overview of the experimental setup is given in Section 3.1, with detailed descriptions of different parts of the experiment then following in Sections 3.2 through 3.5. The main physics goals of the T2K experiment, the search for electron neutrino appearance in atmospheric neutrino oscillations and the precision measurement of the atmospheric neutrino oscillation parameters θ_{23} and Δm^2_{32} from muon neutrino disappearance, are discussed in Section 3.6.

3.1 Overview of Experimental Setup

T2K is a long-baseline (equivalent to atmospheric L/E) neutrino oscillation experiment. A schematic of the T2K experiment can be seen in Figure 3.1. A mostly ν_μ beam is produced at the Japan Proton Accelerator Research Complex (J-PARC) in Tokai by colliding 30 GeV protons onto a graphite target, creating hadrons, mostly pions and kaons. The positively charged particles are then focused with a series of three magnetic horns, and allowed to decay in a 110 m long helium-filled decay pipe. Due to the fact that the charged lepton anti-particle in the π^+-decay must be left-handed, the neutrino beam is predomi-

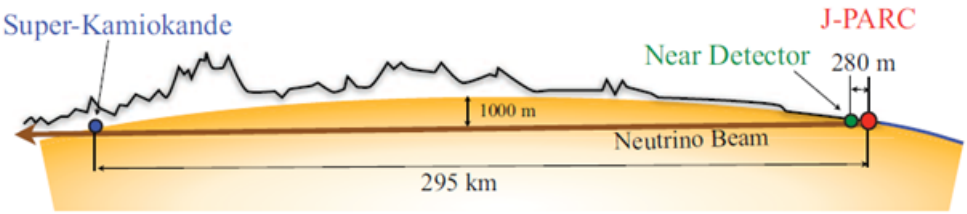


Figure 3.1: Schematic of the T2K Experiment [91]. A ν_μ beam is produced at J-PARC, a near detector complex, the ND280, monitors the neutrino interactions after 280 m, and Super-Kamiokande, 295 km away, looks for evidence of neutrino oscillations via ν_μ disappearance and ν_e appearance.

nantly made up of muon neutrinos. Details of the neutrino beam production and monitoring can be found in Section 3.2.

The neutrinos are then measured 280 m from the production target by a complex of near detectors called the ND280. The neutrino interaction rates can then be checked against simulations of the beam, and used to extrapolate the event rates expected at the far detector, in the absence of oscillations. The ND280 will also be used to perform cross section measurements of many different types of neutrino interaction. A detailed description of the Near Detectors is given in Section 3.3.

The neutrinos then travel 295 km across Japan to the far detector: Super-Kamiokande (SK), a massive water Čerenkov detector, which is described in Section 3.4. When the neutrinos undergo charged current interactions in the water, the final state charged lepton travels faster than the speed of light in water, emitting a cone of Čerenkov radiation which can be detected by the surrounding photo-multiplier tubes (PMTs).

By comparing the number and flavours of the neutrinos that interact in SK to those predicted by the simulations and near detectors, it is possible to extract information on the parameters of the PMNS matrix which govern neutrino oscillations at atmospheric L/E: θ_{23}, θ_{13} and Δm^2_{32}.

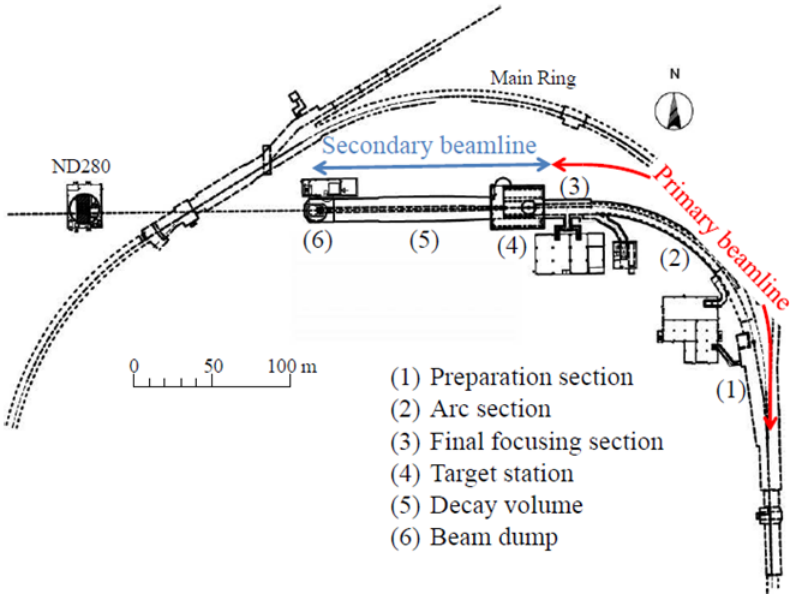


Figure 3.2: A schematic of the T2K neutrino beamline, target station and decay tunnel. 30 GeV protons are collided with a graphite target (4), producing hadrons that are focused and then decay to create a mostly ν_μ beam. Image from [91].

3.2 Neutrino Beam

The Main Ring (MR) accelerator at J-PARC accelerates protons up to 30 GeV. The protons are held in 8 bunches (6 before Summer 2010), each pair separated by 580 ns, all of which can be extracted in a single turn to feed the T2K neutrino beamline. The MR provides protons to both the hadron and neutrino beamlines.

The T2K neutrino beamline is shown in Figure 3.2. The protons are turned to point at Kamioka (actually 2.5° off, see Section 3.2.1) and focused before colliding with the target. The target is a 91.4 cm graphite rod, which is placed inside the first magnetic horn so that the charged mesons produced can be collected. Then the positively charged mesons (mostly pions) are focused into a narrow beam with the second and third horns, which have been optimised to maximise the neutrino flux.

The secondary particles then travel down a 109 m long helium filled decay tunnel, where they decay predominantly $\pi^+ \rightarrow \mu^+\nu_\mu$. Remaining hadrons and muons are stopped at the end of the decay tunnel by the beam stop: 75 tons of graphite and 15 iron plates (totaling 2.4 m) stop all the muons with energies $<$ 5 GeV.

After the beam stop, the surviving muon flux is monitored with a series of muon monitor detectors, consisting of ionisation chambers, silicon photodiodes and an emulsion tracker. The muon monitor measures the direction of the neutrino beam, with a precision better than 0.25 mrad, and the stability of the beam intensity to a precision of 3%, on a bunch by bunch basis.

3.2.1 The Off-Axis Technique

The T2K neutrino beam is not directed straight at Super-Kamiokande. Instead, it is directed 2.5° off-axis. This technique creates a neutrino beam that is much narrower in energy than a conventional neutrino beam, removing the majority of the high energy tail, and with peak neutrino energy lower than the on-axis peak. The off-axis technique was first suggested by Beavis *et al.* in [95]. To see why this is, we must consider the two-body decay of the pion $\pi^+ \rightarrow \nu_\mu\,\mu^+$. By conservation of four-momentum: $p_\pi = p_\mu + p_\nu$, re-arranging and squaring we get: $m_\mu^2 = m_\pi^2 - 2p_\pi p_\nu$, ignoring the mass of the neutrino. Now, labelling the opening angle of the neutrino from the pion's direction of travel θ we get:

$$E_\nu = \frac{m_\pi^2 - m_\mu^2}{2\left(E_\pi - |\mathbf{p}_\pi|\cos\theta\right)} \tag{3.1}$$

In the case $\theta = 0$ the neutrino energy increases monotonically with the pion energy. However, if $\theta \neq 0$, we can find a maximum neutrino energy as a function of pion energy. A plot of this behaviour can be seen in Figure 3.3.

The effect of changing the off-axis angle for the T2K neutrino beam can be

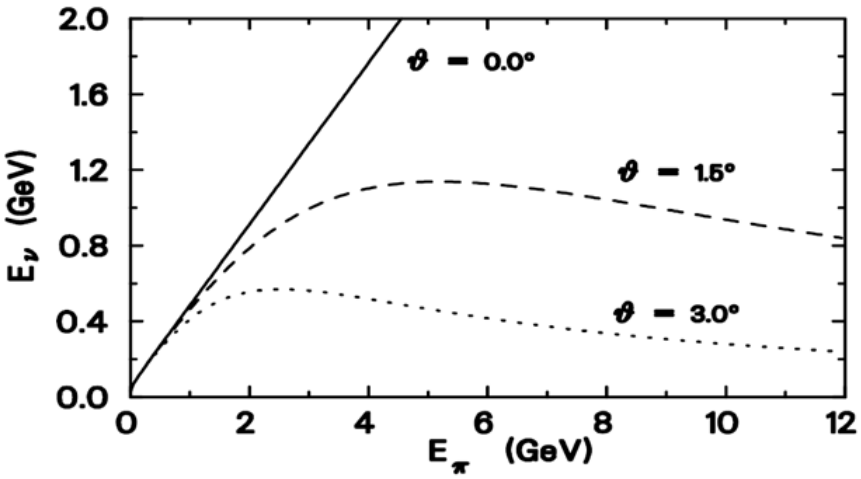


Figure 3.3: Neutrino energy against parent pion energy at different off-axis angles. On-axis, the neutrino energy increases monotonically with the parent pion energy. Off-axis, a maximum neutrino energy can be seen. This plot is taken from [95].

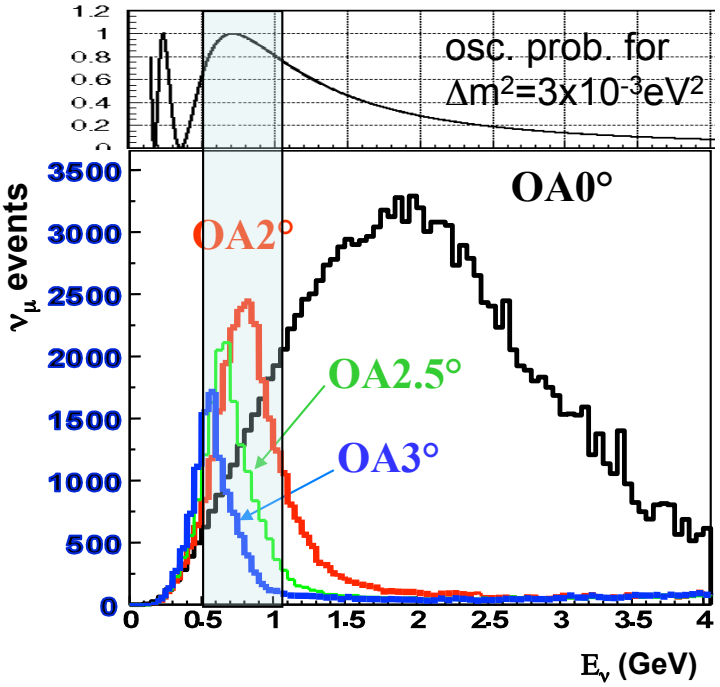


Figure 3.4: The effect of changing the off-axis angle of the T2K beam. The red, green and blue lines show the predicted ν_μ interaction rates at 2°, 2.5° and 3° off-axis respectively. The on-axis prediction is shown by the black line. Plot from [96].

seen in Figure 3.4. The off-axis angle is tuned to produce a neutrino beam with a narrow energy range around the atmospheric oscillation maximum energy, following the disappearance measurement of MINOS [97]. One of the main advantages of having an off-axis beam for a ν_e appearance measurement is the reduction of the high energy tail of neutrinos, and consequently the backgrounds from neutral current (NC) events. NC events present only a fraction of the neutrino energy in the visible final state, often producing π^0 which decays $\pi^0 \rightarrow \gamma\gamma$. If one of these photons is subsequently lost by the reconstruction, a single photon, which is indistinguishable from an electron in Super-Kamiokande, can be produced close to the oscillation maximum. Another advantage is the reduction in the high energy ν_μ, which could migrate into the oscillation region if their energy is mis-reconstructed.

3.3 The Near Detectors: ND280 and INGRID

The T2K Near Detector Complex (ND280) is located 280 m from the hadron production target and consists of two sections, an on-axis beam monitor, the Interactive Neutrino GRID (INGRID), and an off-axis composite detector, also called the ND280. For clarity, future uses of ND280 in this thesis will refer only to the off-axis part of the T2K near detector.

3.3.1 INGRID

INGRID is an array of seven horizontal and seven vertical iron/scintillator neutrino detector modules, centered on the beam axis. Its role is to monitor the neutrino beam direction, and the beam intensity. In addition to the fourteen modules that make up the cross, two more identical modules are placed off-axis, in order to monitor the axial symmetry of the neutrino beam. The layout of the INGRID detector can be seen in Figure 3.5. INGRID uses the number of

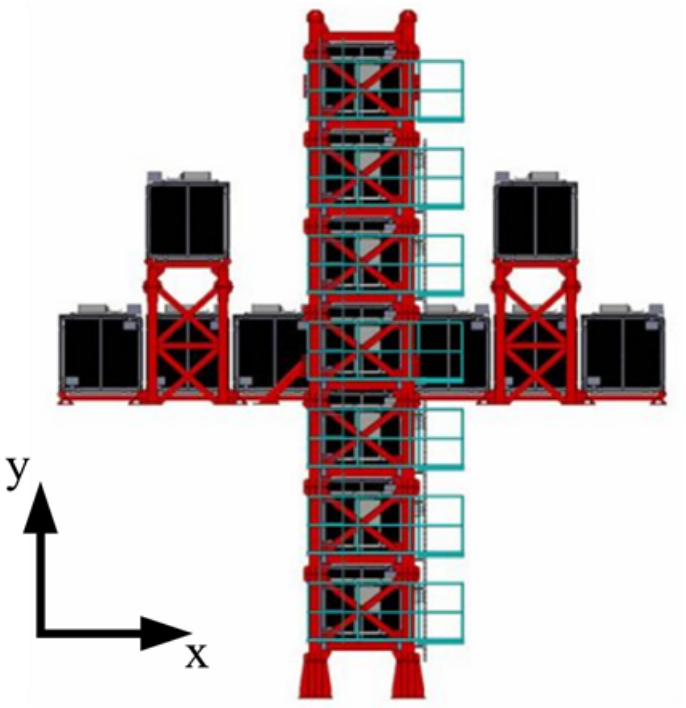


Figure 3.5: A schematic of the INGRID module layout. Fourteen modules form a cross in the horizontal and vertical directions, to monitor the beam position. In addition, two modules monitor the axial symmetry of the beam, and a proton module aligned with the beam center studies charged current quasi-elastic (CCQE) interactions of the beam ν_μ. Image from [91]

neutrino interactions per day in each detector module to monitor the position of the beam center, and can achieve an accuracy of 10 cm.

Each of the INGRID detector modules is made up of nine iron planes (totaling 7.1 tons) and eleven scintillator planes. Each module is also surrounded by scintillator veto planes to reject any events that come into the detector from the outside. Each of the scintillator planes is made up of two layers of scintillator bars, 24 in the horizontal direction and 24 in the vertical direction, each of which transports scintillation light out with a wavelength shifting (WLS) fibre in an extruded hole at its center. The light from these WLS fibres is then read out using MPPCs and TRIP-t electronics, as described in Section 3.3.3. An event display of a typical charged current neutrino interaction in one of these modules can be seen in Figure 3.6.

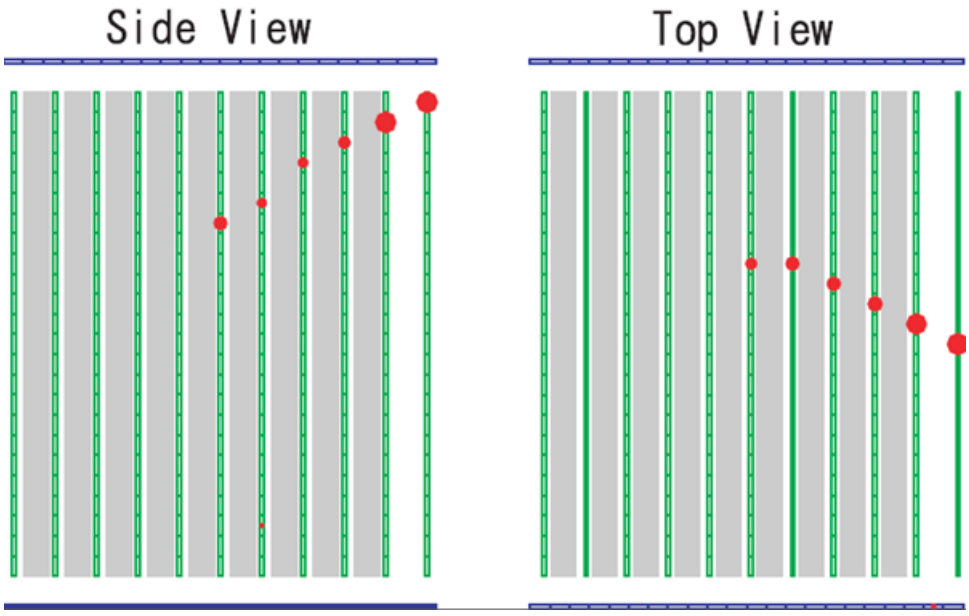


Figure 3.6: An event display of a typical charged current neutrino interaction from the T2K beam in INGRID. Image from [91]

INGRID also has a module that is capable of reconstructing proton tracks (Proton Module) which is made up entirely of scintillator planes rather than also containing iron planes. It is located at the center of the INGRID cross, between the central horizontal and vertical modules. The Proton Module can distinguish between quasi-elastic (CCQE) and deep inelastic charged-current ν_μ interactions, which means a separate energy spectrum measurement of the CCQE neutrino interactions can be made.

3.3.2 ND280

The T2K ND280 off-axis detector (ND280), a diagram of which can be seen in Figure 3.7, is made up of five different sub-detector systems, all enclosed inside the 0.2 T UA1 magnet donated by CERN. The Side Muon Range Detector (SMRD) consists of plastic scintillator layers sandwiched between the steel plates that make up the magnet's return yoke.

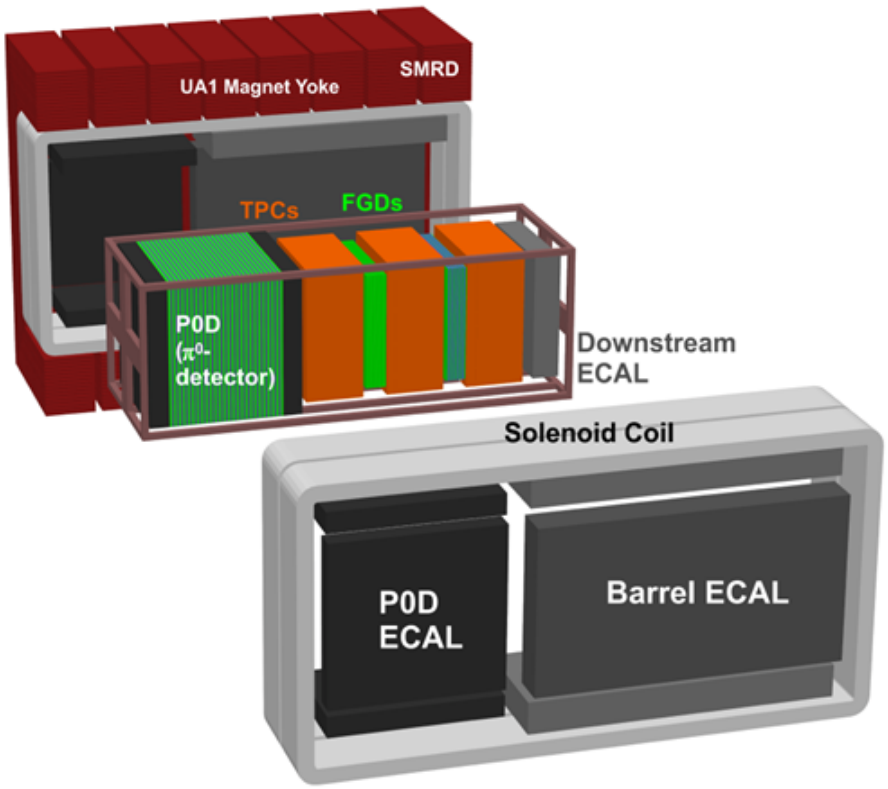


Figure 3.7: A schematic of the T2K ND280. The UA1 magnet (containing the SMRD) surrounds the inner sub-detectors. The central basket region consists of the PØD, three TPCs, two FGDs and a downstream ECal. Surrounding the basket region are 12 ECals. Figure from [91]

Enclosed within the magnet return yoke are the inner sub-detectors. A steel supporting basket contains, from upstream to downstream: a π^0 detector (PØD), two Fine Grained Detectors (FGDs) sandwiched between three Time Projection Chambers (TPCs), and finally a Downstream Electro-magnetic Calorimeter (DsECal). Surrounding the sub-detectors in the basket are 12 more ECal modules: 6 surrounding the PØD (PØD ECal) and 6 surrounding the tracker (TPC/FGD) region (Barrel ECal).

ECals

The ECals are made up of alternating lead layers and plastic scintillator layers. The scintillator layers are made up of plastic bars, each of which has a Wavelength Shifting (WLS) fibre in a hole burrowed along the centre. At each end of the bars (in fact some are only single ended, including all the bars in the PØD ECal) is a Multi-Pixel Photon Counter (MPPC). These photo-sensors and the read-out electronics are the same for the SMRD, PØD, ECal and INGRID and are described in Section 3.3.3.

The ECal has two main roles within the ND280: total energy measurement and particle identification (PID). Electrons and photons entering the ECal shower, depositing all (unless the shower is not fully contained) of their energy in the ECal.

PØD

The π^0 Detector (PØD) is designed specifically to look for π^0 from neutrino interactions. The π^0 themselves are not seen, rather their decays via their dominant mode, $\pi^0 \rightarrow \gamma\gamma$, are searched for by looking for two electro-magnetic (EM) showers consistent with a decay from a parent around the π^0 invariant mass.

The PØD is made up of four sections, called super-PØDules, two of which (upstream and downstream most parts) are calorimeters, and two of which are targets. A schematic of the PØD can be seen in Figure 3.8. The target super-PØDules consist of alternating target (lead and brass layers) and scintillator layers. The scintillator layers in the PØD are distinct from those in the ECals in that they have a triangular rather than rectangular profile, allowing for better spatial resolution. The target layers in the PØD consist of bags that can either be filled with water or left empty to use air. By comparing the rate of neutrino interactions with water in and water out, the interaction rate on water can be

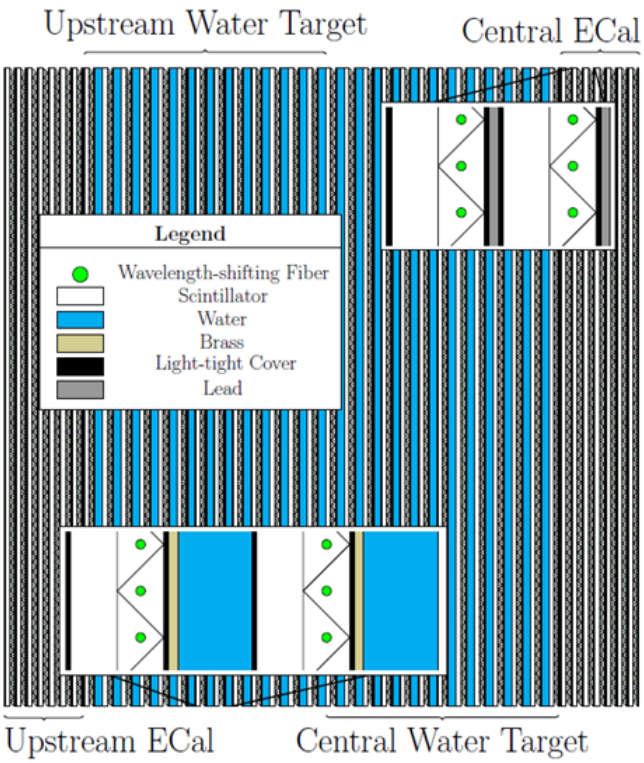


Figure 3.8: A schematic of the ND280 π^0-detector (PØD). The PØD contains both calorimeter and water target sections. A unique feature of the PØD, amoung the ND280 sub-detectors, is the triangular scintillator bar profile. Picture taken from [91]

deduced, which is very important since the far detector interactions occur on water.

ND280 Tracker: FGDs and TPCs

The ND280 tracker region is made up of three Time Projection Chambers[98] (TPCs) and two Fine Grained Detectors (FGDs) [99]. The FGDs are so named because they have a very small profile to their scintillator bars, giving very high resolution around any neutrino interaction vertices that occur within them. The FGDs use plastic as both their target and scintillator material, being entirely composed of 9.61 mm $\times$ 9.61 mm $\times$ 1864.3 mm bars of polystyrene scintillator with a wavelength shifting fibre running through the centre, as with the other

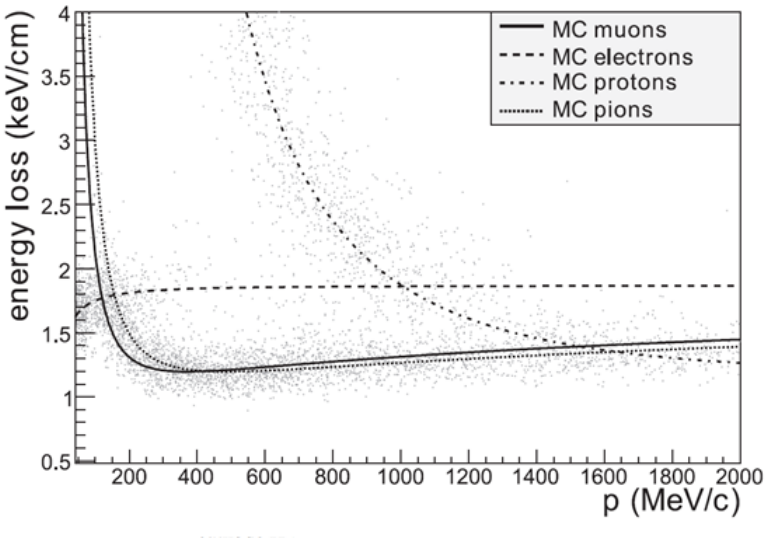


Figure 3.9: The energy loss per unit distance as a function of momentum of different particle types in the TPC. Data in this plot were recorded during the first T2K physics run. Figure taken from [91]

scintillator detectors. Each bar is read out by a single MPPC.

FGD1 has 30 layers of 192 scintillator bars, which are arranged in alternating horizontal (x) and vertical (y) layers. FGD2 also contains water targets, seven pairs of layers (one x and one y) alternate with six 2.5 cm thick water targets.

The Time Projection Chambers (TPCs) are very important for measuring particle momentum (by measuring the track curvature in the magnetic field) and performing particle identification (PID). This is done using a combination of the particle momentum and ionisation, the different energy loss of different particles can be used to identify them, as can be seen in Figure 3.9.

Each of the three TPCs consists of an inner box containing an argon-based gas, surrounded by a carbon-dioxide filled outer box. The inner box itself acts as a cathode (the sides in the yz-plane), which, in conjunction with the central anode, causes a uniform electric field across the detector in the x-direction. This electric field causes the electrons released during ionisation by an incident particle to drift to the edges of the detector where they are then read out by the TPC

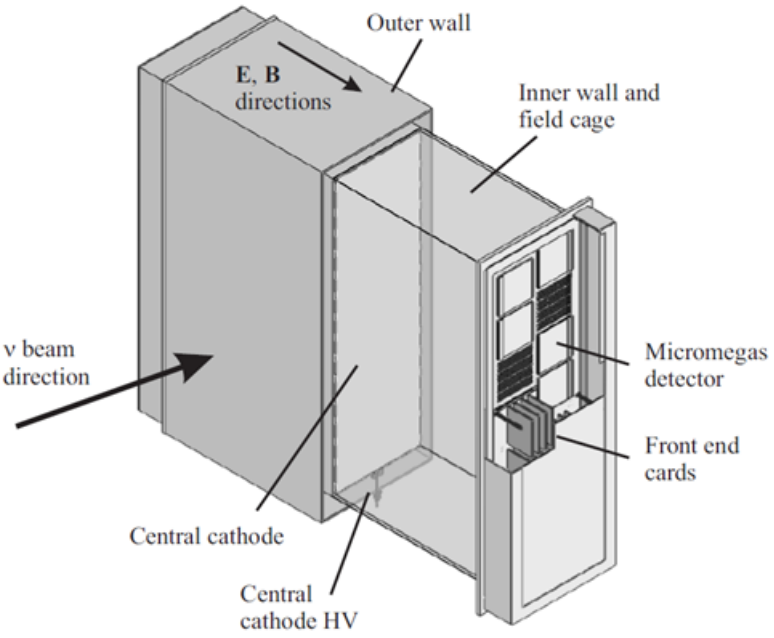


Figure 3.10: A schematic of the TPC, charged particles ionise the gas as they travel, causing a trail of electrons which are then drifted to the read-out planes with a uniform electric field. Spatial and timing information from these ionisation electrons allows for 3D track reconstruction and energy-loss measurement. Figure taken from [91]

electronics. The position of the drifted electrons (y and z directions) and their time of arrival (x direction) allow for three dimensional track reconstruction, in addition to a total energy loss measurement. A schematic of the TPC is shown in Figure 3.10.

3.3.3 Scintillator Read-Out

All of the scintillator sub-detectors in the T2K near detectors (PØD, FGD, ECal, SMRD and INGRID) are read out using wavelength shifting fibres, connected to Hamamatsu multi-pixel photon counters [93] (MPPCs) running in Geiger mode.

Each MPPC is made up of 667 silicon avalanche photo-diodes, read out by a single anode, operating at a sufficiently high reverse bias voltage that a single

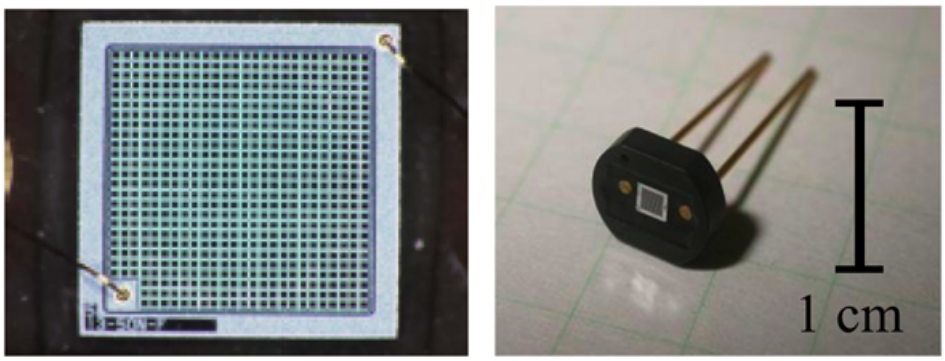


Figure 3.11: An image of an MPPC (right) and a close up of the photo-sensor array (left). Each MPPC has 667 silicon pixel diodes which operate above breakdown voltage, causing a discrete signal proportional to the number of incident photons. Photo taken from [91]

incident photon on one of the photo-diodes results in cascading electron-hole production, resulting in a discrete pulse of charge of fixed size. A measurement of the number of incident photons can then be made by measuring the signal from the MPPC, with a some correction for linearity at higher charges [94].

In all the scintillator detectors except the FGDs, the MPPCs are read-out using TRIP-t Frontend Boards (TFBs). Each MPPC is connected to one channel on the TFB, which is split into a high gain and low gain channel on the board. The reason for the charge splitting is to provide a larger range over which the MPPCs can be read out to a reasonable degree of precision than would have been provided by a single channel. Each TFB consists of four TRIP-t ASICs, each of which has sixteen low gain and sixteen high gain readout channels, which produce analogue voltages, which are then passed to an external analogue to digital converter (ADC) to give 10-bit ADC counts. Each of these channels has 23 capacitors that are used for charge integration. The integration time for each capacitor is 480 ns, separated by a 100 ns reset period. Further details of the electronics, and details of the calibration of the TFBs can be found in Chapter 4 of this thesis.

Up to 48 TFBs are connected to a single Readout Merger Module (RMM) backend board, which read out the ADC counts and controlling the TFB operation mode. The RMMs in turn are connected to the Frontend Processing Nodes (FPNs) that write out data in a form that can be used in the offline analysis.

3.4 The Far Detector: Super-Kamiokande

The T2K far detector, Super-Kamiokande, is a 50 kt water Čerenkov detector previously used to study atmospheric and solar neutrinos. The detector is made up of two parts, both water Čerenkov detectors, the Inner Detector (ID) and the Outer Detector (OD). The ID is a cylinder 33.8 m in diameter and 36.2 m in height and is separated from the OD by a cylindrical stainless steel structure. The OD extends 2 m from the edge of the ID in both radial and vertical directions. A schematic of the Super-Kamiokande detector can be seen in Figure 3.12.

The ID is read out by 11 129 PMTs, attached to the inner edge of the steel cylinder, giving a total of 40% PMT coverage. Each Hamamatsu R3600 hemispherical PMT is 50 cm in diameter, and has a photon detection efficiency (PDE) of 20%. The stainless steel structure surrouding the ID is lined with plastic sheets which prevent reflection of light from within the ID, and transmission of light from the OD into the ID.

The OD is read out by 1 885 PMTs on the outer edge of the stainless steel cylinder. Each PMT is 20 cm in diameter, and the OD is lined with highly reflective material due to the relative sparsity of its PMT coverage. The OD serves to veto cosmic muon events, or other radioactive events where a particle enters the detector from the outside. Due to the cut around the beam time for T2K running, the probability to have a cosmic muon at the same time is actually very low.

Calibration of the detector is performed from cosmic rays and a laser light

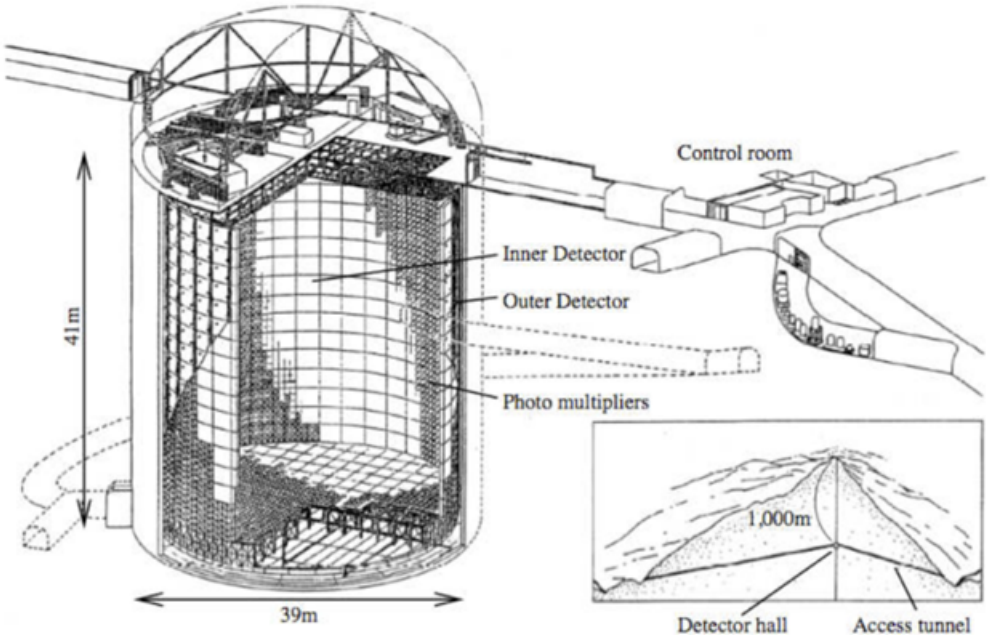


Figure 3.12: A Schematic of Super-Kamiokande. The water volume is split into a well instrumented inner detector (40% PMT coverage), and a more sparsely instrumented outer detector which is used to veto events that come into the detector from the outside. Figure from [91]

source.

3.4.1 Particle Identification from Čerenkov Radiation

When a charged particle travels faster than the speed of light in a medium, it emits Čerenkov radiation. Charged current quasi-elastic (CCQE) neutrino events are primarily used for T2K analyses as a single charged particle in the final state leads to clear particle identification (PID).

When ν_μ CCQE interactions occur, a single muon is created in the final state which emits a ring of Čerenkov radiation. As muons are relatively massive, they do not scatter much on their path through the detector, resulting in a very well defined Čerenkov ring, a typical example of which can be seen in Figure 3.13. Sometimes the muon will stop in the detector, leading to a delayed

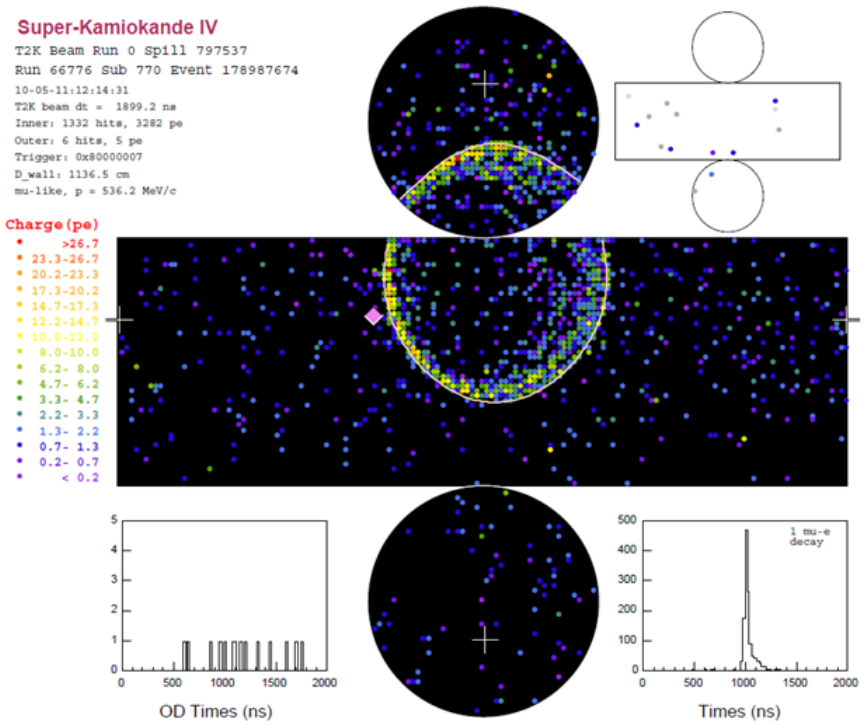


Figure 3.13: A typical ν_μ Čerenkov ring in Super-Kamiokande, formed when the μ^- produced in a charged current ν_μ interaction travels faster than the speed of light in water. Image from [91]

electron-like ring from the Michel electron.

CCQE interactions of ν_e, however, leave a single electron in the final state which is relatively light and scatters heavily along its path. This causes lots of small segments of Čerenkov light from the different trajectories the electron has been on to be emitted, essentially giving an overlap of multiple cones of Čerenkov light to form a fuzzy ring, a typical example of which can be seen in Figure 3.14.

3.5 Monte Carlo Simulation

The simulation of neutrinos in T2K starts with the simulation of the production of the neutrino beam. The neutrino beam is simulated by Monte Carlo (MC) that is then re-weighted by hadron production data from the dedicated hadron

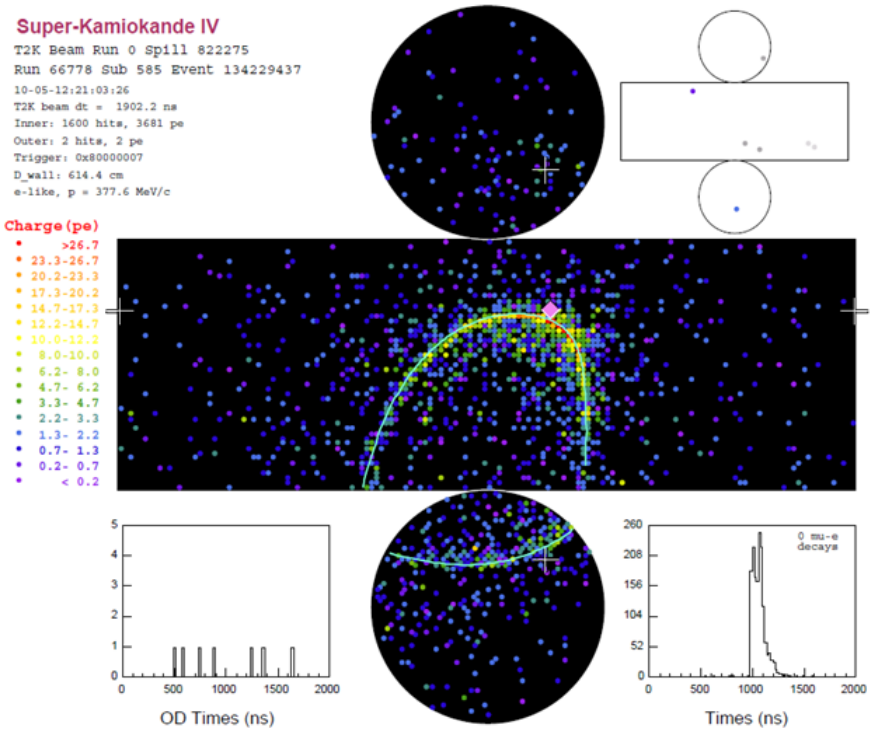


Figure 3.14: A typical ν_e Čerenkov ring in Super-Kamiokande, formed when the e^- produced in a charged current ν_e interaction travels faster than the speed of light in water. Image from [91]

production experiment at CERN, NA61/SHINE [100, 101]. The NA61/SHINE experiment measures hadron production off a graphite target by a 30 GeV proton beam provided by the CERN SPS. They have run with two different graphite targets: a thin target to measure proton primary interactions, and a T2K replica target to measure all interactions.

In the neutrino beam MC, the primary proton interactions in the target are simulated, ensuring that they agree with the NA61/SHINE thin target data. Subsequent secondary, tertiary *etc.* interactions in the target are then simulated by the FLUKA [102] package. Interactions in the material surrounding the target are also modeled using GEANT3/GCALOR [103].

Once the neutrino beam has been simulated, the neutrino interactions in the ND280 need to be simulated. The ND280 detector geometry is simulated with the GEANT4 [104] package and neutrino interactions within this geometry are

simulated by two different neutrino interaction generators: GENIE [105] and NEUT [106]. The propagation of the final state particles through the ND280 and their energy deposits are modeled with GEANT4. The response of the ND280 scintillators, MPPCs and electronics is then simulated with a custom built package, `elecSim`.

Neutrino interactions in Super-Kamiokande are also simulated with both NEUT and GENIE. The Super-Kamiokande detector simulation package (SKDETSIM), which is also based on GEANT3, is then responsible for propagating the final state particles through the detector. Hadronic interactions in the water are simulated by a combination of CALOR [107] and custom code [108].

3.6 T2K Physics

3.6.1 Electron Neutrino Appearance: The Search for θ_{13}

The main goal of the T2K experiment is to measure θ_{13} from oscillations $\nu_\mu \rightarrow \nu_e$, which is done by looking for ν_e appearance at Super-Kamiokande. The predicted sensitivity to θ_{13} can be seen in Figure 3.15.

T2K have released two electron neutrino appearance results, one from the first two run periods [113], and one from the first three run periods [43]. In the first result, six ν_e candidates were observed, against an expected background of 1.5 ± 0.3 events for the first two run periods. This was inconsistent with the $\theta_{13} = 0$ hypothesis at 2.5σ. Allowed values for $\sin^2 2\theta_{13}$ and δ, at 90% and 68% confidence levels, for this analysis, can be seen in Figure 3.16. The work presented in this thesis will use the Run 1+2 dataset. The data and allowed confidence level regions from the Run 1+2+3 analysis can be seen in Figures 3.17 and 3.18 respectively.

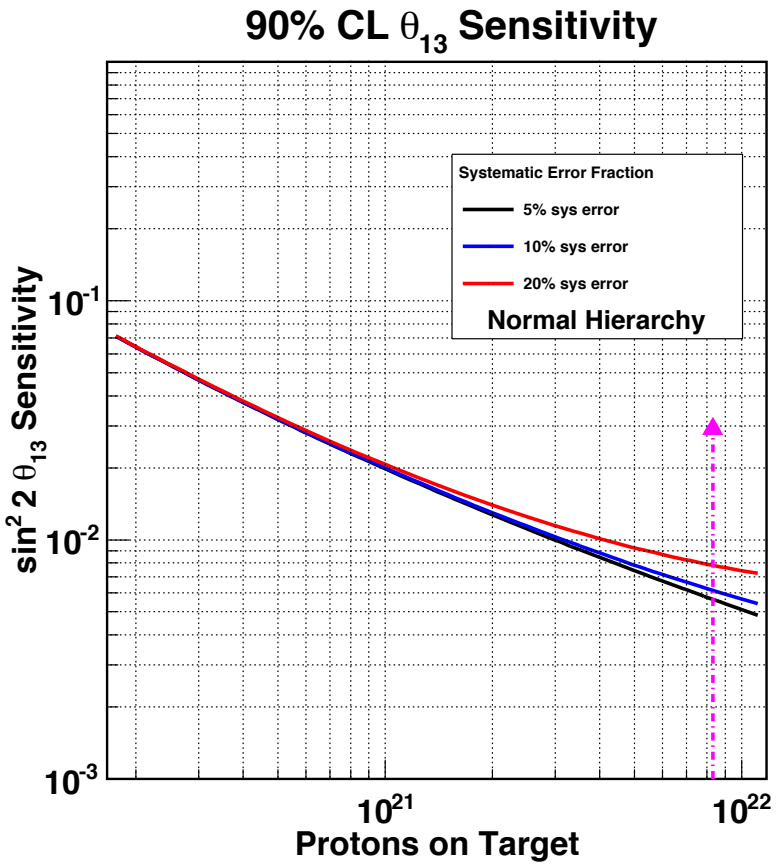


Figure 3.15: T2K sensitivity to θ_{13} at the 90% confidence level as a function of protons on target. 5%, 10% and 20% systematic error fractions are plotted. The dashed arrow indicates a 5-year run. The following oscillation parameters are assumed: $\sin^2 2\theta_{12} = 0.8704$, $\sin^2 2\theta_{23} = 1.0$, $\Delta m^2_{21} = 7.6 \times 10^{-5}\text{eV}^2$, $\Delta m^2_{32} = 2.4 \times 10^{-3}\text{eV}^2$, $\delta = 0$, normal hierarchy ($m_3 > m_2, m_1$). Plot taken from [109]

3.6.2 Muon Neutrino Disappearance: Precision Measurement of θ_{23} and Δm^2_{32}

The energy dependent deficit of ν_μ events at Super-Kamiokande is used to measure the oscillation parameters Δm^2_{32} and θ_{23}. The shape of the ν_μ energy spectrum is fit to extract these parameters. Ultimately, T2K aims to measure Δm^2_{32} to a precision of 10% and $\sin^2 2\theta_{23}$ to a precision of 1% [90].

T2K have presented the muon neutrino disappearance results from their first two run periods [112], the muon neutrino energy spectrum is shown in

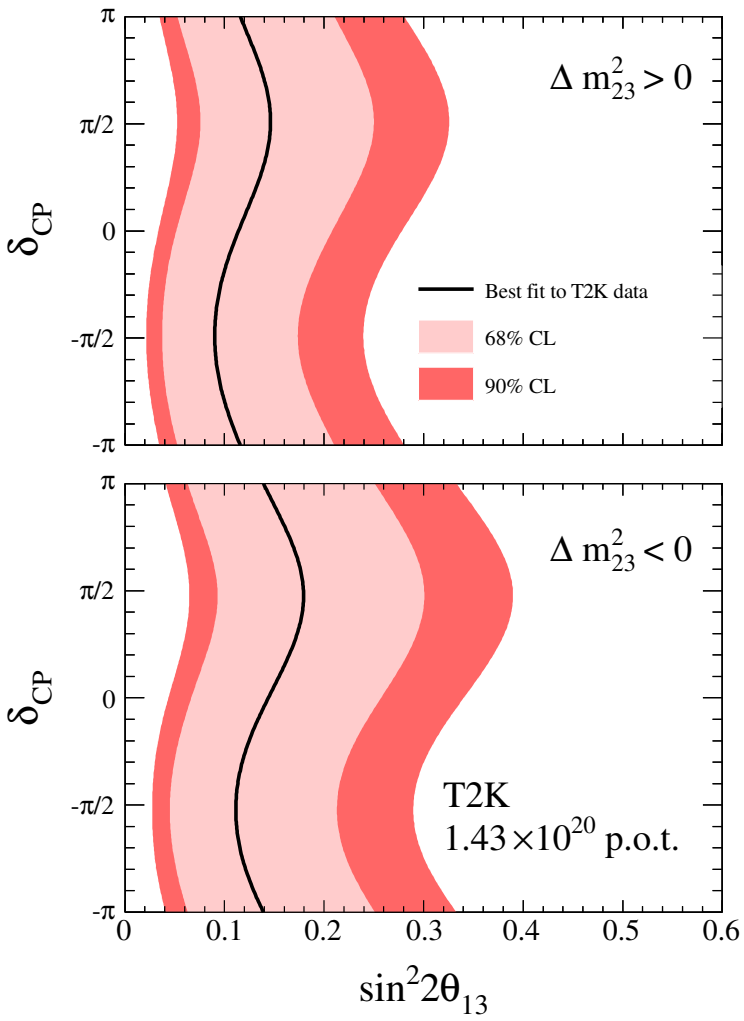


Figure 3.16: The Feldman Cousins allowed regions for the parameters $\sin^2 2\theta_{13}$ and δ at 90% and 68% confidence levels from the first two T2K run periods. Plot from [110].

Figure 3.19. The sensitivity to ν_μ is not quite at the level of MINOS [38], but many more protons on target are expected in the coming months and years.

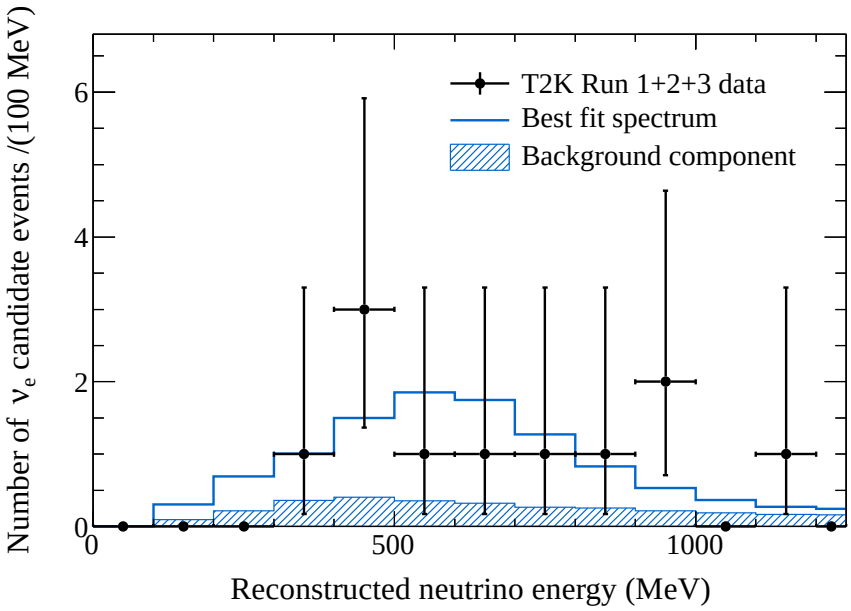


Figure 3.17: The ν_e candidates from the first three T2K run periods. Updated version of a plot from [43].

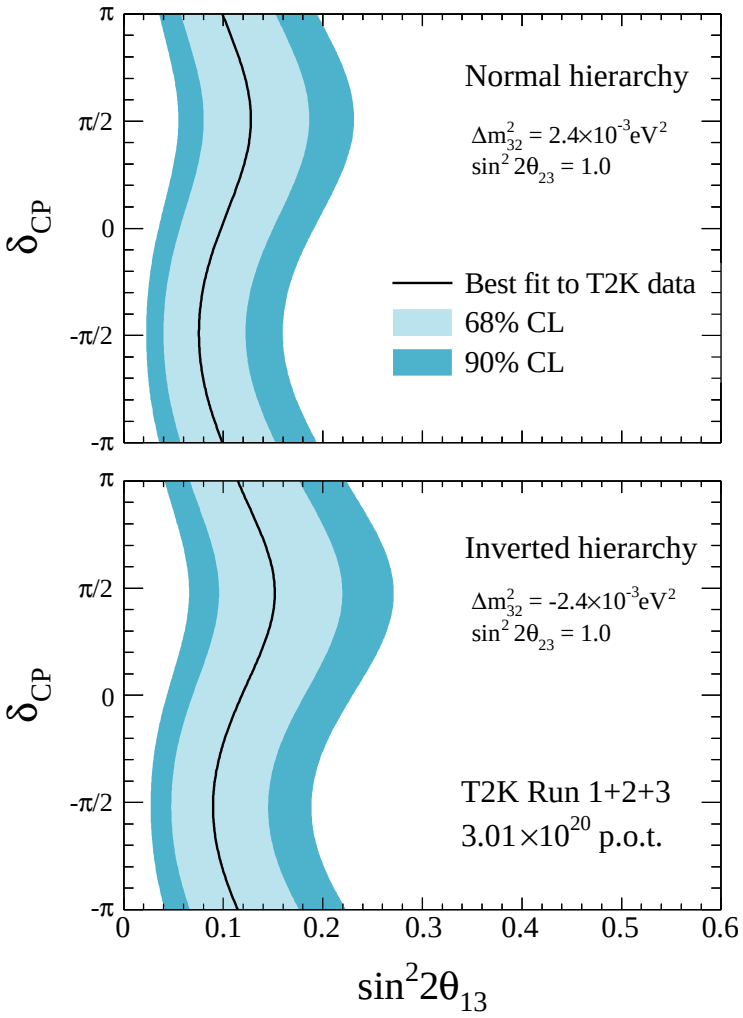


Figure 3.18: The allowed regions for the parameters $\sin^2 2\theta_{13}$ and δ at 90% and 68% confidence levels from the first three T2K run periods. Updated version of a plot from [43].

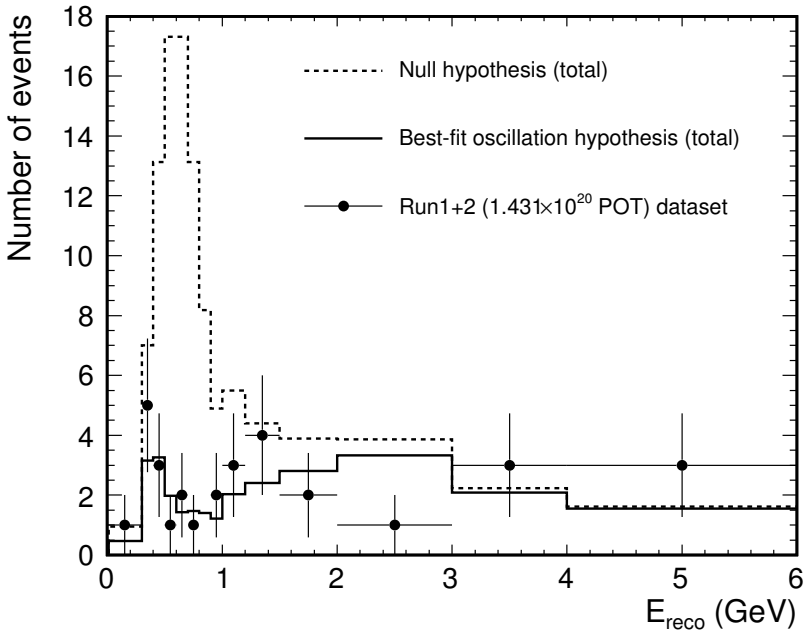


Figure 3.19: The T2K measured ν_μ energy spectrum and predictions in the case of no oscillations (dashed line) and the best fit to oscillations (solid line). Plot from [111]

Chapter 4

ND280 TRIP-t Electronics Calibration

This chapter describes the calibration of the TRIP-t frontend boards (TFBs), which are used to read out signals from three of the ND280 sub-detectors: ECal, PØD and SMRD, as well as the on-axis near detector, INGRID. The chapter begins with a description of the TFB and its connection to the MPPCs, in Section 4.1. Following is a description of the need for and implementation of the different types of TFB calibration: firstly the non-zero response to zero input charge, the pedestal calibration, in Section 4.2, and then the non-linearity of the electronics' response to input signal size, the non-linearity calibration, in Section 4.3.

4.1 The TRIP-t Electronics

The TFB was designed for use in the T2K near detectors. It utilises the TRIP-t chip that was created for use in the D0 experiment at the Tevatron [114, 115]. Each TFB contains four TRIP-t chips, each of which is connected to 16 input channels, so each TFB can be connected to up to 64 MPPCs. The MPPCs are

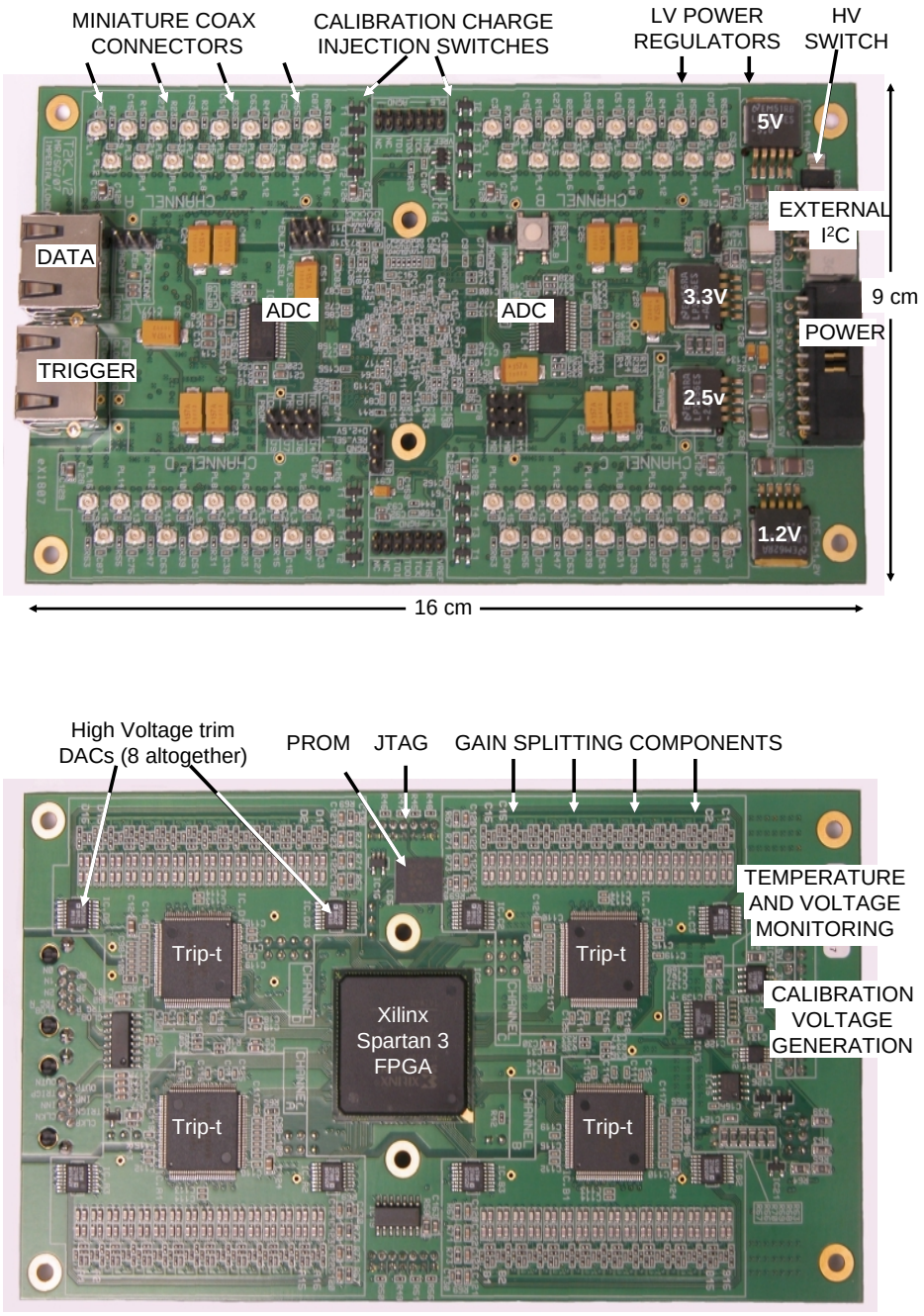


Figure 4.1: Top (above) and bottom (below) views of the TRIP-t frontend board (TFB) used in the T2K ND280. Photos from [116]

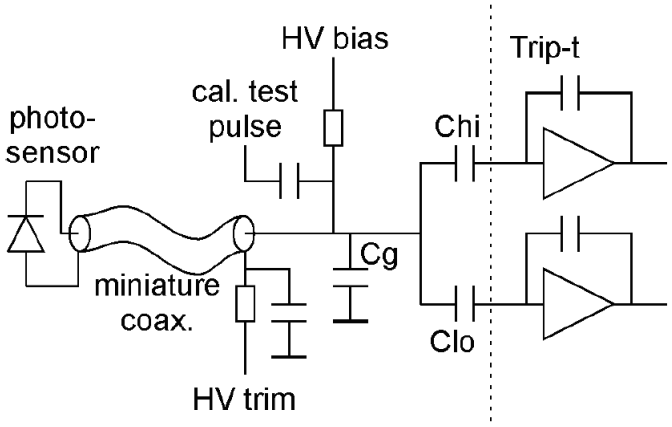


Figure 4.2: Schematic of part of the TFB electronics and connection to the MPPC. Figure from [92]

connected to the wavelength shifting (WLS) fibres used to transport light out from the scintillator bars in the PØD, ECal, SMRD and INGRID. The MPPC and scintillator readout was discussed previously in Section 3.3.3. In total there are over 50 000 channels in use to read out from these ND280 (sub-)detectors. Images of the T2K TFB can be seen in Figure 4.1. The TRIP-t chips can be seen in the bottom view, and the connectors to the MPPCs (miniature coax connectors) can be seen in the top view.

A diagram of the circuit connecting an MPPC to the TRIP-t chip on the TFB can be seen in Figure 4.2. Each MPPC is connected to a channel on the TFB, which is then split into a high gain channel and a low gain channel, each of which is connected to a channel on the TRIP-t, to give both high precision read-out of small signals and a large range of signals that can be read out [116]. The high gain channel provides a time stamp if the charge crosses a programmable discriminator threshold. The TFB also supplies the high voltage to the MPPC ($\sim$ 70 V), and can supply a calibration test pulse to groups of the channels, which will be discussed in more detail in Section 4.3.

The TRIP-t chip contains 23 capacitors for each channel. The charge coming

from each channel is amplified for a period of 480 ns and stored in one of the 23 capacitors. At the end of this integration period, there is a 100 ns reset period, before the amplification cycle begins again, switching to the next capacitor. In this way 23 integrated charges can be stored for readout. There are different modes that the readout can operate in, and these will be discussed in 4.2. The signals output from the TRIP-t are then digitised by the two on-board two channel analogue to digital converters (ADCs).

4.2 Pedestal Subtraction

In the absence of any signal from the MPPCs, the TFB channels still output ADC counts due to noise in the electronics, which is referred to as the pedestal. Typical dark noise spectra can be seen in Figure 4.3. For the high gain channels, in addition to the pedestal peak, a distinctive MPPC pixel peak structure can be seen due to the background rate of individual (or multiple for the higher peaks) pixels firing on the MPPCs. The reason this is not visible for the low gain channels is that the low gain channels are much less sensitive to small input charges, so the pixel peaks are merged with the pedestal peak. The pedestal peak is different for each channel and capacitor (as used in the integration cycles in the TRIP-t), and not constant in time (with a particular inverse dependence on temperature, see Section 4.2.1).

There are two different ways in which the 23 capacitors of each high and low gain channel can be filled and read out: “beam” mode and “cosmic” mode. In the beam triggering mode, no charge integration occurs until a trigger is received, at which point the 580 ns integration/reset cycle begins, starting with the first physical capacitor, and continuing until 23 cycles are complete, filling each physical capacitor in order. The 23 cycles are then read out.

In the cosmic triggering mode, the integration/reset cycles occur continu-

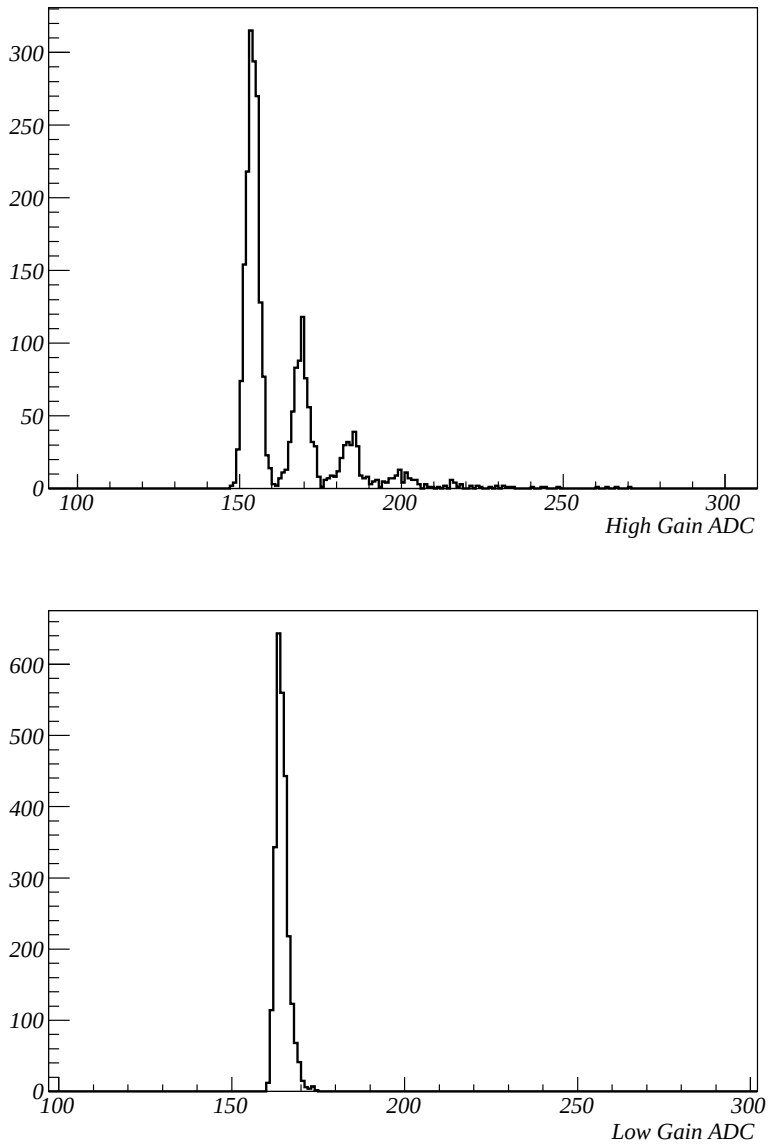


Figure 4.3: Pedestals in the high and low gain channels. In addition to the pedestal peak, MPPC pixel firing peaks can be seen in the high gain channel. The pedestal is found by fitting a Gaussian to a symmetric 9.9 ADC (calculated to be on average $\pm 3\sigma$) range centered on the mode of the distribution.

ously, filling the different capacitors in order and then looping back over them. When a cosmic trigger is received, this integration/reset cycle is stopped, and the charges from all of the 23 capacitors are read out. Due to the delays between a cosmic event occurring, the trigger being issued and the stopping of the integration/reset cycle, the cosmic event will occur some cycles before the last one to be filled. This means that for each cosmic trigger, a number of cycles before and after the event are also read out. Due to the continuous cycling of integration/reset and the uncertainty in when a cosmic trigger will arrive, the first capacitor to be read out will not in general be the first physical capacitor.

Depending on whether the triggering is in beam or cosmic mode, the value of the pedestal from the different capacitors will be different, as can be seen in Figure 4.4. In these plots, the z-axis is the value of the pedestal for the capacitor minus the pedestal for capacitor 14 (assumed to be typical) in high gain ADC.

In beam mode, the physical capacitor and integration cycle numbers are the same. The pedestal in the first capacitor to be read out is significantly different from the others since this capacitor contains the charge from the first integration cycle, before which the electronics was waiting. This difference in the first capacitor is not present when running in cosmic mode, since in this case there is only a 100 ns reset period before the filling of the first physical capacitor, as with all of the other capacitor in this mode. In both beam and cosmic mode, the pedestal of physical capacitor 21 is quite different from the other pedestals. This feature is not understood, but it is calibrated out. It it also possible to see the four different TRIP-t chips in, they correspond to the different vertical columns of 16 high gain channels each.

The difference between the pedestals in different integration cycles in cosmic trigger mode can be seen in Figure 4.5. As with the beam mode trigger, there is a difference between the first readout cycle and the others, and also a difference in the last readout cycle. In cosmic mode it is the physical capacitor

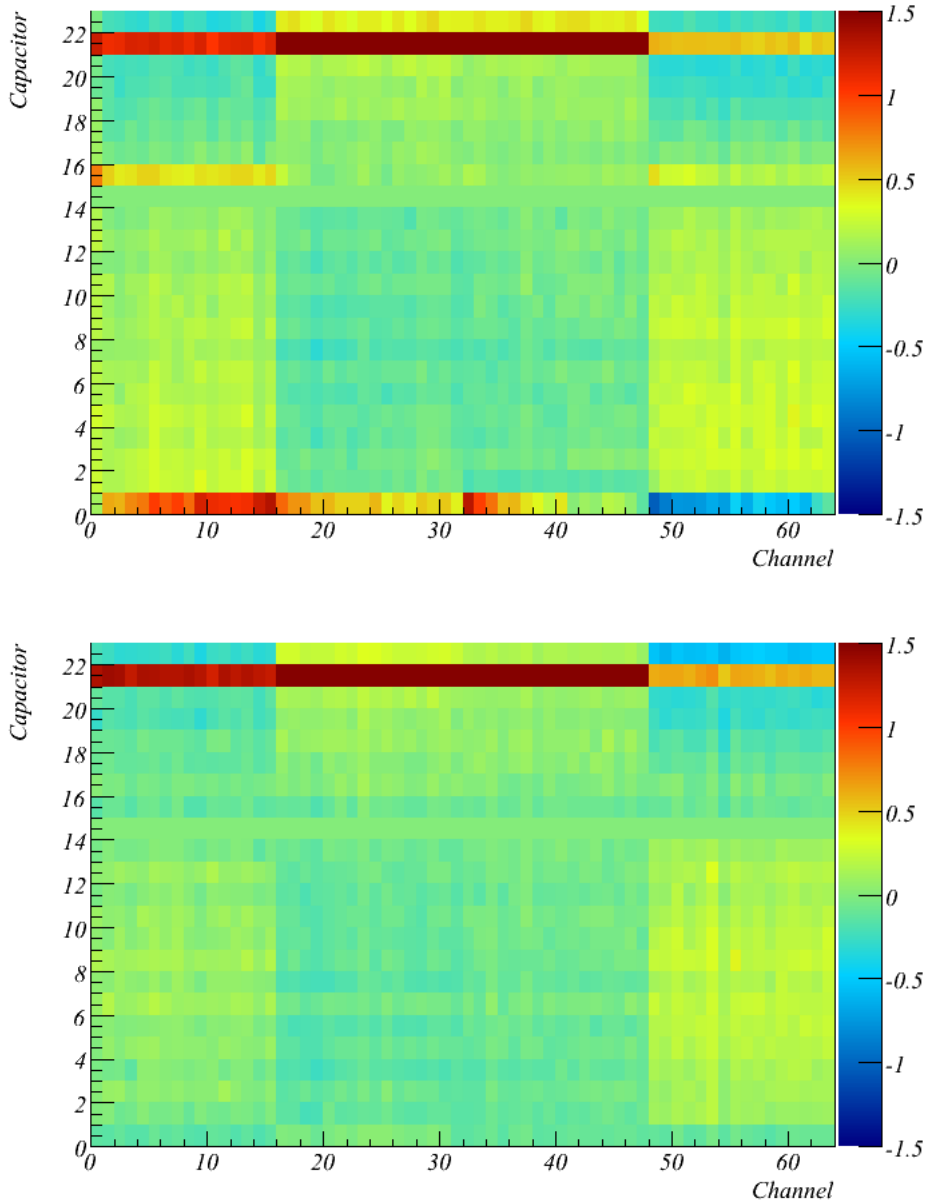


Figure 4.4: The different values of pedestal in the capacitors of the channels of a TFB in beam (above) and cosmic (below) triggering modes. The Elevations shown are in high gain ADC from the value of capacitor 14 - assumed to be typical.

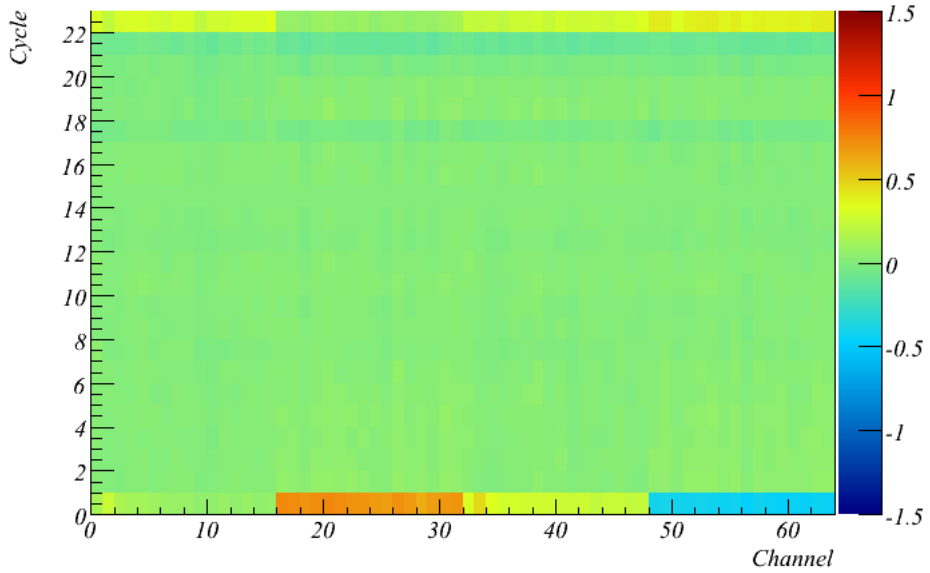


Figure 4.5: The different values of pedestal in the different readout (integration) cycles of the channels of a TFB in cosmic triggering mode. The Elevations shown are in high gain ADC from the value of readout cycle 14 - assumed to be typical.

used for each cycle that is most important in determining the pedestal for that cycle, rather than the cycle's position in the 23-cycle read-out.

The pedestal is calculated by fitting a Gaussian to a symmetric 9.9ADC (calculated to be on average $\pm 3\sigma$) range centered on the mode of the distribution. The idea of limiting the range over which the Gaussian is fit is to limit the bias that can be caused by the presence of the pixel firing peaks found to the right of the pedestal peak. The error on the mean of the fitted pedestal is ~ 0.1 ADC for a one thousand event pedestal run. The result of applying the pedestal subtraction to a dark noise run can be seen in Figure 4.6.

4.2.1 Variation of Pedestal

The pedestal varies when the temperature changes, decreasing in value as the temperature increases. This variation can be seen in Figure 4.7. The tempera-

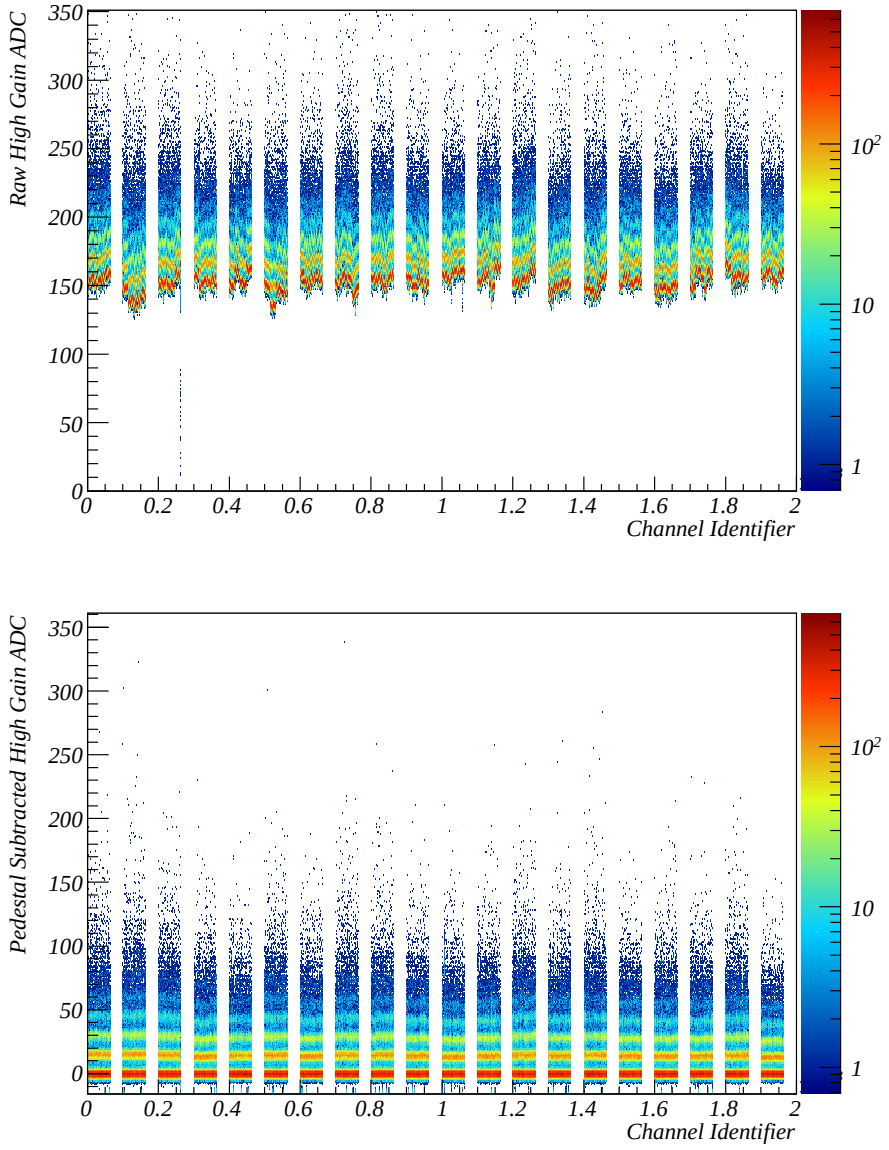


Figure 4.6: Top: The high gain pedestal distributions in various different DsE-Cal channels. Bottom: The result of applying the pedestal subtraction to these channels.

ture is read out from the TFB's on board temperature sensors. This behaviour is not fitted for, instead we intend to correct for it by taking regular pedestal data and updating the calibration regularly.

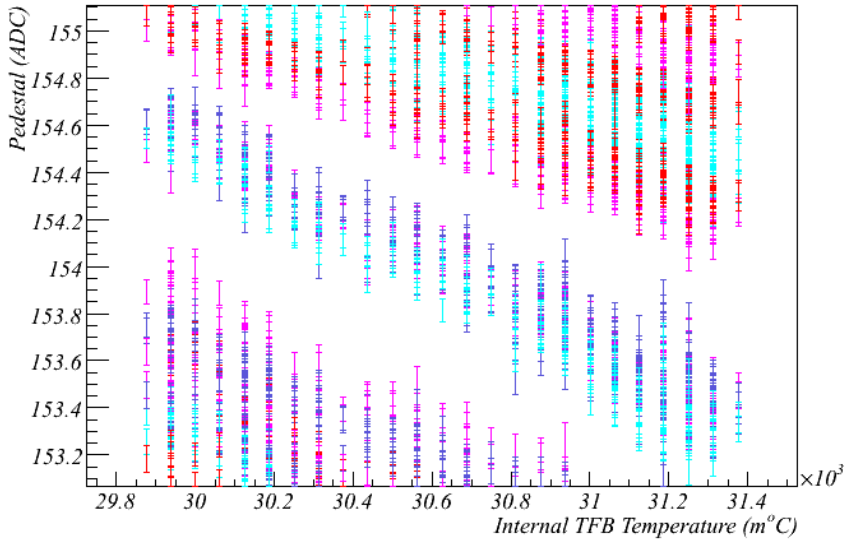


Figure 4.7: Variation of low gain pedestal with temperature for different channels (different colours) on a single TFB.

The fact that the pedestal is not constant with temperature will of course lead to a time variation, since the electronics will not be perfectly temperature stabilised.

The scale of the time variation of the pedestals, up to 0.1 ADC per hour, can be seen in Figure 4.8. This shows differences between a number of pedestal runs taken with the DsECal at the test beam run at CERN, over a period of ten hours. At the start, two runs were taken in quick succession. The peak at zero time is the difference between the pedestals (for each channel and capacitor) in these two runs *i.e.* it represents the combination of the error on the mean of the two pedestal peaks. The later peaks are filled with the difference between each pedestal at that time, and that pedestal at zero time. The average value of the calculated pedestals can clearly be seen to move over time, and the pedestal

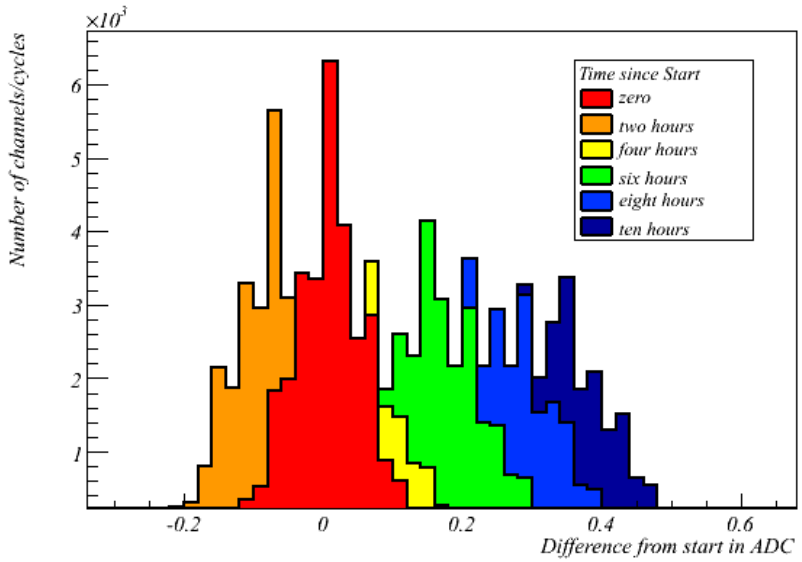


Figure 4.8: The change of high gain pedestals on an ECal RMM over a period of ten hours.

values for the different channels also decohere over time. This drift must be corrected for.

To put these time variations, of around 0.5 high gain ADC, in perspective: the single photo-electron (pe) peak is at around 10 ADC, and a cosmic muon corresponds to about 20 pe, so the pedestal variations are much less than 1% of the signal from cosmic muons.

4.2.2 Pedestal Calibration Strategy

Taking the unsparsified runs necessary to calculate pedestals is not possible with sufficient regularity during neutrino beam running. In normal running, hits from a channel are only saved if either the high gain or low gain ADC is above some threshold (can be changed but is mostly set to around 2.5 pixel equivalent), or the channel outputs a time stamp, which occurs if the discriminator threshold is crossed (set to be around 2.5 pe equivalent). Instead, the data acquisition system (DAQ) fills histograms with all hits before they are sparsi-

fied, as part of the Data Processing Task (DPT). However, due to memory usage constraints, all the capacitors from each channel have their hits stored in the same histogram, meaning that these histograms cannot be used in isolation to perform the pedestal calibration for each of the capacitors.

Instead, they can be used in combination with less frequent complete pedestal runs. The pedestal values for all channels and capacitors are calculated from dedicated runs which are taken infrequently, and then all the pedestals are drifted according to the change in the average pedestal for that channel:

$$\text{Pedestal}_{\text{chan,cap}} = \text{Start Pedestal}_{\text{chan,cap}} + \Delta\text{Average Pedestal}_{\text{chan}}$$

That this method would work was demonstrated before the DPT histogramming functionality was in place by histogramming events from normal pedestal runs into the same histograms that would be available from the DPT histograms. Figure 4.9 shows the differences in the pedestal directly calculated from the pedestal run and that estimated from the average channel drift and the original full pedestal run at zero time. The histogram at zero time was produced using two pedestal runs taken one after the other. The fact that the spread in fitted and estimated pedestals for the different channels and cycles remains constant over time shows that the pedestals for the different cycles do not drift significantly with respect to each other over this period of time.

4.3 Non-Linearity Calibration

As previously mentioned, each TFB channel is split into a high and low gain channel, using different capacitances. In theory the high gain channel has a 100 pF capacitor, whereas the low gain channel has a 10 pF capacitor, leading to a ten times higher response to low charges for the high gain channel. In practice,

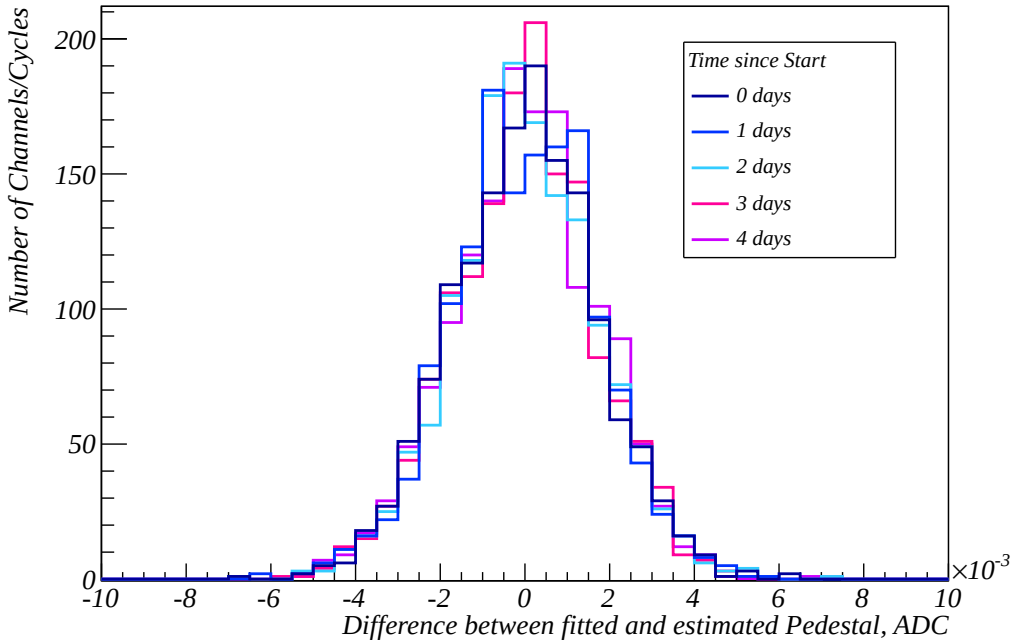


Figure 4.9: Trial of the method to correct different cycles' pedestals using the drift in the average pedestal for the channel.

however, there is a 5% standard deviation in the capacitance of each channel, leading to a spread of different responses to input charge in the different channels.

To measure the non-linearity in the charge response, we use the programmable charge injection circuit that is present on each TFB. This charge injection circuit is connected to all of the channels and provides a test pulse for calibration. The resolution of the charge injection is about 12 fC [116]. Four channels per TRIP-t can have charge injected at the same time, and the point in the integration cycle at which charge is injected can be controlled up to a resolution of 10 ns. The control of the time of charge injection point is necessary to ensure that the entire charge can be recorded during the 480 ns integration cycle.

Figure 4.10 shows the typical responses of the high and low gain channels to the charge injection. Both sets of channels will saturate for some value of

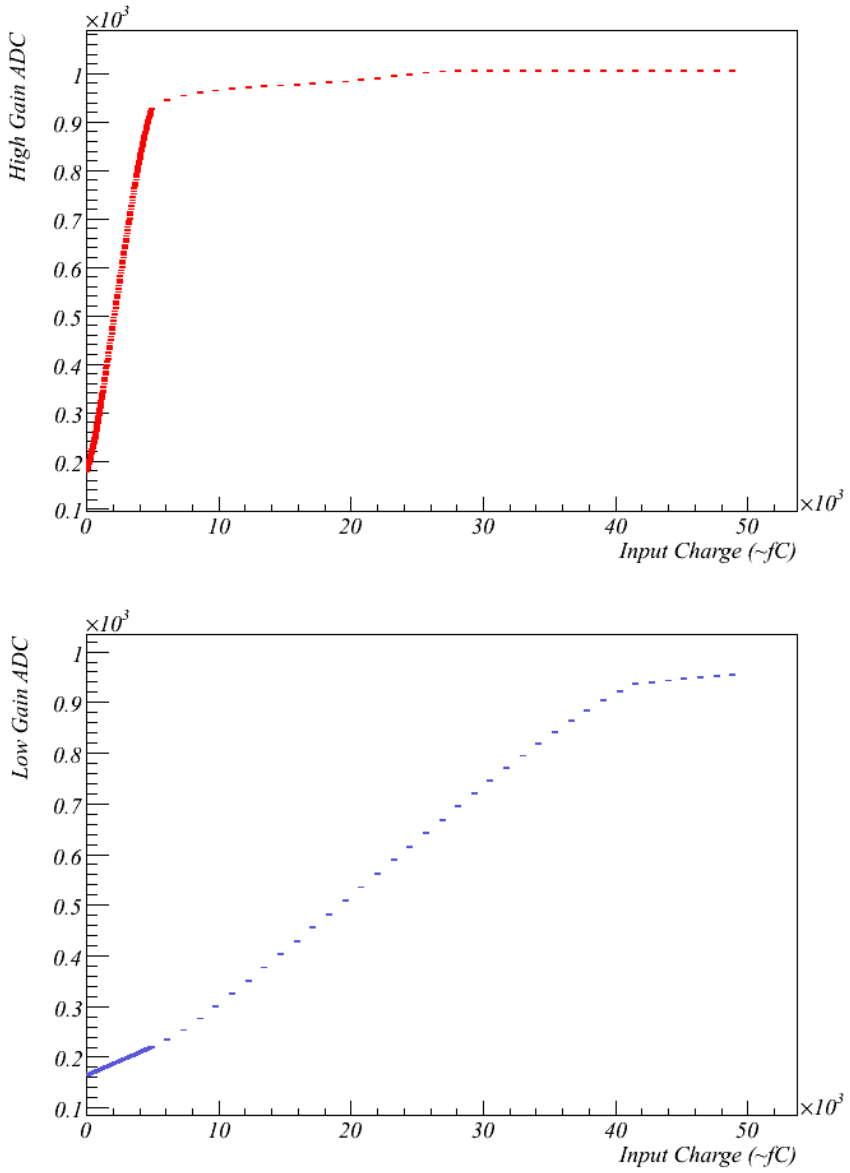


Figure 4.10: Example output ADC counts as a function of input charge, for high (red) and low (blue) gain channels. Here each input charge count is equivalent to about 12 fC [116].

input charge. The high gain channels will saturate at much lower values of input charge than the low gain channels, due to their different capacitances. The point at which saturation occurs also varies between channels. An elbow can be seen in the low gain channel at the point corresponding to the saturation of the high gain channel, as no further charge sharing occurs so the response of the low gain channel increases. The spread of responses in different channels to the charge injection can be seen in Figure 4.11. The saturation of the different channels can be seen clearly on the high gain plot especially: although the onset of saturation occurs at roughly the same input charge, the complete saturation occurs at very different input charges and in any case the behaviour is very non-linear after saturation.

There is a problem with the charge injection circuitry in that the requested charge is not delivered for some boards, this problem will have to be fixed by measuring the actual charge delivered to the channels by the charge injection circuit, with additional functionality not currently enabled. The effect can be seen for some channels with behaviour such as is seen in Figure 4.12. Currently the effect is removed when doing the charge injection calibration by assuming the true injected charge is offset by the amount the high gain channel remains flat for.

The high and low gain channel fits are made using two cubic polynomials superimposed using error functions,

$$\begin{aligned}\text{Input Charge} \quad &= \text{erfc}\,(x - p_0)\,(p_1 + p_2 x + p_3 x^2 + p_4 x^3) \;+ \\ &\quad (1.0 + \text{erf}\,(x - p_0))\,(p_5 + p_6 x + p_7 x^2 + p_8 x^3)\end{aligned}$$

where x can be the high or low gain ADC and the p_i are the fit parameters. Error functions are essentially smooth step functions, allowing for different regions of the calibration data to be fit almost independently, but still giving a contin-

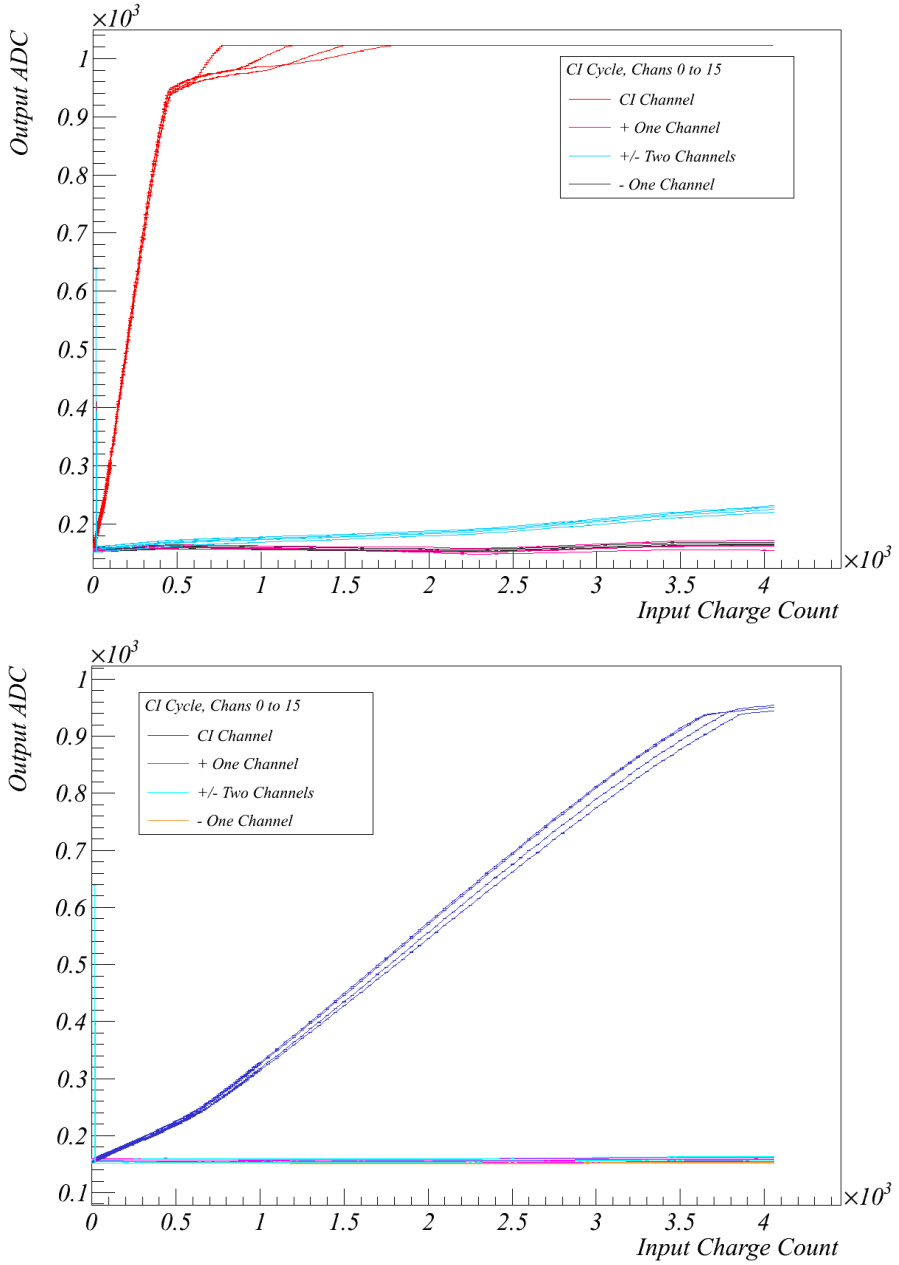


Figure 4.11: Example output ADC counts as a function of input charge, for high (above) and low (below) gain channels. Also shown are the responses of other channels (into which charge is not directly being injected) during the charge calibration runs. Cross talk up to about 1% of the input charge can be seen.

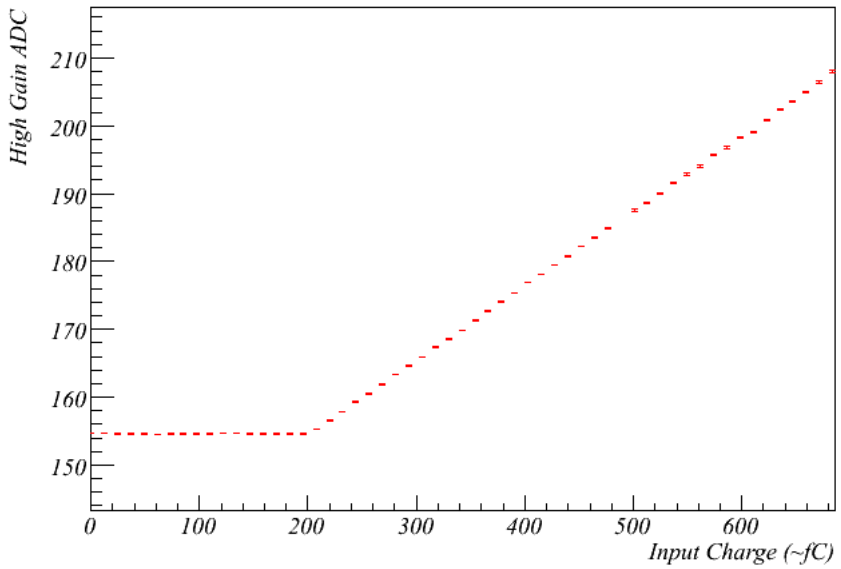


Figure 4.12: Example of charge injection circuit not outputting low charges when requested to. Shown here is the response of the high gain channel to the charge that was supposed to be injected.

uous differentiable function as the result. The error function and inverse error function are defined as:

$$\begin{aligned} \text{erf}(x) &= \frac{2}{\sqrt{\pi}} \int_0^x e^{-x'^2} dx' \\ \text{erfc}(x) &= 1 - \text{erf}(x) \end{aligned}$$

For the high gain channels, the range of the fit is truncated so that the saturated regions and the region before actual charge injection starts are excluded. For the low gain channels, only the range above saturation of the high gain channels and below the saturation point of the low gain channels are fitted. Successful calibration is defined as the residual everywhere being within 5% of the input charge. Example fits can be seen in Figure 4.13, and typical residuals can be seen in Figure 4.14. The fits have a high success rate (more than 99%, depending on how many points are taken in the charge injection run). If a fit cannot be made for a channel then a default polynomial is used instead for

its linearity correction. This default polynomial is calculated from the average values of the successful fit parameters for the DsECal.

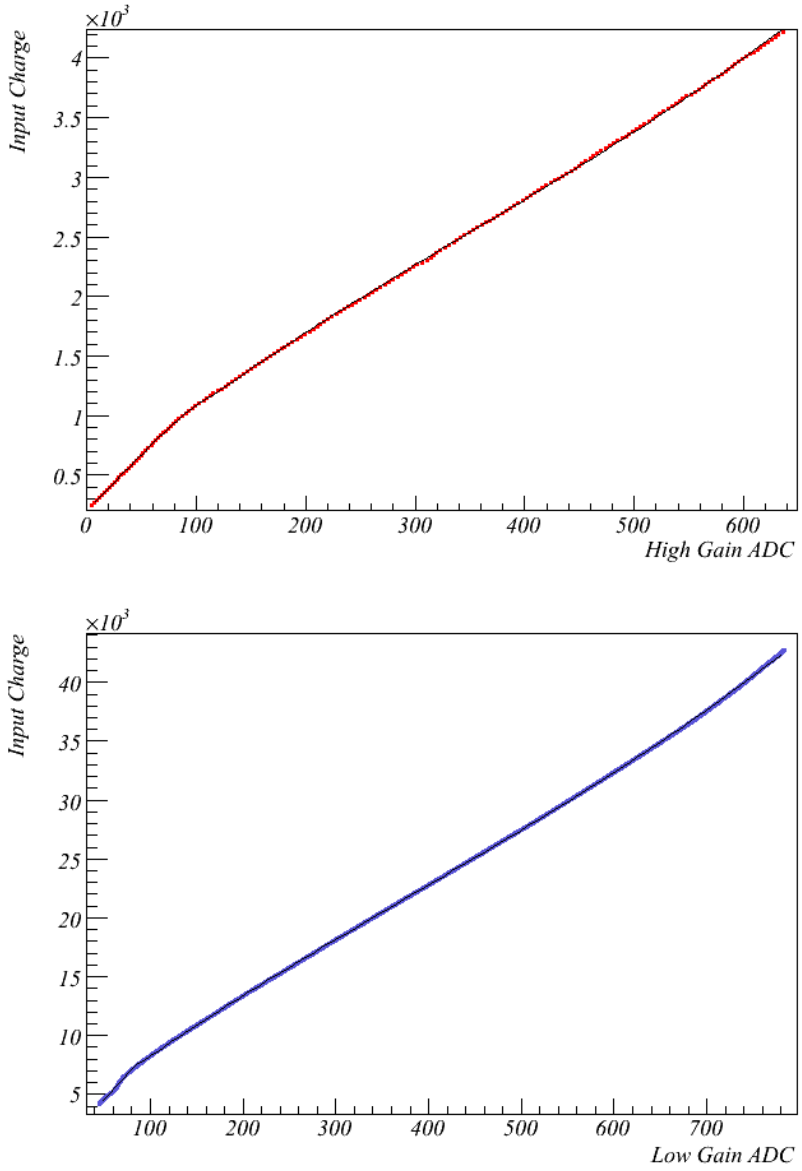


Figure 4.13: Examples of high (red) and low (blue) gain fits. Note that the dependent and independent values are swapped, as we want to know the input as a function of the output. The scale on the y-axis is the value of charge the circuit was instructed to supply.

The reason for fitting for the non-linearity of charge response rather than using splines between the points is to limit the amount of data in the database.

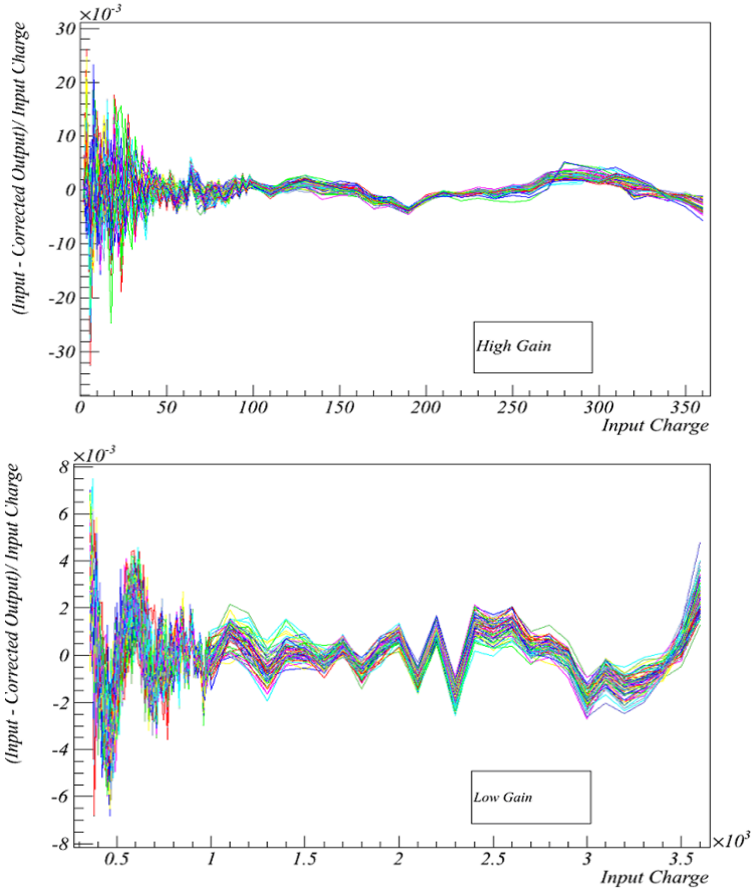


Figure 4.14: Residuals after fitting the non-linearity of the high gain (top) and low gain (bottom) channels of one ECal TFB.

With the polynomial fits only 23 parameters (9 for the high gain polynomial, 9 for the low gain polynomial, plus four to specify the ranges of the two polynomials and one error code) need to be stored for each channel, rather than the hundreds that would be required if using complete splines of the charge injection data. The reason for the limit in database size is to allow the database to be queried in reasonable times rather than due to any physical limits on what we can store. It is also important to fit the calibration data, rather than using all the points, to smooth out unphysical discontinuities due to the statistics of the calibration data.

4.3.1 Switching Between High and Low Gain Channels

The application of the non-linearity correction is complicated by the fact that the charge is read out by two channels per photo-sensor. For low charges, it is beneficial to use the high gain channel as it is more precise, but care must be taken to switch to the low gain channel before the high gain channel saturates. The relationship between the linearised ADC of the high and low gain channels for the DsECal during a cosmic run can be seen in Figure 4.15.

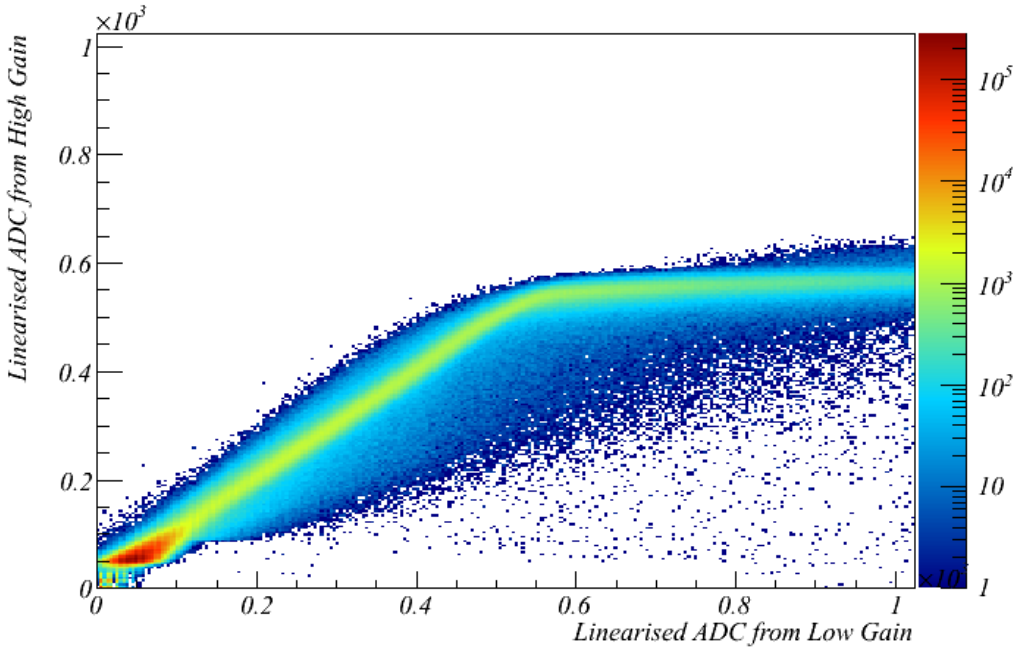


Figure 4.15: Relationship between linearised ADC for the high and low gain channels of the DsECal during a cosmic run. The high gain channel saturates at around 500 linearised ADC, whilst the low gain channel continues to give rising values of the linearised ADC.

The switching choice is performed using a combination of the result of applying the non-linearity correction to the low and high gain channels. If the sum of the two reconstructed charges is above 600 linearised ADC, and the original low gain ADC is above the minimum value used in making the low gain polynomial, then the low gain channel is used to calculate the result, oth-

erwise the high gain channel is used. In addition, both low and high gain channels must have valid constants (the fit must have been successful). The result of the linearity calibration is shown in Figure 4.16. Before this calibration is applied it is essential that the pedestal calibration has been applied correctly, otherwise discontinuities in charge can occur where the range switching occurs. This non-linearity calibration is now used for all of the ND280 off-axis TRIP-t subdetectors.

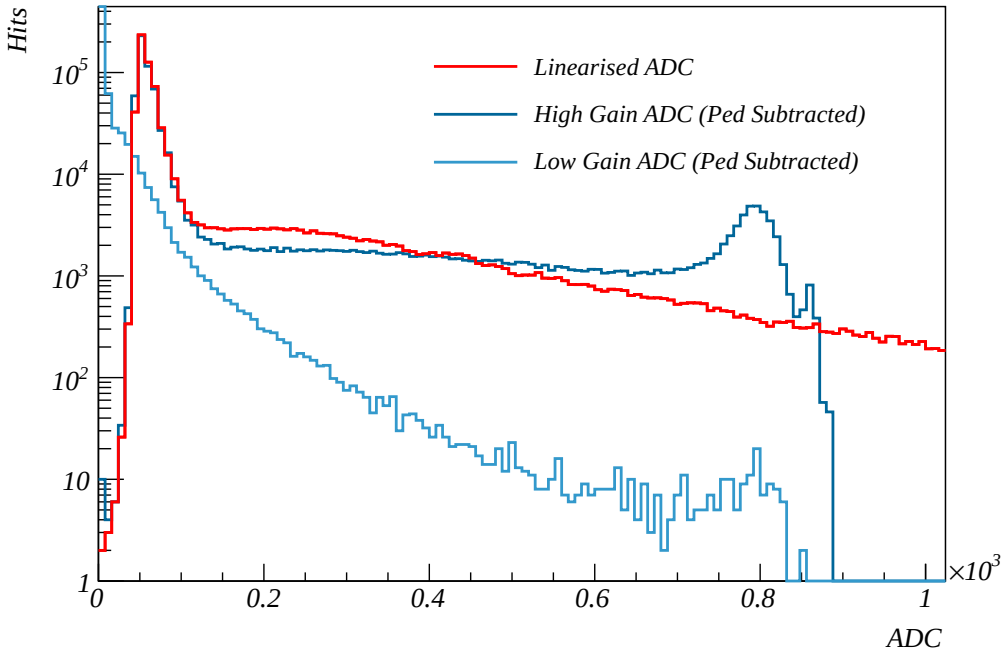


Figure 4.16: The linearised ADC for the channels of a DsECal TFB during a cosmic run. The pedestal subtracted high and low gain ADC counts are also shown. Note the saturation of the high gain ADC.

Chapter 5

Far Detector ν_e Appearance from Short Baseline Oscillations

In this chapter the possibility that the various short baseline anomalies discussed in Chapter 2 of this thesis (LSND, MiniBooNE, reactors *etc.*) could be caused by short baseline neutrino oscillations is considered. In particular, the fact that such short baseline oscillations could cause ν_e or $\overline{\nu}_e$ appearance in the T2K beam will be used to constrain the short baseline oscillation parameters Δm^2_{LSND} and $\sin^2 2\theta_{\text{LSND}}$. Some parts of the MiniBooNE allowed region presented in [120] can be excluded at $3\,\sigma$.

5.1 Possible Models for Including Sterile Neutrinos

As was discussed in Chapter 2, in order to explain the LSND $\overline{\nu}_\mu \rightarrow \overline{\nu}_e$ results in terms of neutrino oscillations, a new Δm^2, at least an order of magnitude ($> 10^{-2}\,\text{eV}^2$) greater than the other two mass-squared splittings, must be introduced. The simplest such scenario involves the addition of one sterile neutrino to the three active flavours; such models are known as 3+1 models.

After this choice, the issue is complicated somewhat by the fact that LSND

only sees a signal for oscillations $\overline{\nu}_\mu \rightarrow \overline{\nu}_e$ [49], but not for oscillations $\nu_\mu \rightarrow \nu_e$ [50]. These results in themselves are perplexing, as on the LSND baseline and energies no significant oscillations will occur driven by Δm^2_{32} or Δm^2_{21}, which means that we are essentially in a two-neutrino oscillation scenario. This means that a difference between the appearance probability for neutrinos and antineutrinos is equivalent to a difference in the survival probabilities for ν_μ and $\overline{\nu}_\mu$, *i.e.* represents $\mathcal{CPT}$-violation. More than two neutrino flavours are required for $\mathcal{CP}$-violation without $\mathcal{CPT}$-violation.

However, the nature of the LSND beam [48] means that the ν_μ beam is higher in energy than the $\overline{\nu}_\mu$ beam, which means that the oscillation probability could be the same for neutrinos and antineutrinos, but the ν_μ would not oscillate as they are above the peak oscillation energy. This possibility, combined with the fact that the latest results from MiniBooNE [120] suggest largely the same behaviour for neutrinos and antineutrinos, the fact that hints of short baseline electron-neutrino disappearance have been observed in both $\overline{\nu}_e$, from reactor experiments [55], and ν_e, from gallium experiments [56, 57, 58], means that a 3+1 scenario with no $\mathcal{CPT}$-violation is still worth consideration. The results of the MiniBooNE joint neutrino and antineutrino analysis can be seen in Figure 5.1.

If short baseline neutrino oscillations really are different for neutrinos and antineutrinos, it is necessary to be a little more speculative with the choice of model. Possible motivations for such a scenario include the different LSND neutrino [50] and antineutrino [49] results, and the slightly different energies of the peak oscillation probability seen by MiniBooNE [120]. One possibility is to just throw away $\mathcal{CPT}$-conservation, and assume that short baseline neutrino oscillations $\nu_\mu \rightarrow \nu_e$ either do not occur, or occur with different oscillation parameters to oscillations $\overline{\nu}_\mu \rightarrow \overline{\nu}_e$. A more conservative approach, since we have already introduced the concept of a sterile neutrino, is to introduce additional

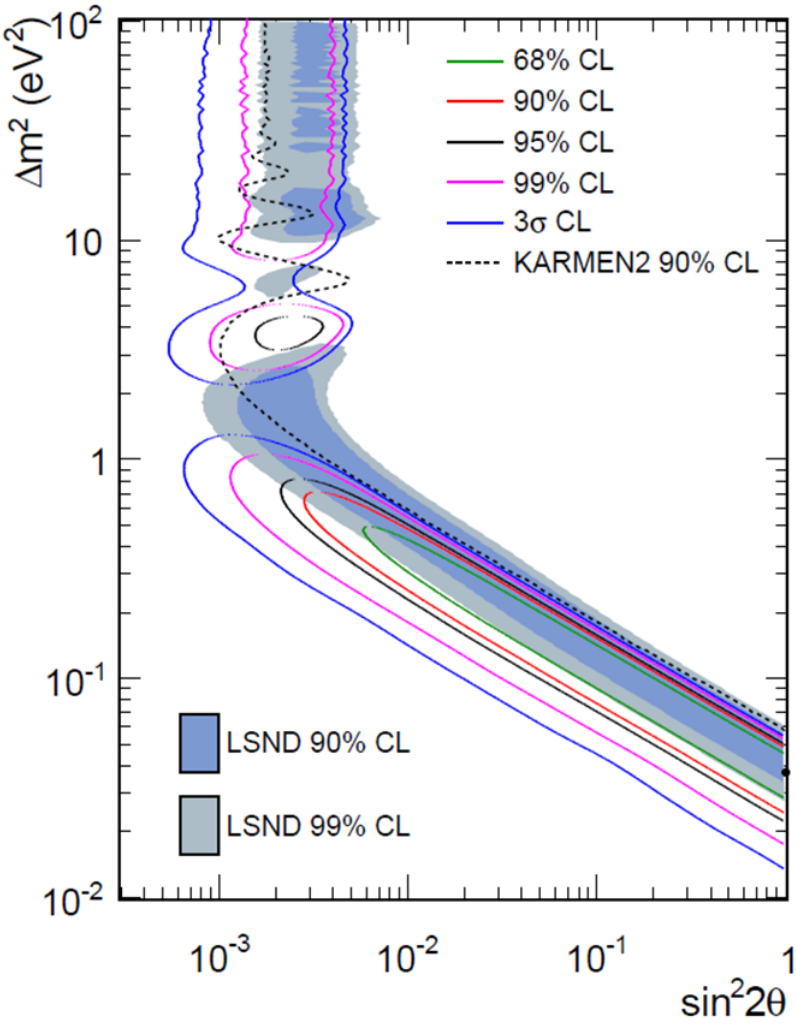


Figure 5.1: The MiniBooNE joint neutrino and antineutrino data allowed regions, plot from [120]. The LSND allowed regions, and the KARMEN exclusion limit (above and to the right of the contour is excluded at 90% CL) are also shown.

sterile neutrino species. Models with two sterile neutrinos are sufficient to introduce different behaviour in short baseline oscillations $\overline{\nu}_\mu \rightarrow \overline{\nu}_e$ and $\nu_\mu \rightarrow \nu_e$, using $\mathcal{CP}$-violation. In this thesis, however, the only model to be considered will be the 3+1 model with no $\mathcal{CPT}$-violation.

5.2 Theory of Sterile Neutrino Mixing

To calculate oscillation probabilities in the presence of an additional sterile neutrino, the PMNS mixing matrix needs to be expanded to a 4×4 matrix, with three new mixing angles and two new $\mathcal{CP}$-violating phases needing to be introduced to parametrise the new matrix. To define this expanded mixing matrix, the treatment used by the MINOS Collaboration in [117] will be followed, as it simplifies the algebra in the case (such as for T2K) that oscillations due to Δm^2_{21} can be neglected. The PMNS matrix is described in terms of rotation matrices, R, as in Chapter 2, with additional rotation matrices to include the new phases and mixing angles:

$$\begin{aligned} U &= R_{34}(\theta_{34})R_{24}(\theta_{24},\delta_2)R_{14}(\theta_{14})R_{23}(\theta_{23})R_{13}(\theta_{13},\delta_1)R_{12}(\theta_{12},\delta_3) \\ &= R_{34}(\theta_{34})R_{24}(\theta_{24},\delta_2)R_{14}(\theta_{14})R_{23}(\theta_{23})R_{13}(\theta_{13},\delta_1) \end{aligned} \tag{5.1}$$

Where the rotation matrices are, for example:

$$R_{34}(\theta_{34}) = \begin{pmatrix} 1 & & & \\ & 1 & & \\ & & c_{34} & s_{34} \\ & & -s_{34} & c_{34} \end{pmatrix} \tag{5.2}$$

$$R_{24}(\theta_{24},\delta_2) = \begin{pmatrix} 1 & & & \\ & c_{24} & & s_{24}e^{-i\delta_2} \\ & & 1 & \\ & -s_{24}e^{i\delta_2} & & c_{24} \end{pmatrix} \tag{5.3}$$

Here the standard $\mathcal{CP}$ phase is δ_1 and the new parameters are θ_{i4} and δ_2. If all of the new angles and phases are set to zero then the standard three neutrino mixing matrix is recovered, so θ_{13}, θ_{12} and θ_{23} have their usual meanings. The mixing matrix can then be expressed as follows:

$$U = \begin{pmatrix} U_{e1} & U_{e2} & c_{14}s_{13}e^{-i\delta_1} & s_{14} \\ U_{\mu 1} & U_{\mu 2} & -s_{14}s_{13}e^{-i\delta_1}s_{24}e^{-i\delta_2} + c_{13}s_{23}c_{24} & c_{14}s_{24}e^{-i\delta_2} \\ U_{\tau 1} & U_{\tau 2} & -s_{14}c_{24}s_{34}s_{13}e^{-i\delta_1} - c_{13}s_{23}s_{34}s_{24}e^{i\delta_2} + c_{13}c_{23}c_{34} & c_{14}c_{24}s_{34} \\ U_{s1} & U_{s2} & -s_{14}c_{24}c_{34}s_{13}e^{-i\delta_1} - c_{13}s_{23}c_{34}s_{24}e^{i\delta_2} - c_{13}c_{23}s_{34} & c_{14}c_{24}c_{34} \end{pmatrix} \tag{5.4}$$

Where $s_{ij} = \sin\theta_{ij}$ and $c_{ij} = \cos\theta_{ij}$. Now, using the oscillation probability derived in Chapter 2:

$$\begin{aligned} P_{\nu_\alpha \to \nu_\beta} &= \delta_{\alpha\beta} - 4\sum_{i>j} \Re\left[U^*_{\alpha i}U_{\beta i}U_{\alpha j}U^*_{\beta j}\right]\sin^2\frac{\Delta m^2_{ij}L}{4E} \\ &\quad +2\sum_{i>j} \Im\left[U^*_{\alpha i}U_{\beta i}U_{\alpha j}U^*_{\beta j}\right]\sin\frac{\Delta m^2_{ij}L}{2E} \end{aligned} \tag{5.5}$$

The probability for $\nu_\mu \to \nu_e$ can be worked out for various different scenarios. In all cases, however, oscillations due to the solar mass squared splitting will be neglected, so we can write:

$$\sum_{i>j} \Re\left[\eta_{ij}\right] \sin^2 \phi_{ij} = \Re\left[\eta_{41}+\eta_{42}\right] \sin^2 \phi_{41} + \Re\left[\eta_{32}+\eta_{31}\right] \sin^2 \phi_{31} + \Re\left[\eta_{43}\right] \sin^2 \phi_{43} \quad (5.6)$$

Where $\phi_{ij} \equiv \frac{\Delta m^2_{ij} L}{4E}$ and $\eta_{ij} \equiv U^*_{\alpha i} U_{\beta i} U_{\alpha j} U^*_{\beta j}$. Now using unitarity relation, for $\alpha \neq \beta$, $\sum_i U_{\alpha i} U^*_{\beta i} = 0$, the following are found:

$$\eta_{41} + \eta_{42} = -|U_{\alpha 4}|^2 |U_{\beta 4}|^2 - U^*_{\alpha 4} U_{\beta 4} U_{\alpha 3} U^*_{\beta 3} \quad (5.7)$$

$$\eta_{32} + \eta_{31} = -|U_{\alpha 3}|^2 |U_{\beta 3}|^2 - U^*_{\alpha 3} U_{\beta 3} U_{\alpha 4} U^*_{\beta 4} \quad (5.8)$$

Putting these back into equation (5.6):

$$\sum_{i>j} \Re\left[\eta_{ij}\right] \sin^2 \phi_{ij} = -|U_{\alpha 4}|^2 |U_{\beta 4}|^2 \sin^2 \phi_{41} - |U_{\alpha 3}|^2 |U_{\beta 3}|^2 \sin^2 \phi_{31} + \Re\left[\eta_{43}\right] \left(\sin^2 \phi_{43} - \sin^2 \phi_{41} - \sin^2 \phi_{31}\right) \quad (5.9)$$

Following the same procedure with the imaginary part and substituting back into equation (5.5):

$$P_{\nu_\alpha \to \nu_{\beta \neq \alpha}} = 4|U_{\alpha 4}|^2 |U_{\beta 4}|^2 \sin^2 \phi_{41} + 4|U_{\alpha 3}|^2 |U_{\beta 3}|^2 \sin^2 \phi_{31} + 4\Re\left[U^*_{\alpha 4} U_{\beta 4} U_{\alpha 3} U^*_{\beta 3}\right] \left(\sin^2 \phi_{41} + \sin^2 \phi_{31} - \sin^2 \phi_{43}\right) + 2\Im\left[U^*_{\alpha 4} U_{\beta 4} U_{\alpha 3} U^*_{\beta 3}\right] \left(\sin 2\phi_{31} - \sin 2\phi_{41} + \sin 2\phi_{43}\right) \quad (5.10)$$

Now some approximations can be made depending on the baseline and value of θ_{13}. The first case to be considered will be the very short (LSND equivalent)

baseline case.

5.2.1 $P(\nu_\mu \to \nu_e)$ for LSND L/E

In this case it is possible to neglect ν_e appearance driven by the atmospheric mass squared splitting, Δm^2_{32}, in addition to those driven by Δm^2_{21}:

$$\begin{aligned} P_{\nu_\mu \to \nu_e} &= 4|U_{\mu 4}|^2 |U_{e4}|^2 \sin^2 \phi_{41} \\ &\quad + 4\Re\left[U^*_{\mu 4} U_{e4} U_{\mu 3} U^*_{e3}\right]\left(\sin^2 \phi_{41} - \sin^2 \phi_{43}\right) \\ &\quad + 2\Im\left[U^*_{\mu 4} U_{e4} U_{\mu 3} U^*_{e3}\right]\left(\sin 2\phi_{43} - \sin 2\phi_{41}\right) \end{aligned} \tag{5.11}$$

Further making the approximation $\Delta m^2_{41} = \Delta m^2_{43}$, which is reasonable since the LSND favoured solutions require a new mass squared splitting at least an order of magnitude greater than Δm^2_{32}:

$$P_{\nu_\mu \to \nu_e} = 4|U_{\mu 4}|^2 |U_{e4}|^2 \sin^2 \phi_{41} \tag{5.12}$$

Now using (5.4):

$$P_{\nu_\mu \to \nu_e} = \sin^2 2\theta_{14} \sin^2 \theta_{24} \sin^2 \phi_{41} \tag{5.13}$$

Now to compare this with the two flavour oscillation parameters in the LSND analysis:

$$\sin^2 2\theta_{\text{LSND}} = \sin^2 2\theta_{14} \sin^2 \theta_{24} \tag{5.14}$$

$$\Delta m^2_{\text{LSND}} = \Delta m^2_{41} \tag{5.15}$$

5.2.2 $P(\nu_\mu \to \nu_e)$ for Long Baseline with $\theta_{13} = 0$

For T2K, it is interesting to consider the case where $\theta_{13} = 0$, but ν_e appearance occurs due to short baseline oscillations. Setting $\theta_{13} = 0$ means that $U_{e3} = 0$ so equation (5.10) immediately becomes:

$$\begin{aligned} P_{\nu_\mu \to \nu_e} &= 4|U_{\mu 4}|^2|U_{e4}|^2 \sin^2 \phi_{41} \\ &= \sin^2 2\theta_{14} \sin^2 \theta_{24} \sin^2 \phi_{41} \\ &= \sin^2 2\theta_{\text{LSND}} \sin^2 \phi_{41} \end{aligned} \tag{5.16}$$

Where it is interesting to note that this is exactly the same equation as governs very short baseline oscillations, without needing to assume $\Delta m^2_{43} = \Delta m^2_{41}$. For T2K, the oscillations are very rapid around the peak energy of the neutrino beam, so a reasonable approximation is also $\sin^2 \phi_{41} = \frac{1}{2}$.

5.2.3 $P(\nu_\mu \to \nu_e)$ for Long Baseline with $\theta_{13} \neq 0$

In the long baseline case where $\theta_{13} \neq 0$, the only assumption that can be made is $\Delta m^2_{41} = \Delta m^2_{43}$:

$$\begin{aligned} P_{\nu_\mu \to \nu_e} &= 4|U_{\mu 4}|^2|U_{e4}|^2 \sin^2 \phi_{41} + 4|U_{\mu 3}|^2|U_{e3}|^2 \sin^2 \phi_{31} \\ &\quad +4\Re\left[U^*_{\mu 4}U_{e4}U_{\mu 3}U^*_{e3}\right] \sin^2 \phi_{31} \\ &\quad +2\Im\left[U^*_{\mu 4}U_{e4}U_{\mu 3}U^*_{e3}\right] \sin 2\phi_{31} \end{aligned} \tag{5.17}$$

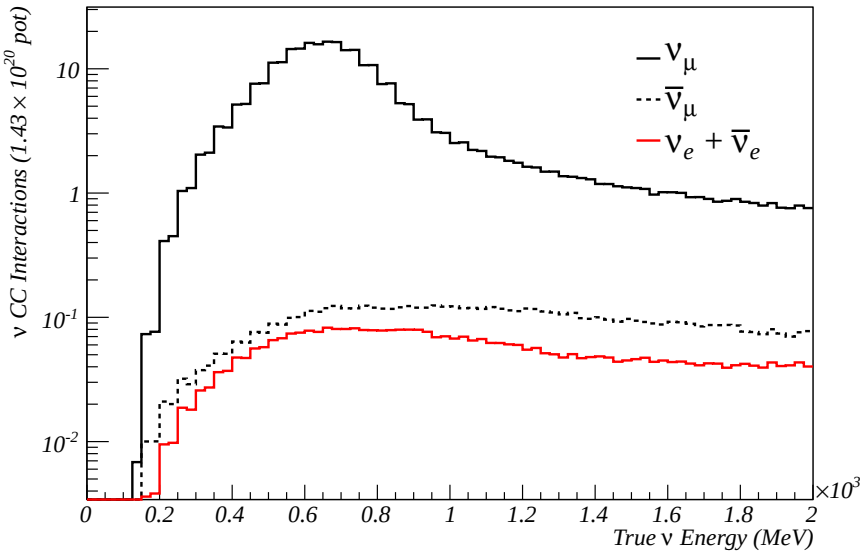


Figure 5.2: Charged current neutrino event rate predictions at the T2K Far Detector, SK, in the absence of any neutrino oscillations, for the Run 1+2 dataset.

5.3 T2K $\nu_\mu \rightarrow \nu_e$ Analysis

The T2K Experiment looks for ν_e appearance in a predominantly ν_μ beam, to constrain the neutrino oscillation parameter θ_{13}. An overview of the T2K experiment is given in Chapter 3. The number and type of neutrino interactions at Super-Kamiokande is predicted using Monte Carlo, which is then re-weighted using the hadron production data from the NA61 hadron production experiment. The total predicted number of charged-current neutrino interactions at SK, for the run 1+2 dataset, in the absence of any neutrino oscillations, from the different neutrino flavours can be seen in Figure 5.2.

This event rate prediction for SK is then weighted by the total charged-current ν_μ interaction data to MC ratio at the ND280, which was measured to be [113]:

$$\frac{N^{\text{data}}_{\nu_\mu}}{N^{\text{MC}}_{\nu_\mu}} = 1.036 \pm 0.028(\text{stat.})^{+0.044}_{-0.037}(\text{det. syst.}) \pm 0.038(\text{phys. syst.}) \quad (5.18)$$

For the Run 1+2 dataset, excluding errors that cancel between the near and far detectors. The following section will focus on the ν_e reconstruction at the T2K far detector, Super-Kamiokande.

5.3.1 Super-Kamiokande ν_e Reconstruction

The reconstruction criteria from the 2011 electron neutrino appearance analysis [113] will be followed here. The first reconstruction criterion is that the reconstructed neutrino vertex be within the fiducial volume (FV) of SK, to remove events that enter the detector from outside. The event is also required to be fully contained in the detector FV, to ensure that the energy reconstruction will not be biased. The total visible energy of the event must be greater than 100 MeV. The event must only have one Čerenkov ring, to select CCQE events, and that ring must be electron-like rather than muon-like. In addition, the event must not have an associated decay electron to further eliminate muon neutrino events. The reconstructed momentum of the neutrino event must be less than 1250 MeV to reduce the background event rate from high energy ν_e in the beam outside the oscillation signal region.

The final cut is to remove a background to the ν_e appearance search: π^0 events. π^0s created in neutral current neutrino interactions decay predominantly $\pi^0 \rightarrow \gamma\gamma$. Whilst a single photon Čerenkov ring is indistinguishable from an electron Čerenkov ring, a pair of photons can have their invariant mass reconstructed, and if this is close to the π^0 rest mass then the pair could be from a π^0 decay. However, sometimes one of the γ rings will be missed by the reconstruction, either because it is emitted in the same direction as the other photon,

or because its Čerenkov ring was not well defined enough to pass the reconstruction algorithm. In order to eliminate such events, in the case where only one ring is found in an event, a second Čerenkov ring is forced to be reconstructed (whether or not one appears to be there) and the invariant mass of this pair of rings is calculated. If the invariant mass of this pair is greater than 105 MeV, the event is rejected as is could be a photon ring from a π^0 decay where the second ring has been missed.

In summary, the cuts used to select ν_e charged-current events in SK are the following:

- Reconstructed vertex in fiducial volume
- Event fully contained in fiducial volume
- Visible energy > 100 MeV
- Only one Čerenkov ring
- Ring is electron-like
- No decay electron
- π^0 mass cut: $m_{\pi^0} < 105$ MeV
- Reconstructed momentum < 1250 MeV

The efficiency for reconstructing and selecting ν_e CC events can be seen, as a function of the true ν_e energy, in Figure 5.3, where the efficiency for ν_e CC selection (all CC interaction modes) is defined as:

$$\text{Efficiency} = \frac{N(\nu_e \text{ CC Events Selected})}{N(\nu_e \text{ CC Events})} \tag{5.19}$$

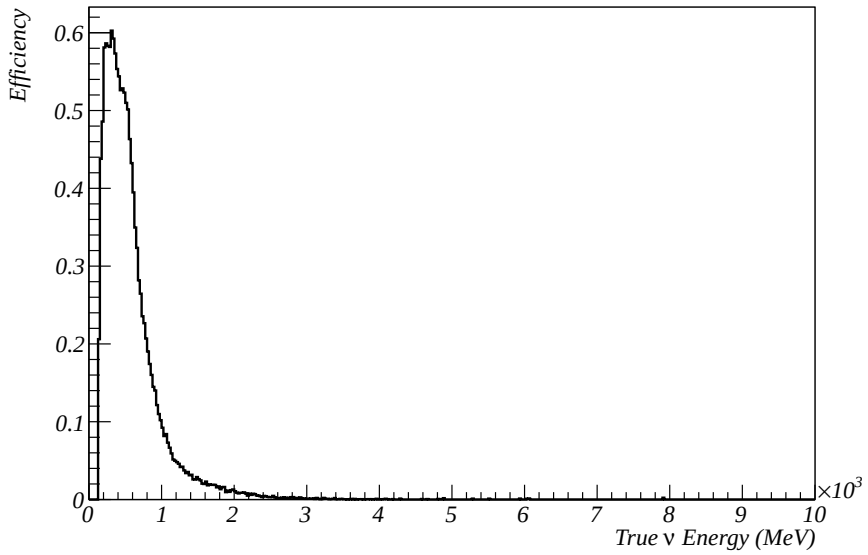


Figure 5.3: Efficiency for CC ν_e reconstruction plus selection, as a function of true neutrino energy, in Super-Kamiokande.

The drop in reconstruction efficiency around 1 GeV is partly due to the reconstructed momentum cut, but is also partly due to the fact that the neutrino interactions at these energies are predominantly non-quasi-elastic. This means that there is likely to be more than one Čerenkov ring reconstructed, so the events are rejected by the cut requiring only one Čerenkov ring in the event.

5.3.2 Energy Reconstruction

Since we hope to select only CCQE events, there should only be one charged lepton in the final state, so conservation of four-momentum gives:

$$p_n - p_V + p_{\nu_e} = p_{e^-} + p_p \tag{5.20}$$

Where V is the average nucleon interaction energy (the average energy transferred to the nucleus during quasi-elastic scattering) and $p_V = (V, \mathbf{0})$. This energy was measured using quasielastic electron scattering experiments [122]. For

oxygen, this energy is 27 MeV (found by interpolation from the values measured for carbon and magnesium). Re-arranging terms and squaring gives:

$$m_p^2 = (p_n - p_V)^2 + m_e^2 + 2(p_n - p_V)p_\nu - 2(p_n - p_V)p_e - 2p_\nu p_e \tag{5.21}$$

Now if the final state electron is emitted at angle θ to the beam direction, and the neutron is at rest:

$$-\frac{1}{2}m_e^2 + \frac{1}{2}\left(m_p^2 - (m_n - V)^2\right) = (m_n - V)E_\nu - (m_n - V)E_e - E_\nu E_e + E_\nu |\mathbf{p}_e| \cos\theta \tag{5.22}$$

Re-arranging to solve for E_ν:

$$E_\nu = \frac{(m_n - V)E_e - \frac{1}{2}m_e^2 + \frac{1}{2}\left(m_p^2 - m_n^2\right) - \frac{1}{2}V^2 + m_n V}{m_n - V - E_e + |\mathbf{p}_e| \cos\theta} \tag{5.23}$$

The correct reconstruction of the neutrino energy depends on whether or not the interaction was actually CCQE. Using the Monte Carlo ν_e events, the relationship between the true and reconstructed energy for CCQE and CC non-QE ν_e events that passed the reconstruction can be seen in Figure 5.4.

5.3.3 Total Backgrounds

There are three classes of background to ν_e appearance: intrinsic ν_e and $\overline{\nu}_e$ in the beam, beam ν_μ and $\overline{\nu}_\mu$ CC events mis-identified as ν_e, and NC events mis-identified as ν_e. After applying the ν_e selection, the total number of background events expected for the Run 1+2 data in the absence of any neutrino oscillations is 1.4 events. These background events can be seen in Figure 5.5.

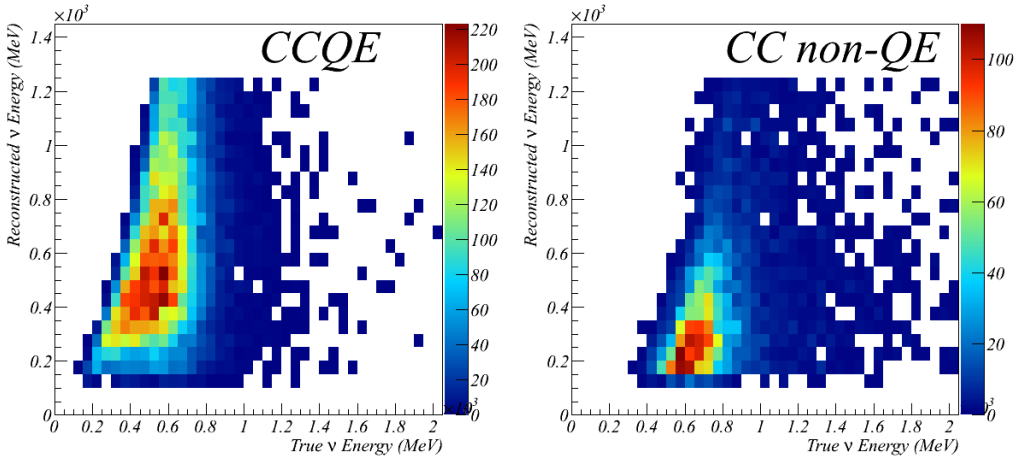


Figure 5.4: Relationship between true and reconstructed neutrino energy for ν_e events passing the selection. The left hand plot shows true CCQE interactions, whereas the right hand plot shows CC non-QE interactions.

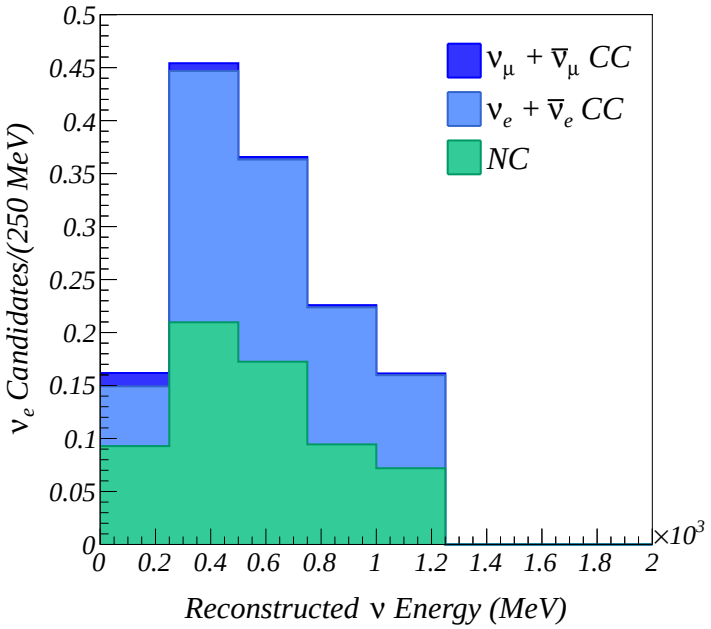


Figure 5.5: Total backgrounds for Run 1+2 $\nu_\mu \rightarrow \nu_e$ search. With no oscillations, 1.4 ν_e candidates are expected, of which 0.6 are NC events, 0.8 are intrinsic ν_e and $\overline{\nu}_e$ in the beam, and 0.03 are mis-identified beam ν_μ and $\overline{\nu}_\mu$ CC events.

5.4 Implementation of 3+1 Neutrino Oscillations

In order to constrain the MiniBooNE short baseline neutrino oscillation parameter space, it is necessary to see what such signals would look like for T2K. Non-standard neutrino oscillations are implemented using a modified version of the General Long Baseline Experiment Simulator (GLoBES) [118, 119]. This is necessary when considering long-baseline ν_e appearance since there is a small probability for $\nu_\mu \rightarrow \nu_e$ from the solar mass squared splitting, and oscillations can cancel in the case where both θ_{13} and θ_{24} are non-zero. In addition there are additional matter effects to consider when oscillations occur between active and sterile neutrino flavours.

5.4.1 Matter Effects between Active and Sterile Neutrinos

As described in Section 2.3.2, any two flavours of neutrino that experience different coherent forward scattering potentials in matter can undergo resonant oscillations in matter at certain energies and matter densities. This means that it is, in principle, possible for a sterile neutrino, which has no scattering potential with matter, to undergo resonant oscillations with any active neutrino flavour since when all active neutrinos travel through matter they experience a potential from coherent neutral current forward scattering given by:

$$V_m^{NC} = \mp \frac{G_F n_n}{\sqrt{2}} \tag{5.24}$$

Where n_n is the number density of neutrons in the matter, and the contributions from the electrons and protons, which are equal and opposite, have cancelled as ordinary matter is electrically neutral. The negative sign is for neutrinos and the positive sign for antineutrinos. This means matter effects must be put into the simulation of sterile neutrino propagation when considering long-baseline

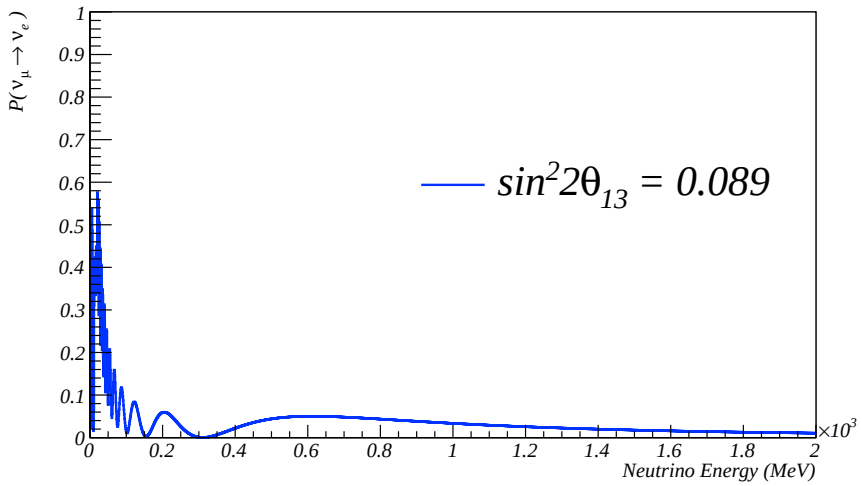


Figure 5.6: $P(\nu_\mu \to \nu_e)$ for Super-K with Daya Bay best fit parameter ($\sin^2 2\theta_{13} = 0.089$) and no short baseline neutrino oscillations.

experiments.

5.5 Oscillation Probabilities for Different $\Delta m^2_{\mathbf{LSND}}$ and $\sin^2 2\theta_{\mathbf{LSND}}$

In the standard neutrino oscillation picture, neutrino oscillations driven largely by θ_{13}, with a small solar neutrino oscillation component, lead to ν_e appearance at SK. The oscillations from a three flavour model including matter effects can be seen in Figure 5.6, where the oscillation parameters used are: $\sin^2 2\theta_{12} = 0.8704$, $\sin^2 2\theta_{13} = 0.089$, $\sin^2 2\theta_{23} = 1.0$, $|\Delta m^2_{21}| = 7.6 \times 10^{-5}\text{eV}^2$, $|\Delta m^2_{32}| = 2.4 \times 10^{-3}\text{eV}^2$ and $\delta = 0.0$. The normal neutrino mass hierarchy $m_3 > m_2, m_1$ is assumed and the matter density between Tokai and Kamioka is taken to be $2.7\,\text{gcm}^{-3}$ [123].

Now, moving to a 3+1 neutrino model, oscillations can also occur $\nu_\mu \to \nu_e$ over a short baseline if θ_{14} and θ_{24} are non-zero. The oscillation probabilities after 295 km are shown for the various MiniBooNE best fit points from [120] in

Figures 5.7 and 5.8. For all of these oscillation probabilities θ_{13} is assumed to be zero. Also shown are the approximations to the oscillation probabilities in the case where we can neglect solar neutrino oscillations and matter effects. Due to the high values of the new mass squared splitting, the oscillations are very rapid in energy by the time the neutrinos have travelled to SK, so $P(\nu_\mu \to \nu_e) \sim \frac{1}{2}\sin^2 2\theta_{\text{LSND}}$.

Interestingly, changing the value of $\sin^2 2\theta_{13}$ from zero to the Daya Bay best fit value has very little effect on the ν_e appearance probability at Super-K for the MiniBooNE best fit neutrino plus antineutrino oscillation scenario. An example of the slight modulation can be seen in Figure 5.9. This is not always true however, if $\theta_{14} = 0$ and $\theta_{24} \neq 0$, changing the value of θ_{13} can have a large effect on the oscillation probability. For the remainder of this chapter it will be assumed that $\sin^2 2\theta_{13} = 0.089$.

The value of the third sterile neutrino mixing angle, θ_{34}, has no effect on the appearance probability $P(\nu_\mu \to \nu_e)$, as can be seen from its absence in the first two rows of Equation 5.4. In principle the values of the $\mathcal{CP}$-violating phases δ_1 and δ_2 can affect the ν_e appearance probability, but in practice T2K is not sensitive to these parameters. This was established by looking for a change in the expected number of ν_e candidates when δ_1 and δ_2 were changed from 0 to $\frac{\pi}{2}$.

5.5.1 Degeneracy between θ_{14} and θ_{24}

A slight complication arises when trying to calculate the number of expected ν_e candidates at SK (N_{exp}) at different values of the short baseline oscillation parameter, θ_{LSND}, since $\sin^2 2\theta_{\text{LSND}}$ is a function of the two oscillation parameters θ_{14} and θ_{24} as in Equation (5.13):

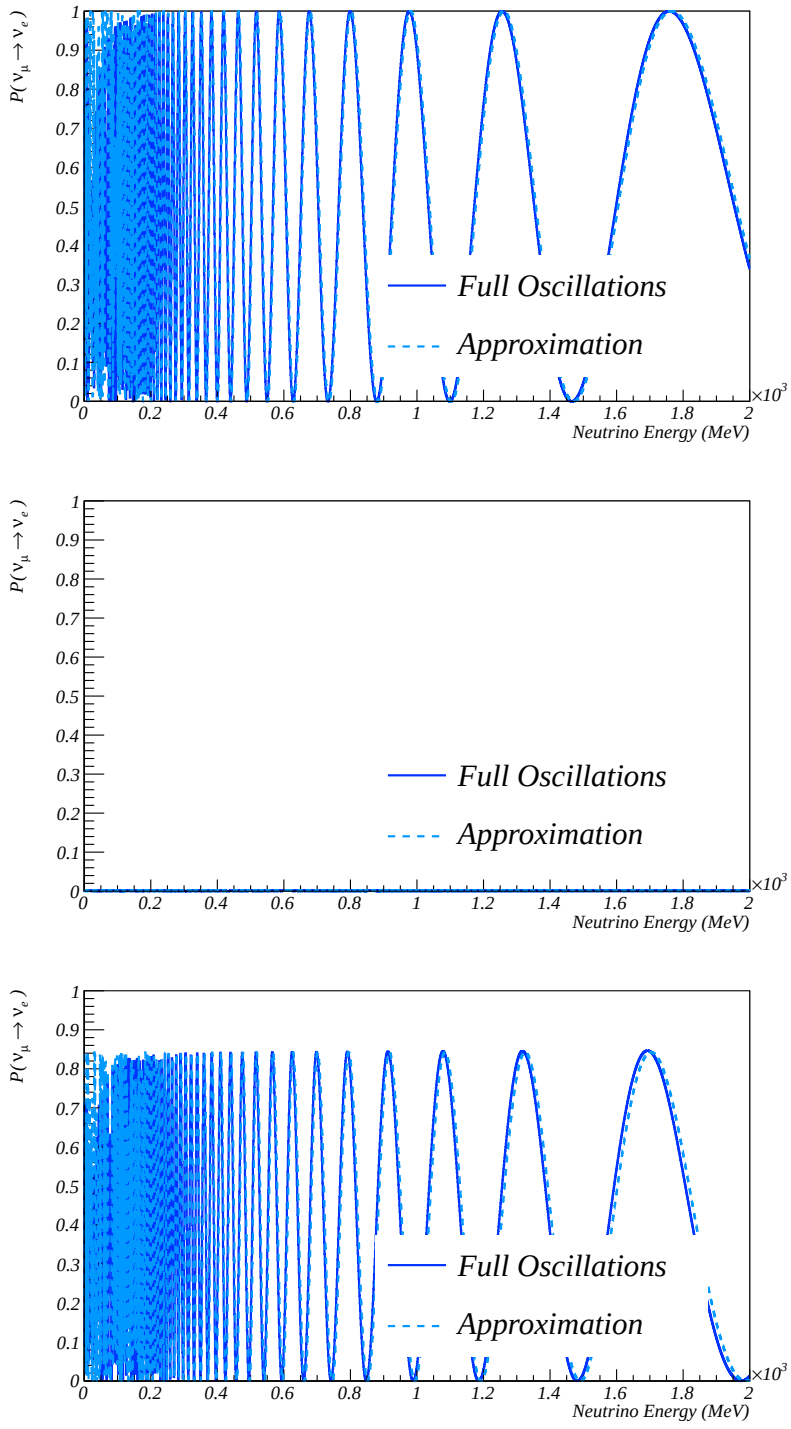


Figure 5.7: $P(\nu_\mu \to \nu_e)$ for Super-K with the three different MiniBooNE best fit points from [120]. Top is the best fit to both neutrino and antineutrino data: (Δm^2,$\sin^2 2\theta$) = ($0.037\,\mathrm{eV}^2$,1.00), center is the best fit to neutrino data ($3.14\,\mathrm{eV}^2$, 0.002) and bottom is the best fit to antineutrino data ($0.05\,\mathrm{eV}^2$, 0.842). On all plots the full 3+1+matter effects solution is shown in addition to the solution neglecting solar neutrino oscillations and matter effects.

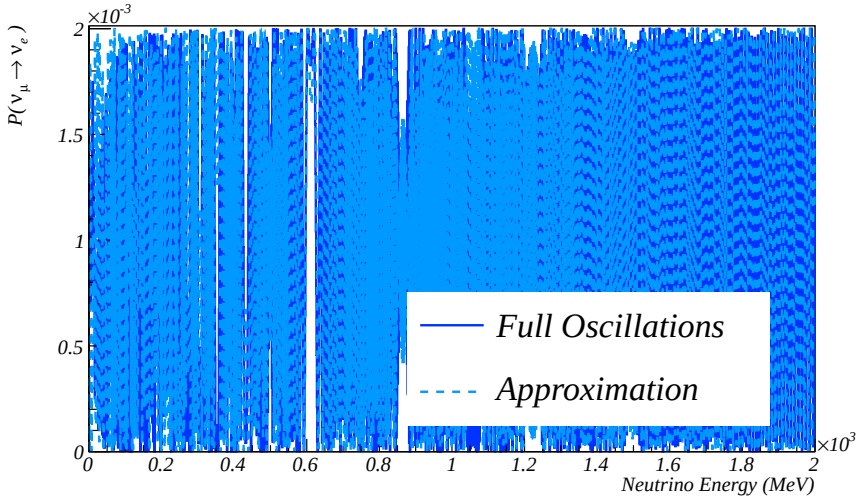


Figure 5.8: $P(\nu_\mu \rightarrow \nu_e)$ for Super-K with best fit to MiniBooNE neutrino data from [120]. This plot is a zoomed version of the central plot from Figure 5.7.

$$\sin^2 2\theta_{\text{LSND}} = \sin^2 2\theta_{14} \sin^2 \theta_{24} \tag{5.25}$$

This means that, at each point in $(\Delta m^2_{\text{LSND}}, \sin^2 2\theta_{\text{LSND}})$ space, there are a range of possible values of N_{exp}. The parameter ranges that must be considered at each point of $(\Delta m^2_{\text{LSND}}, \sin^2 2\theta_{\text{LSND}})$ space are:

$$\sin^2 2\theta_{\text{LSND}} < \sin^2 \theta_{24} \leq 1 \tag{5.26}$$

$$\sin^2 2\theta_{14} = \frac{\sin^2 2\theta_{\text{LSND}}}{\sin^2 \theta_{24}} \tag{5.27}$$

These possible values were looped over at each point in the parameter space and the maximum and minimum values of N_{exp} were recorded. This is necessary for making confidence contours: if the data are compatible with some range of N_{exp}, points of the parameter space that have a maximum predicted N_{exp} that is less than the smallest value compatible with the data, and points that have a minimum predicted N_{exp} that is greater than the maximum value

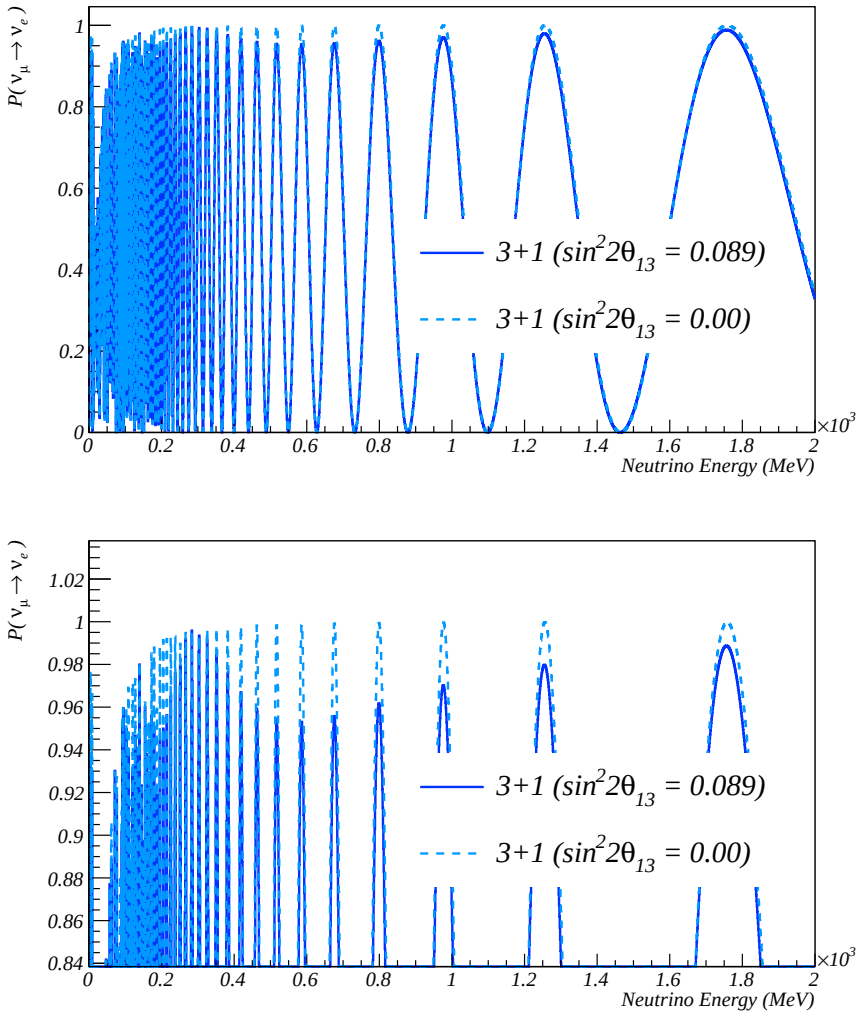


Figure 5.9: $P(\nu_\mu \rightarrow \nu_e)$ with 3+1 neutrinos, with $\sin^2 2\theta_{13} = 0., 0.089$ and the MiniBooNE best fit parameters to the neutrino and antineutrino dataset from [120]. The bottom plot is a zoomed version around the slight modulation caused by θ_{13}.

compatible with the data, will be excluded. This is discussed in more detail in Section 5.6.

5.5.2 Constraint from $P(\nu_\mu \rightarrow \nu_\mu)$ at the ND280

When considering points in $(\Delta m^2_{\text{LSND}}, \sin^2 2\theta_{\text{LSND}})$ space, it is also necessary to re-calculate the expected ND280 ν_μ event rate, since this is used to make the ν_e event rate prediction for SK, as can be seen in Equation (5.28). Any reduction in the ND280 ν_μ event rate due to short baseline oscillations will change $N^{\text{MC}}_{\text{ND280}}$.

$$N^{\text{exp}}_{\text{SK}} = \frac{N^{\text{data}}_{\text{ND280}}}{N^{\text{MC}}_{\text{ND280}}} N^{\text{MC}}_{\text{SK}} \tag{5.28}$$

5.6 Excluding models in terms of $N_{\mathbf{exp}}$

The T2K ν_e appearance analysis in [113] counts the number of ν_e candidates, according to the selection criterion described in Section 5.3.1 of this chapter. It uses the Feldman-Cousins technique to separate the parameter space (θ_{13}, δ) into regions allowed at different confidence levels, by generating toy experiments based on N_{exp} and the error on N_{exp} at each point in the parameter space. The Feldman-Cousins technique and the T2K appearance analysis are discussed in detail in Chapter 7 of this thesis. Since the analysis only uses one bin for the ν_e candidate events, the allowed regions of parameter space can be re-interpreted as being allowed values of N_{exp}.

To interpret this in terms of neutrino oscillations including sterile neutrinos, the confidence regions in terms of N_{exp} can then be used to exclude any models making incompatible predictions for N_{exp}. This is only possible, however, if the systematic errors are the same for both types of signal, and this will be discussed in Section 5.6.1.

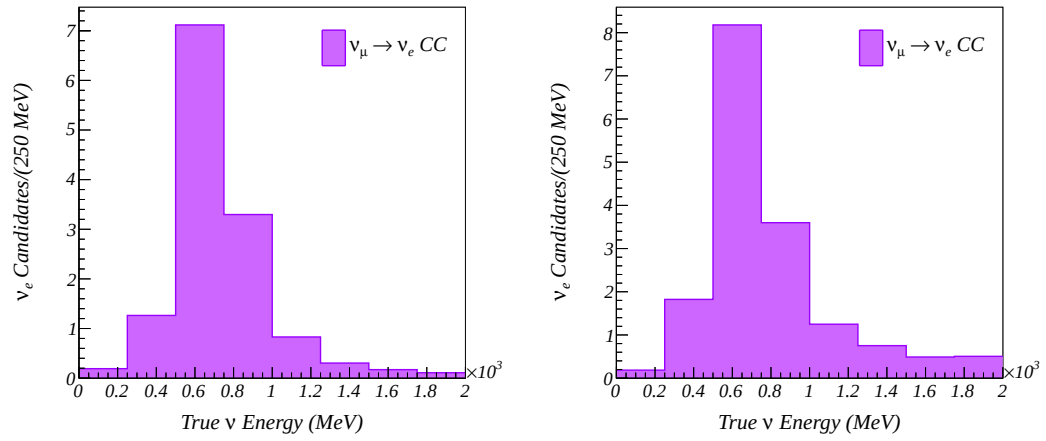


Figure 5.10: The left hand plot shows the number of expected ν_e events for $\sin^2 2\theta_{13} = 0.089$, the Daya Bay best fit point. The right hand point shows the signal from short baseline oscillations $\nu_\mu \rightarrow \nu_e$ for $\Delta m^2_{\text{LSND}} = 0.1\,\text{eV}^2$ and $\sin^2 2\theta_{\text{LSND}} = 0.1$. The signal here is in true neutrino energy, and the signal has not yet been multiplied by the efficiency.

5.6.1 Signal Shapes and Systematic Errors

In order to work out whether the systematic errors from [113] can be used for signals caused by short baseline oscillations, it is necessary to know the energy dependence of such signals. Figure 5.10 shows signals driven, on the left hand side, by $\sin^2 2\theta_{13} = 0.089$, and on the right hand side by $\Delta m^2_{41} = 0.1$, $\sin^2 2\theta_{41} = 0.1$, $\theta_{24} = \frac{\pi}{2}$ and $\theta_{13} = 0$. The signals are shown in true neutrino energy, and the signals have not yet been multiplied by the efficiency histogram. For the short baseline oscillation case, more high energy events can be seen. This is because the ν_μ beam has a high energy tail, some of whose events are oscillated since the oscillation probability is very flat. For the θ_{13} driven case, these high energy events are not seen to such a large extent since the oscillation probability peaks around 600 MeV and then drops off.

Now, multiplying by the ν_e reconstruction plus selection efficiency, which is a function of neutrino energy as was seen in Figure 5.3, the signals, still in true

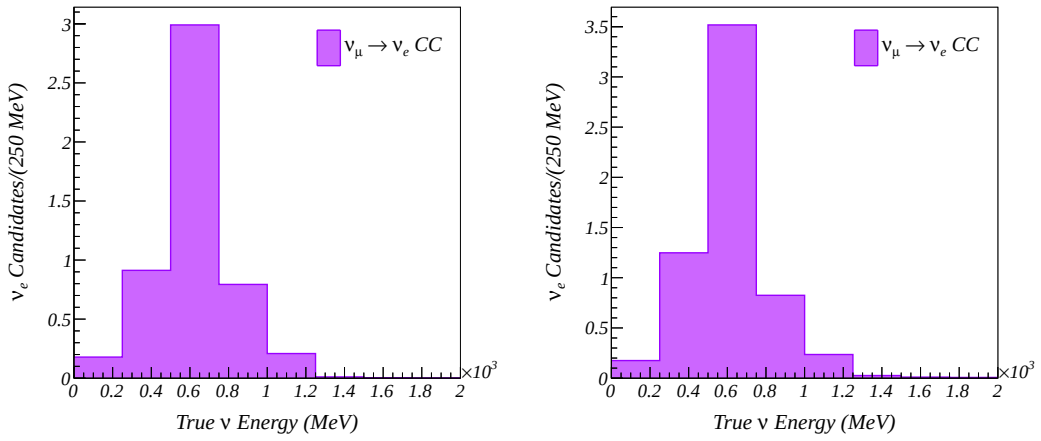


Figure 5.11: The left hand plot shows the number of expected ν_e events for $\sin^2 2\theta_{13} = 0.089$, the Daya Bay best fit point. The right hand point shows the signal from short baseline oscillations $\nu_\mu \to \nu_e$ for $\Delta m^2_{\text{LSND}} = 0.1\,\text{eV}^2$ and $\sin^2 2\theta_{\text{LSND}} = 0.1$. The signal here is in true neutrino energy, after multiplication by the efficiency.

neutrino energy, can be seen in Figure 5.11. The difference in the shape of the signal is negligible since the high energy events from the short baseline oscillation driven case have been removed. This is largely due to the fact that higher energy CC ν_e interactions are more likely to have other particles associated with them, and therefore be removed by the multi-ring cut, and also partly due to the cut in reconstructed neutrino energy. This means that, to first order, we can apply the systematic errors from the standard ν_e appearance analysis in [113] to signals of this kind [1].

For illustration, Figure 5.12 shows the result of converting the true neutrino energy to reconstructed neutrino energy. The conversion is made using the histograms in Figure 5.4, and is applied separately for CCQE and CC non-QE ν_e interactions. This conversion is actually not made in the final analysis as it is a counting experiment.

[1] Ideally, of course, the systematic errors would be completely re-evaluated for this analysis. However, the systematic error calculation was the work of many people so re-evaluation of it is beyond the scope of this thesis.

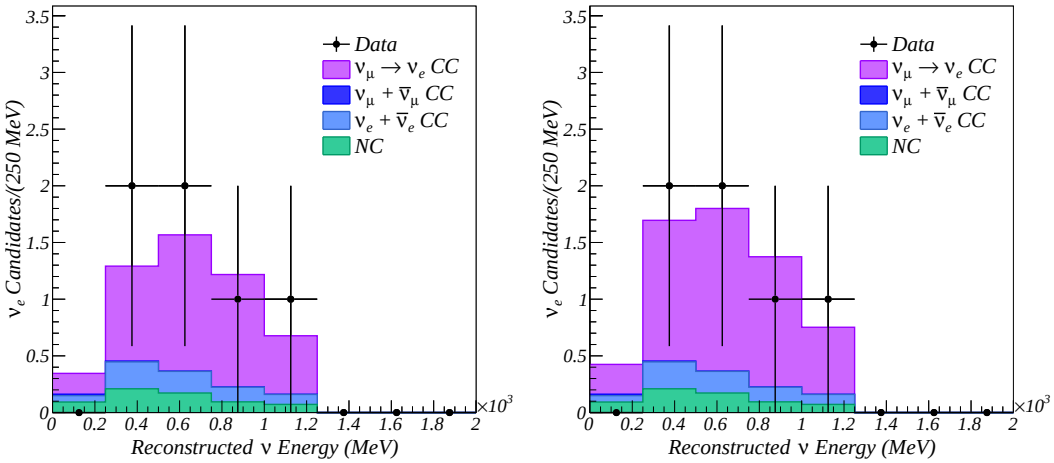


Figure 5.12: The left hand plot shows the number of expected ν_e events for $\sin^2 2\theta_{13} = 0.089$, the Daya Bay best fit point. The right hand point shows the signal from short baseline oscillations $\nu_\mu \to \nu_e$ for $\Delta m^2_{\text{LSND}} = 0.1\,\text{eV}^2$ and $\sin^2 2\theta_{\text{LSND}} = 0.1$.

5.7 Results

The first step towards creating allowed regions of the parameter space at confidence levels is to convert the result from [113] into allowed regions of N_{exp} instead of $\sin^2 2\theta_{13}$ at $\delta = 0$. The difference between the Δ log-likelihood for the T2K data, 6 ν_e candidates, and the critical Δ log-likelihood for the given confidence level, as a function of N_{exp} can be seen in Figure 5.13. The allowed values of N_{exp} for each confidence level are those values for which $\Delta \log \mathcal{L} - \Delta \log \mathcal{L}_{\text{crit}}$ is less than or equal to zero. The Feldman-Cousins technique is described in detail in Chapter 7.

Now to create the confidence level contours the values of N_{exp} at each point in the parameter space under consideration need to be compared to the edge values of N_{exp} for the different confidence level regions. The maximum and minimum values of N_{exp} for each point in the parameter space are shown in Figure 5.14. The maximum number of events allowed by the data must be less than the minimum number of events predicted by the values of $(\Delta m^2_{\text{LSND}}, \sin^2 2\theta_{\text{LSND}})$

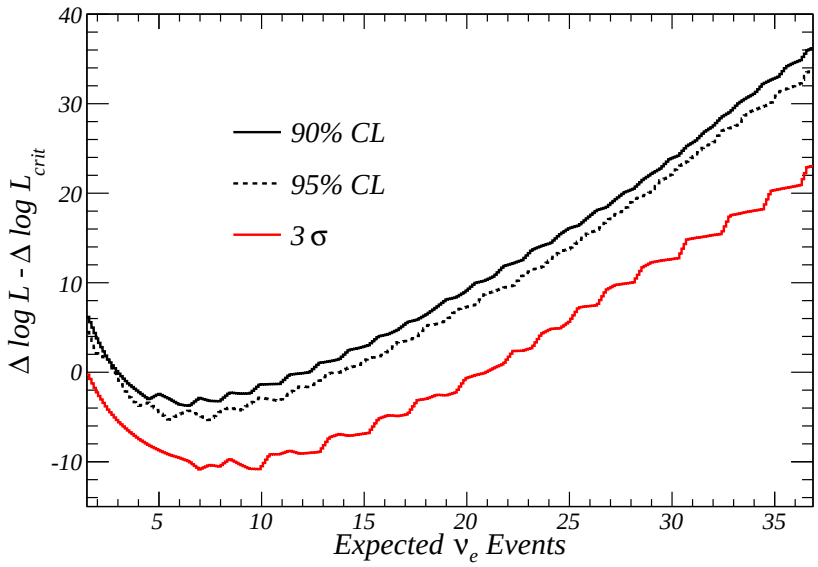


Figure 5.13: Values of $\Delta \log \mathcal{L} - \Delta \log \mathcal{L}_{\text{crit}}$ in terms of expected ν_e candidates at SK. Where the value of $\Delta \log \mathcal{L} - \Delta \log \mathcal{L}_{\text{crit}}$ is less than or equal to zero, models predicting the value of N_{exp} are allowed by the T2K data.

to exclude a point in the parameter space. The minimum number of events allowed by the data is always greater than the maximum model prediction at each value of the parameter space shown for all the confidence levels here.

The region of the $(\sin^2 2\theta_{\text{LSND}}, \Delta m^2_{\text{LSND}})$ parameter space that is excluded by this analysis can be seen in Figure 5.15. The region to the lower right hand side of the contours is excluded at the confidence levels shown.

It is interesting to compare the region disfavoured by this analysis with the MiniBooNE results presented in [120], the allowed parameter regions from which can also be seen in Figure 5.15. Assuming a 3+1 neutrino oscillation model, part of the large mixing angle solution from MiniBooNE, including the global best fit point, can be excluded by this analysis at $3\,\sigma$. After this measurement was made, the ICARUS Collaboration published a similar analysis [125].

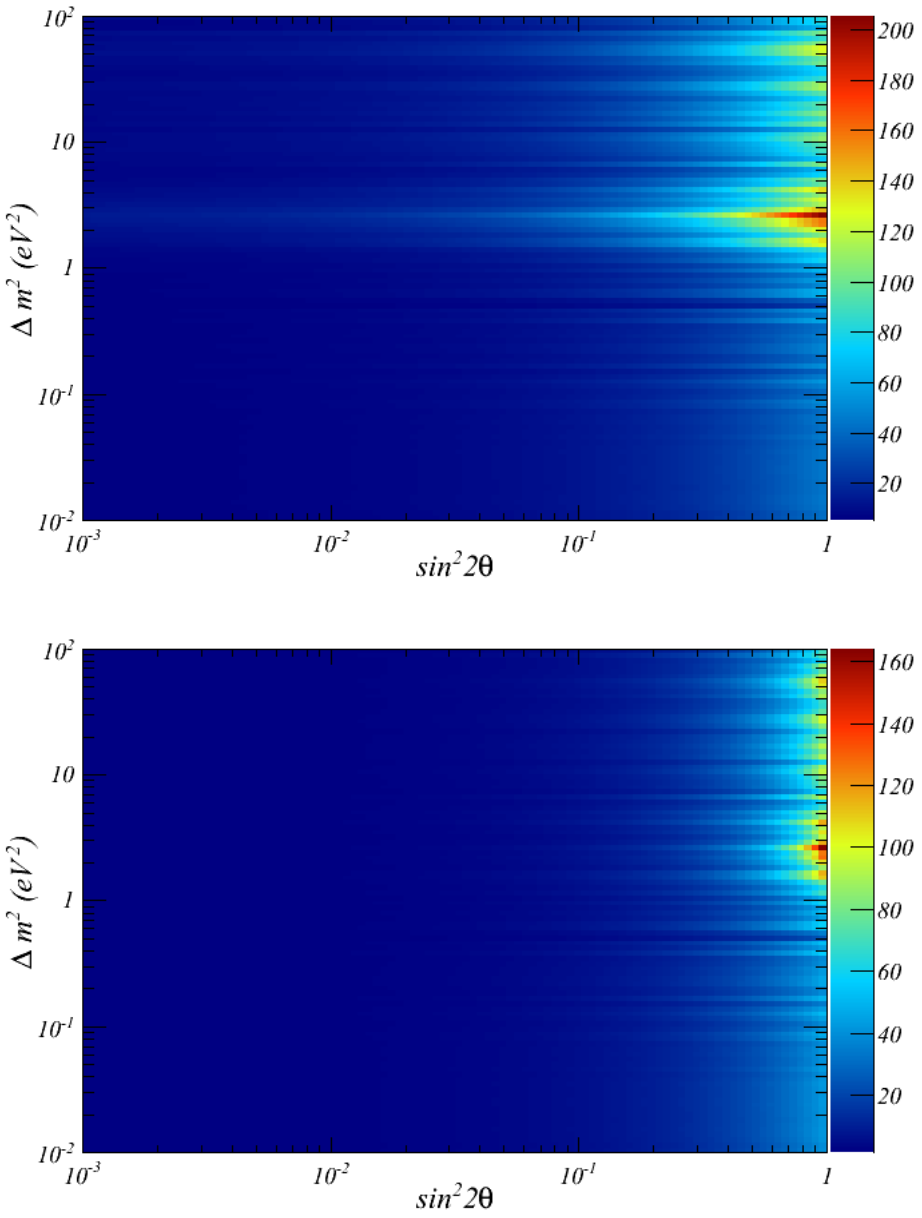


Figure 5.14: Maximum (above) and minimum (below) possible value of expected ν_e candidates at SK for different values of the LSND oscillation parameters. These values were found at each point by varying θ_{14} and θ_{24} such that $\sin^2 2\theta_{14} \sin^2 \theta_{24} = \sin^2 2\theta_{\text{LSND}}$. The minimum number of expected candidates is the number relevant for the upper exclusion contour.

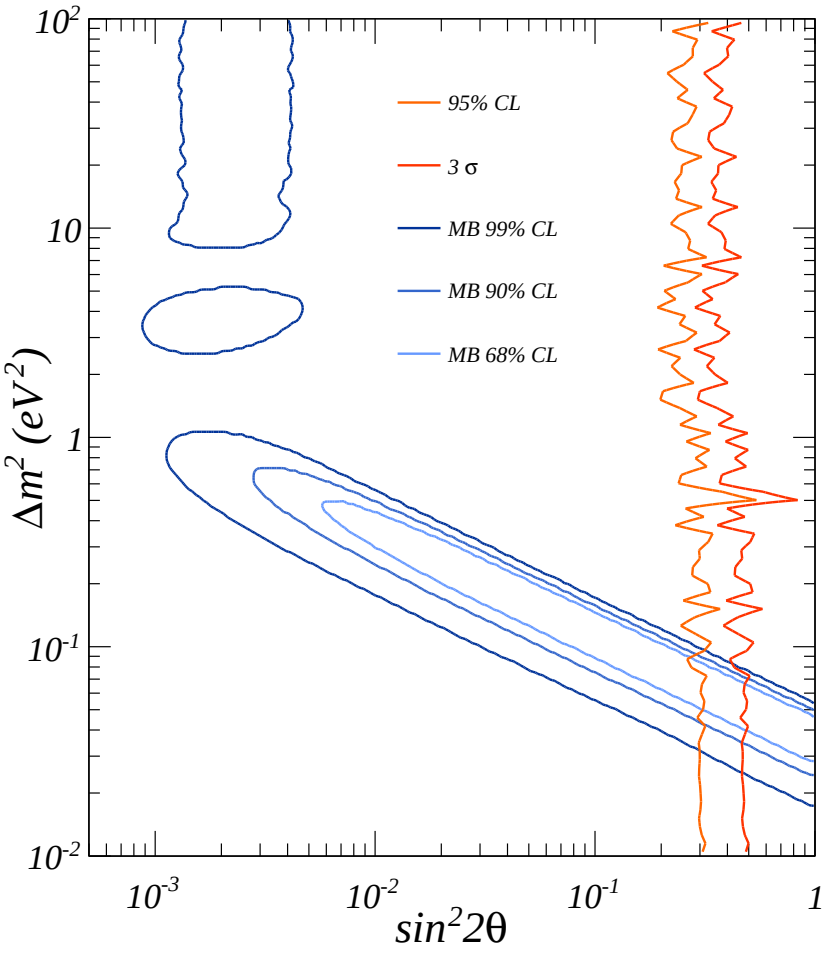


Figure 5.15: T2K confidence limits on LSND oscillation parameter space from $\nu_\mu \rightarrow \nu_e$. The excluded region is to the right of the contours. Contours from the MiniBooNE joint neutrino and antineutrino analysis published in [120] are also shown.

Chapter 6

Near Detector ν_e Appearance from Short Baseline Oscillations

This chapter is concerned with possible signals of short baseline oscillations $\nu_\mu \rightarrow \nu_e$ in the T2K ND280. A 3+1 neutrino scenario will be used as discussed in Chapter 5. Predictions of signals for different values of the short baseline oscillation parameters will be made in Section 6.5. The use of the ND280 Tracker to perform a ν_e selection will be described in Section 6.2, and the results of this selection will be presented in Section 6.7. The future sensitivity of the ND280 to such signals will be discussed in Section 6.8.

6.1 Motivation for $\nu_\mu \rightarrow \nu_e$ Search using the ND280

The ND280 has a very similar L/E to MiniBooNE and uses a very similar neutrino beam. As was discussed in Chapter 5, the oscillation probabilities for a model with three active plus one sterile neutrino (3+1 model) are directly comparable for MiniBooNE and other experiments with similar L/E, and only governed by Δm^2_{LSND} and $\sin^2 2\theta_{\text{LSND}}$. For this reason it makes sense that the electron-neutrino like event excesses seen by MiniBooNE should be searched

for using the ND280.

Unlike MiniBooNE, however, the ND280 is not a liquid scintillator detector, and has the ability to distinguish between electrons, positrons and photons due to the magnetic field and the spatial resolution of the detector. The analysis presented in this chapter will only look for ν_e appearance, but with more statistics it could also become interesting to develop single photon searches, since the MiniBooNE excesses could equally be single photons from some process that has not yet been fully understood.

In this analysis, only the tracker region of the ND280 (the FGDs, TPCs and surrounding ECals) is used. An electron-neutrino appearance search could also be performed using the PØD, but this will not be considered in this thesis.

6.2 ND280 Tracker ν_e Reconstruction

The event topology that this selection will focus on will be ν_e CCQE interactions in the fiducial volume of one of the two FGDs. This means that a single electron track (possibly accompanied by a proton track) originating in one of the FGDs must be found. The main backgrounds to such a search come from charged current ν_μ interactions, NC interactions in which one or more π^0s are produced, and CC non-QE ν_e interactions. The selection was developed using one quarter of the available Monte Carlo sample, so as not to bias the selection, and aims to maximise efficiency times purity. The full MC sample was used when calculating the final event rates and efficiencies.

Before performing the selection, the reconstructed objects need to be grouped according to which beam spill and bunch they occur in. Within the data and the MC each beam spill corresponds to a single 'event', which will be looped over, but within each event there are 8 different proton bunches [1]. Each event

[1] In Run 1 there were 6 bunches per spill, but the Run 1 data is not used here, see Section 6.3.

is split into the eight 580 ns (480 ns integration plus 100 ns reset) bunches using the time of the reconstructed objects. Each of these bunches is treated as a separate object for the remainder of this selection. In general, these 'events' may contain multiple neutrino interactions. There is rarely more than one FGD fiducial neutrino interaction in an event, but there will frequently be multiple neutrino interactions in other parts of the ND280, especially in the magnet.

The first step in the selection process is to find the highest momentum, negatively charged, track originating from one of the FGD fiducial volumes, that has enough TPC hits (at least 36 in at least one segment) for the TPC reconstruction. A low track momentum cut is also applied ($p > 150\,\text{MeV}$), since the TPC particle identification (PID) relies on the different dE/dx (energy lost per length travelled through the detector) of different particle types. Below 150 MeV the electron and muon dE/dx curves cross, making the TPC PID unreliable at these energies.

The next step is to perform PID on the selected track. After a track has been reconstructed in the TPC (and its momentum calculated from its curvature), the energy deposited is compared to the expected energy deposit at that momentum for each of the five considered particle types: electrons, muons, pions, kaons and protons [121]. This is quantified in the 'pull', δ_E, for different particle types:

$$\delta_E(i) = \frac{\overline{C}_T - C_E(i)}{\sigma_0(i)} \tag{6.1}$$

Where i is the particle hypothesis, $C_E(i)$ is the expected energy loss for the hypothesized particle at the reconstructed momentum of the track, $\overline{C}_T$ is the measured mean energy loss of the track and $\sigma_0(i)$ is the total error defined as:

$$\sigma_0(i) = \sqrt{\sigma_T^2 + (dC_E(i)/dp)^2\sigma_p^2} \tag{6.2}$$

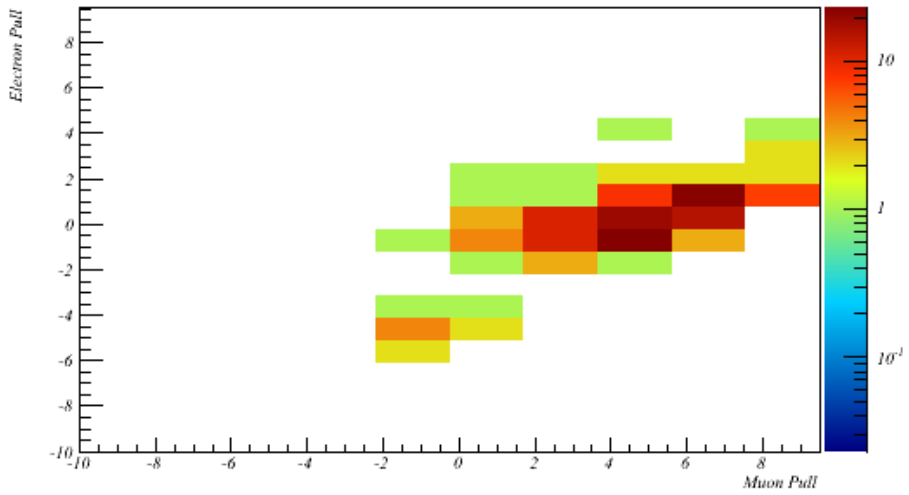


Figure 6.1: TPC electron and muon pulls for the selected track of true CCQE ν_e Monte Carlo events.

Where σ_T is the standard deviation of the measured energy loses, C_T, along the track, and σ_p is the standard deviation of the track momentum measurement.

Ideally this selection would use the TPC pulls to select only tracks that are consistent with being from electrons and reject any tracks likely to be from muons. For this reason I define a two dimensional cut on the electron and muon pulls of the selected track. If the selected track is made up of more than one TPC segment (with at least 36 hits) then the longest segment is chosen to perform the PID. Plots of the muon and electron pulls of the selected tracks from truly CCQE ν_e and ν_μ MC events can be seen in Figures 6.1 and 6.2 respectively. Bins were then chosen for the selection to optimise efficiency times purity. The final cut can be seen in Figure 6.3.

In addition to the PID on the highest momentum track, all of the tracks in the event, that have momentum at least 150 MeV and more than 35 TPC hits, must be inconsistent with being muons. Such a track is rejected as being muon-like if it has muon pull less than 2 and electron pull less than -2. Events are also rejected if there is one or more delayed cluster in the ECal, and one or more

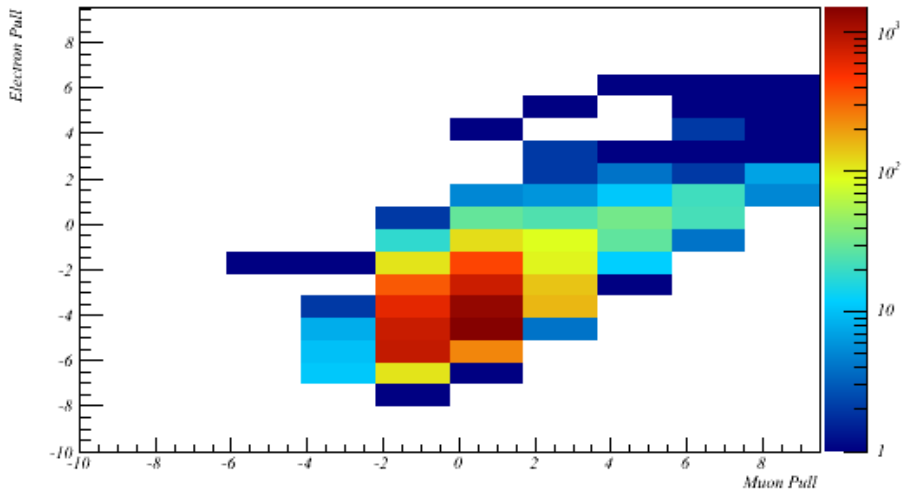


Figure 6.2: TPC electron and muon pulls for the selected track of true CCQE ν_μ Monte Carlo events.

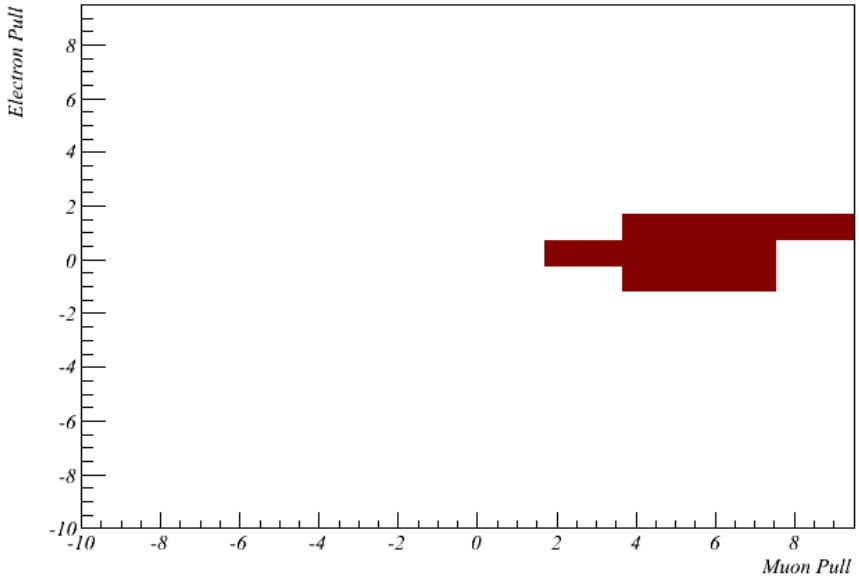


Figure 6.3: TPC PID cut in electron and muon pulls, optimised for efficiency times purity of CCQE ν_e signal. The red region is selected.

muon-like track in the ECal, to reject electrons coming from muon decays.

To prevent events that enter, rather than start within, one of the FGDs being selected, the TPC upstream of the FGD containing the start of the selected track is used as a veto. That means that if the selected track starts in FGD1, the event will be rejected if there are any tracks in TPC1, and if the selected track starts in FGD2, the event will be rejected if there are any tracks in TPC2. In addition to the upstream TPC veto, there is a veto on events containing reconstructed objects in the parts of the Barrel ECal surrounding and upstream of the FGD containing the start of the selected track. Events are rejected if there is a reconstructed ECal object anywhere in an ECal from 1 m upstream of the upstream edge of the FGD fiducial volume in which the event is reconstructed to the downstream edge of the FGD fiducial volume. The veto is not extended downstream since tracks from ν_e CCQE events could enter the ECal after leaving the FGD.

The next step is to remove events where the selected electron is actually part of an e^+e^- pair from a γ decay, *e.g.* following the decay of a π^0. This is done by looping over all the positively charged tracks that start within 20 cm of the start of the selected track, and working out the invariant mass of the pair, which is given by:

$$m_\gamma^2 = 2m_e^2 + 2\left(E_{e^-}E_{e^+} - \mathbf{p}_{e^-}.\mathbf{p}_{e^+}\right) \tag{6.3}$$

Which should be zero, or at least close to zero, depending on the ability of the detector to reconstruct the tracks. If the invariant mass of the parent is found to be less than 60 MeV, the event is rejected. The distributions for the reconstructed γ invariant mass for the signal and background events can be seen in Figure 6.4. Note that a lot of the events will not have candidate pairs and will thus not appear in this plot.

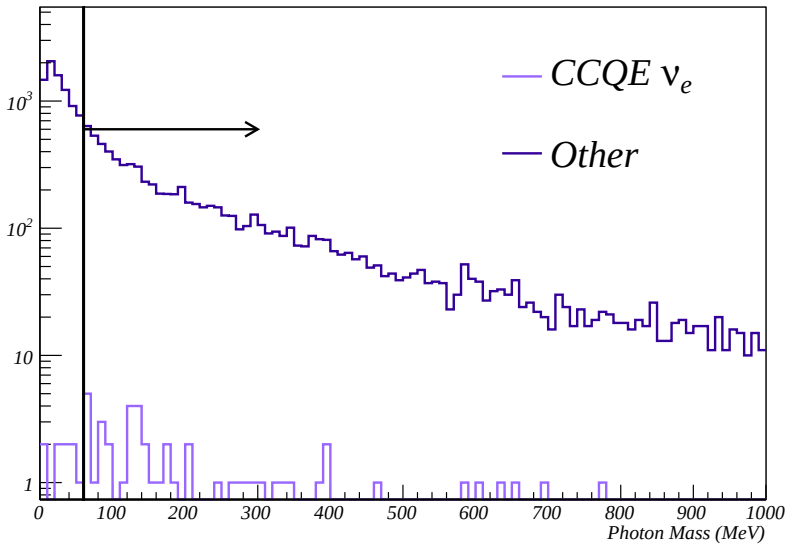


Figure 6.4: Distributions of invariant mass of reconstructed γ mass from true CCQE ν_e events and all other events. If the mass is found to be less than 60 MeV, the event is rejected on the basis that it is consistent with being from a γ interaction. The selected region is marked with an arrow.

The final step relates to the energy reconstruction, which is described in Section 6.2.2. The procedure to reconstruct the energy for an event assumes that the interaction is CCQE, so if the interaction is non-CCQE the energy reconstruction will be wrong and unphysical energies can even be reconstructed. To partly remove this problem, any events with reconstructed energy less than 0 MeV are rejected. In addition, the proportion of signal and background events changes with reconstructed neutrino energy, as can be seen in Figure 6.5. In particular, the background events are heavily peaked around low reconstructed energies. In order to maximise efficiency times purity, the best cut is to select only those events whose reconstructed energy is greater than 400 MeV. This cut will be used, but I will follow MiniBooNE in defining an alternate selection where a low reconstructed energy cut of 200 MeV is also used, as the signal may be peaked in this region. A high reconstructed momentum cut of 2 GeV is also applied to cut out high energy ν_e backgrounds from the beam, since the signals

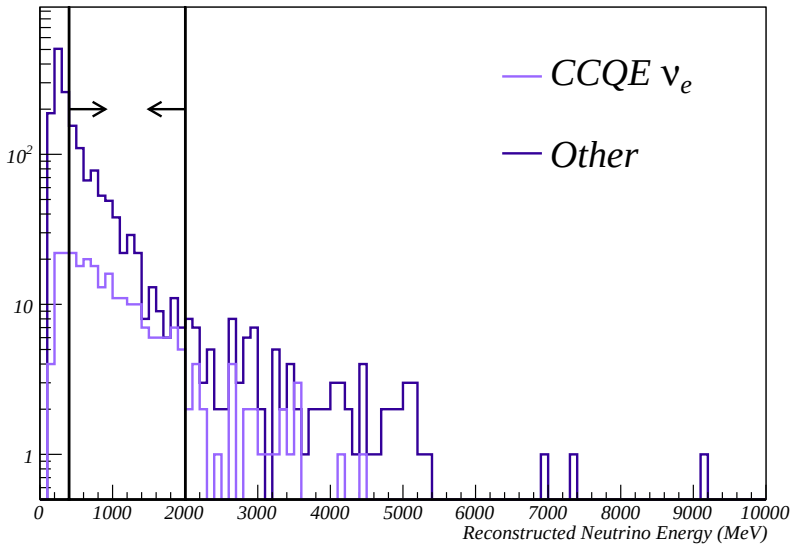


Figure 6.5: Reconstructed energy distributions for the signal CCQE ν_e events and the total background events, after all the other selection cuts have been applied. The events are selected if the reconstructed neutrino energy is greater than 400 MeV and less than 2 GeV. The selected region is marked by the arrows.

from short baseline oscillations are expected to be mostly below these energies.

To summarise, the ν_e reconstruction goes as follows:

1. Preselection
   - Select highest momentum negative track with $>$ 35 TPC hits starting in FGD fiducial volume
   - Track must have momentum $>$ 150 MeV
2. Particle Identification
   - Highest momentum track must have electron and muon pulls consistent with being an electron
   - All well reconstructed tracks must have dE/dx inconsistent with the muon hypothesis
   - No delayed clusters in the ECal

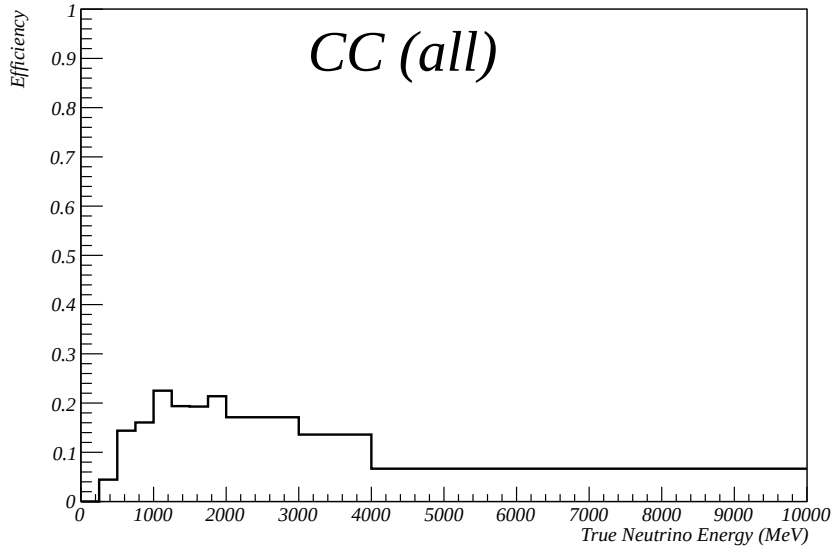


Figure 6.6: Reconstruction and selection efficiency for all CC ν_e interactions in the FGDs as a function of true neutrino energy.

3. Upstream Veto

   - No tracks in TPC immediately upstream of FGD containing vertex
   - No clusters in ECal region surrounding FGD containing vertex

4. γ Rejection, invariant mass of possible pair must be > 60 MeV

5. Momentum cuts

   - $E_{\text{rec}} < 2\,\text{GeV}$ to remove intrinsic ν_e
   - $E_{\text{rec}} > 200\,\text{MeV}$ or $E_{\text{rec}} > 400\,\text{MeV}$ to remove backgrounds, depending on range considered.

6.2.1 Efficiency to Reconstruct and Select Events

The efficiency, after applying all these cuts, can then be calculated for the FGD CC ν_e events. This is done separately for the different interaction modes: CCQE,

CC coherent, CC resonant and CC DIS, due to the different cross section uncertainties associated with the different interaction modes. The efficiency, as a function of true neutrino energy, is defined as:

$$\text{Efficiency}(E) = \frac{N(\nu_e \text{ CC}_i\text{Events Selected})(E)}{N(\nu_e \text{ CC}_i\text{Events})(E)} \tag{6.4}$$

Where CC_i = CCQE, CC coherent, CC resonant or CC DIS, and the denominator is the total number of FGD fiducial CC_i ν_e interactions predicted at that energy by the MC. The separate reconstruction efficiencies for the different interaction modes are used when calculating the expected number of ν_e events. The inclusive reconstruction and selection efficiency, for all CC ν_e interactions, as a function of true neutrino energy, can be seen in Figure 6.6.

6.2.2 Energy Reconstruction

For carbon, the average nucleon interaction energy, V, is 25 MeV [122]. Other than this, the same formula for reconstructing the neutrino energy of CCQE events as in Section 5.3.2 can be used:

$$E_\nu = \frac{(m_n - V)\,E_e - \frac{1}{2}m_e^2 + \frac{1}{2}\left(m_p^2 - m_n^2\right) - \frac{1}{2}V^2 + m_n V}{m_n - V - E_e + |\mathbf{p}_e|\cos\theta} \tag{6.5}$$

The relationship between the true and reconstructed energy for MC CC FGD-fiducial ν_e interactions, split into CCQE and CC non-QE, can be seen in Figure 6.7.

6.3 Dataset

T2K started running in March 2010. The different T2K run periods are summarised in Table 6.1. During Run 1, the T2K ND280 was not completely installed: the Barrel and PØD ECals were not yet in place. Run 2 began in Novem-

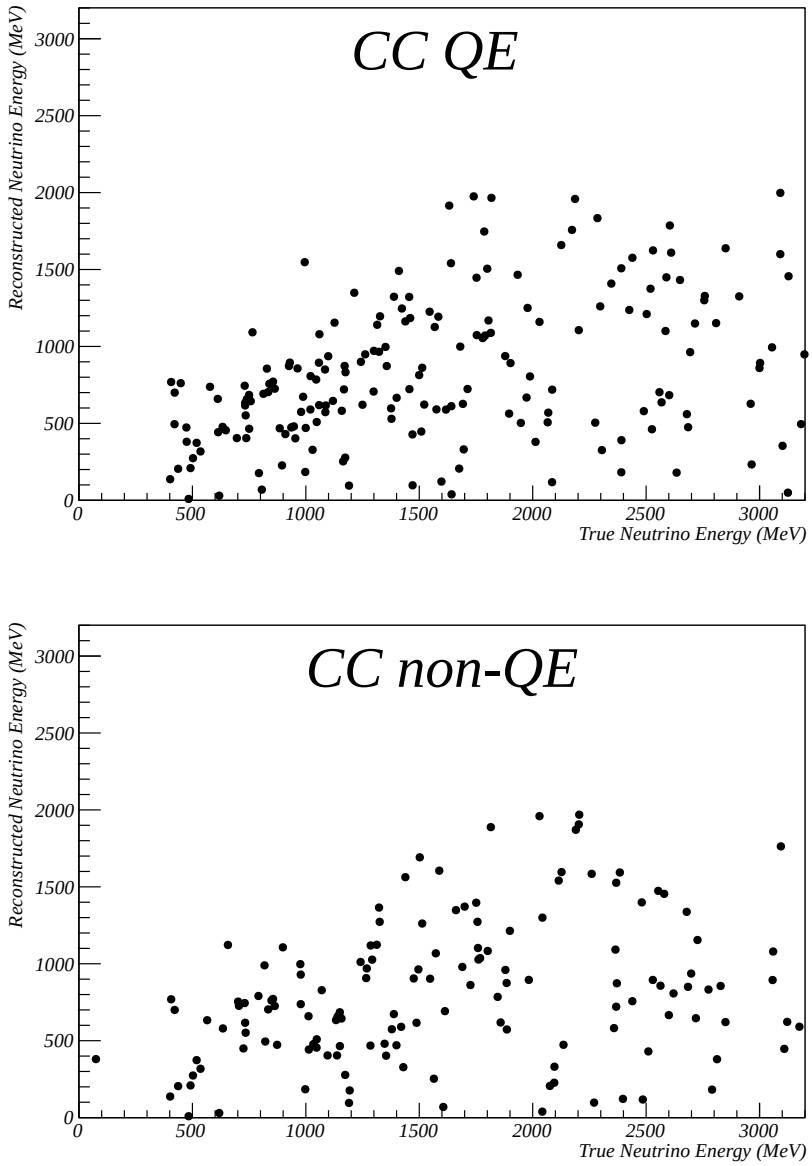


Figure 6.7: Relationship between true and reconstructed neutrino energies for CCQE and CC non-QE ν_e interactions in the FGDs.

ber 2010 and continued until the catastrophic Great East Japan Earthquake on the 11th of March 2011. The T2K beam re-started operation again in early 2012, but problems with the magnetic horn power supplies meant that the initial neutrino beam, for Run 3a, was not focussed, so this data is not included in the physics runs. From late February 2012, the horn power supplies were functioning again. Run 3 is split into two different periods, 3b and 3c, as for the first month of running the horn current, for all three horns, was only 200 kA rather than 250 kA. For Run 3c the horn current was back at the nominal 250 kA.

T2K Run Period	Dates	Protons on Target Recorded
1	19/03/2010 - 26/06/2010	2.8875×10^{19}
2	18/11/2010 - 11/03/2011	7.8862×10^{19}
3b	27/02/2012 - 23/03/2012	2.15555×10^{19}
3c	08/04/2012 - 09/06/2012	1.3547×10^{20}

Table 6.1: Summary of T2K physics run periods and protons on target recorded. Here protons on target recorded means protons on target delivered when all the ND280 subdetectors were fully operational.

For this analysis, only the data from Run 2 will be used. Run 3b and 3c could not be included as the processing of the data was not complete at the time of writing. The data from Run 1 is also not included as the selection would have to be re-developed to cope with the loss of the Barrel ECals, and at present a Monte Carlo sample that would enable this work is not available.

6.4 Selection Results

When applying the selection criteria to the data, in addition to the criteria outlined in Section 6.2, the ND280 is required to be fully operational and the beam is required to be running with 250 kA horn current for all events selected. After scaling the MC to the Run 2 protons on target recorded, the predicted number

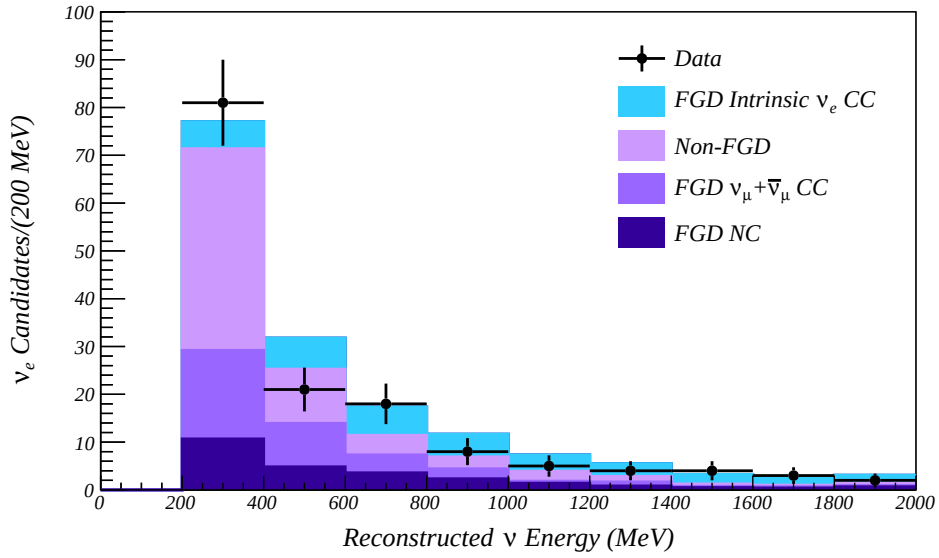


Figure 6.8: Predicted background events at different reconstructed energies and Run 2 selected ν_e CC candidate events.

of events (in the absence of oscillations), for the main search region ($E > 400$ MeV) is 83 ± 22. In the data 65 events are observed. The total error calculation is described in Section 6.6. Of these events, 28 are expected to be ν_e from the beam, 17 are mis-identified ν_μ (largely due to the overlapping dE/dx curves of electrons and muons at low energies) , 15 are NC and 23 are events external to the FGDs (predominantly NC and ν_μ DIS). This translates to a ν_e purity of 34%.

If the extended energy range ($E > 200$ MeV) is used instead, the purity for selecting ν_e events drops to 21%, and 146 events are observed against an expectation of 160 ± 44.5 events. The result of applying the ν_e selection cuts to the Run 2 data, as well as the background predictions, can be seen in Figure 6.8.

It is also interesting to look at the agreement between data and Monte Carlo when one of the cuts is removed. The cuts that have the biggest effect, after the preselection, are the upstream veto and the PID. The effect of removing the upstream veto on the TPC and surrounding ECals can be seen in Figure 6.9. The agreement between data and Monte Carlo is still good when the upstream veto

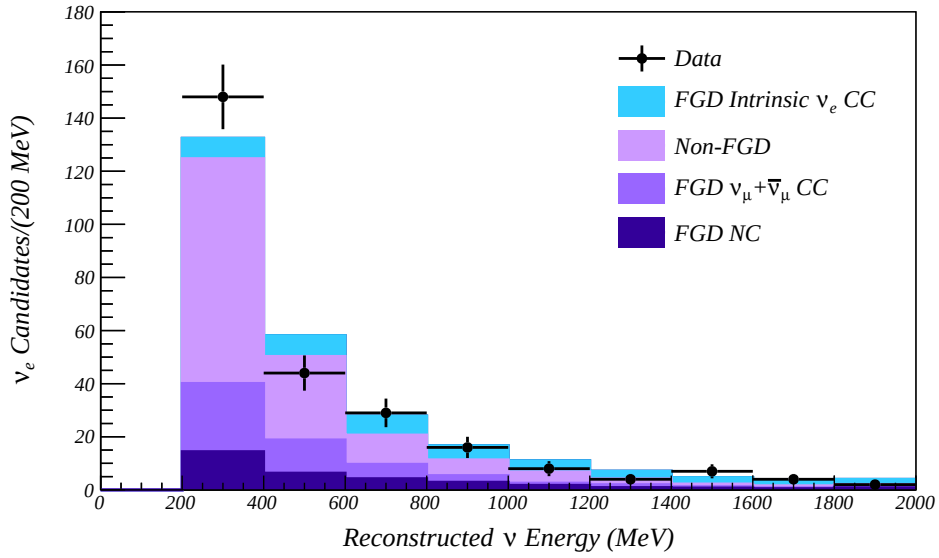


Figure 6.9: Predicted background events at different reconstructed energies and Run 2 selected ν_e CC candidate events, before applying the upstream veto (all other cuts applied).

is removed. The effect of removing all the PID cuts can be seen in Figure 6.10. In the absence of the PID cuts, there is much less agreement between data and MC: there are far more events being selected in the data than the MC. The systematic and statistical errors for this selection are discussed in Section 6.6. The main contributions to the systematic error come from flux, 15.4%, and cross-section, 6-100%, uncertainties. These errors may well account for the differences between the data and MC.

6.5 Oscillation Probabilities for Different $\Delta m^2_{\mathbf{LSND}}$ and $\sin^2 2\theta_{\mathbf{LSND}}$

If there are no short baseline neutrino oscillations from a new value of Δm^2, then the probability for oscillations $\nu_\mu \rightarrow \nu_e$ by the ND280 is negligible.

Introducing a new sterile neutrino as described in Chapter 5, the proba-

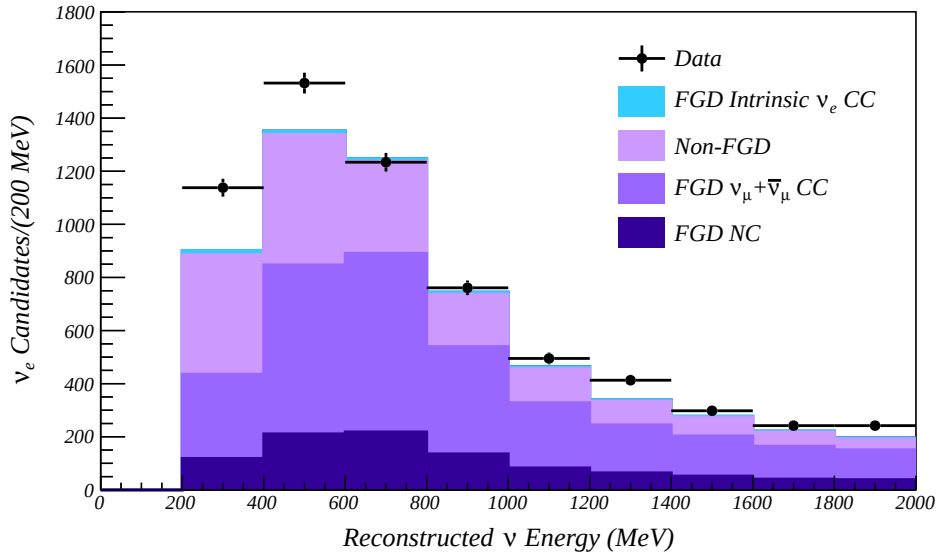


Figure 6.10: Predicted background events at different reconstructed energies and Run 2 selected ν_e CC candidate events, before applying the PID (all other cuts applied).

bilities for electron neutrino appearance at the T2K ND280 become non-zero near to the peak neutrino energy. Oscillation probabilities for the three different MiniBooNE solutions from [120] are shown in Figure 6.11. The top plot is the best fit to both neutrino and antineutrino data: (Δm^2,$\sin^2 2\theta$) = ($0.037\,\mathrm{eV}^2$,1.00), the center plot is the best fit to neutrino data ($3.14\,\mathrm{eV}^2$, 0.002) and bottom plot is the best fit to antineutrino data ($0.05\,\mathrm{eV}^2$, 0.842). In all cases the oscillation probabilities are small, around 0.1% at 600 MeV.

The reconstruction efficiencies for the different CC neutrino interaction modes can then be used, in addition to the probability for $\nu_\mu \rightarrow \nu_e$ oscillations given by:

$$P_{\nu_\mu \rightarrow \nu_e} = \sin^2 2\theta \sin^2 \frac{\Delta m^2 L}{4E} \tag{6.6}$$

To calculate the number of expected ν_e candidates at the ND280, for different values of the short baseline oscillation parameters, from the MC ν_μ CC events.

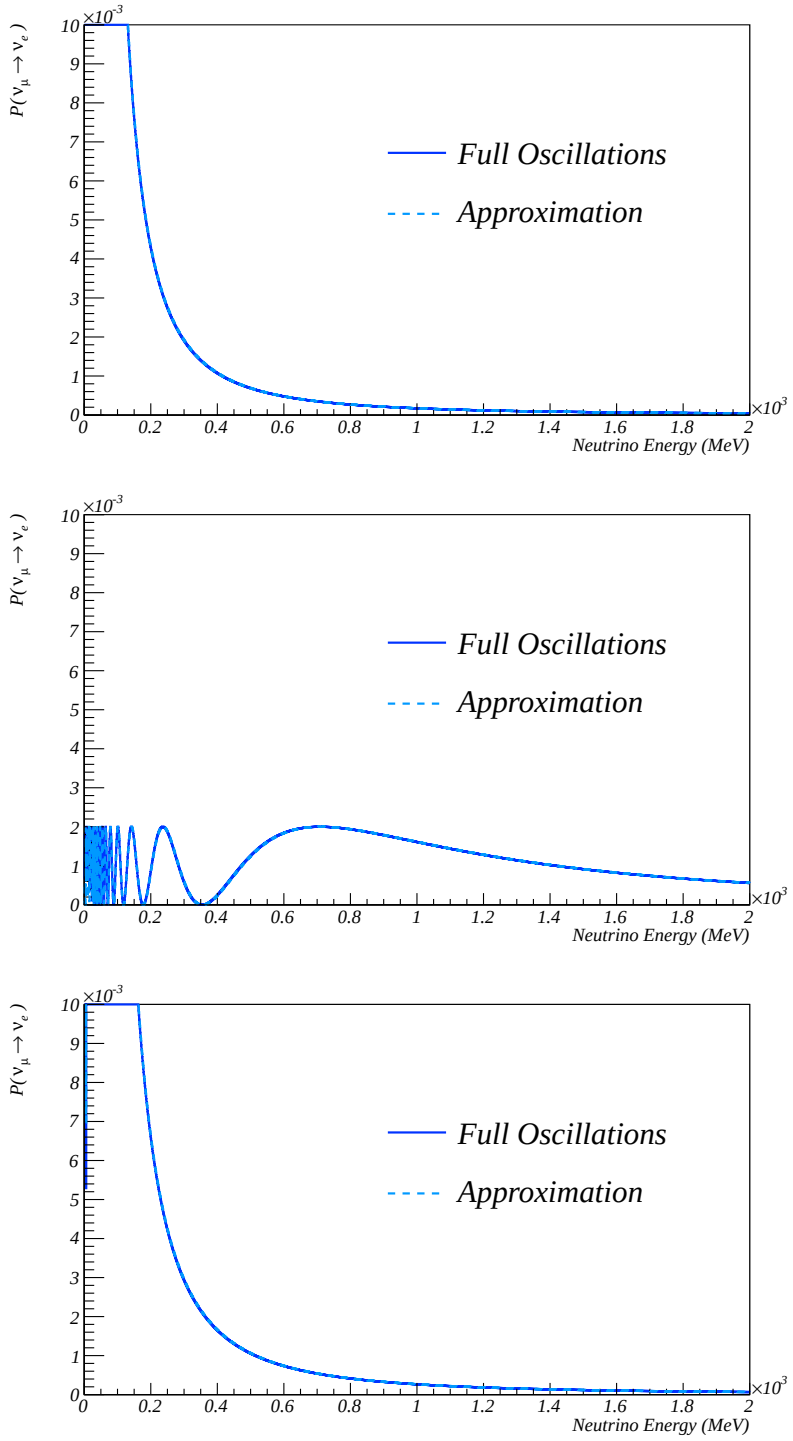


Figure 6.11: $P(\nu_\mu \to \nu_e)$ for ND280 with the three different MiniBooNE best fit points from [120]. The top plot is the best fit to both neutrino and antineutrino data: (Δm^2,$\sin^2 2\theta$) = ($0.037\,\mathrm{eV}^2$,1.00), center is the best fit to neutrino data ($3.14\,\mathrm{eV}^2$, 0.002) and bottom is the best fit to antineutrino data ($0.05\,\mathrm{eV}^2$, 0.842). On all plots the full 3+1+matter effects solution is shown in addition to the solution neglecting solar neutrino oscillations and matter effects.

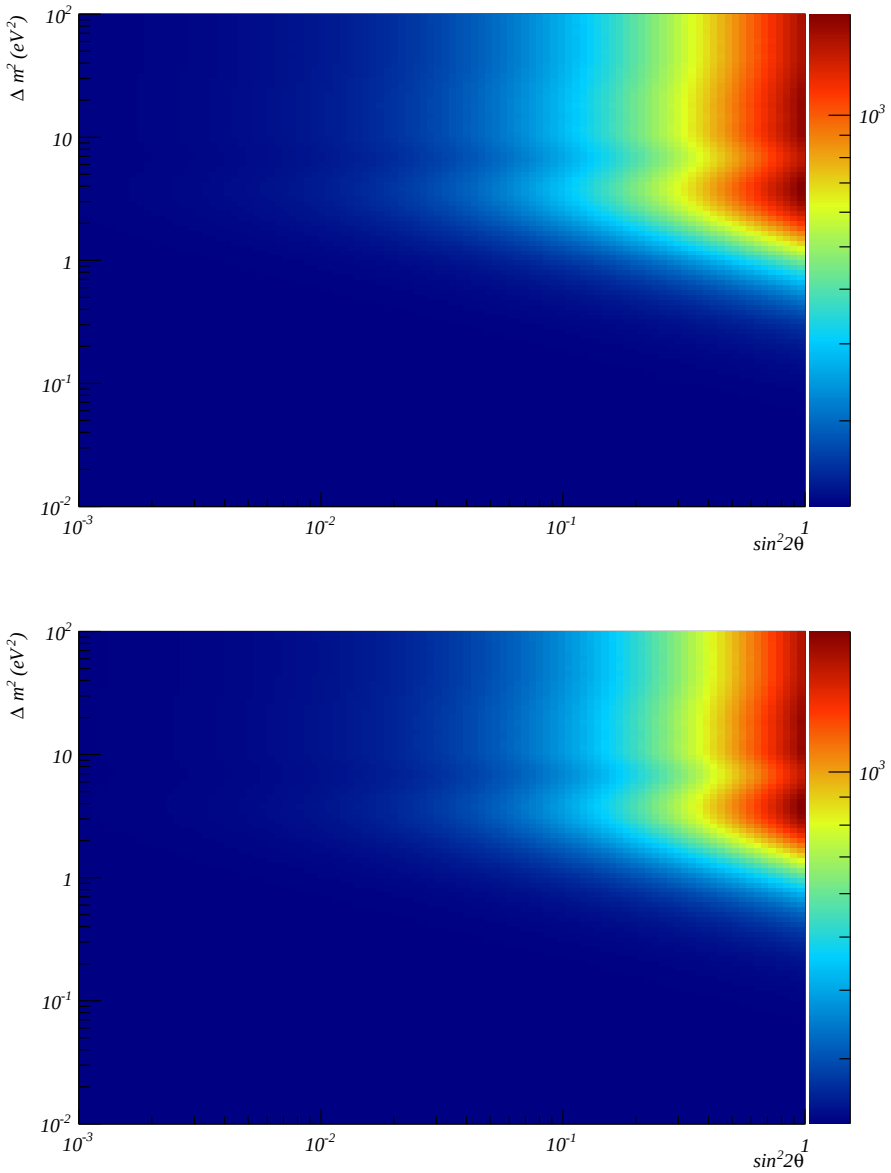


Figure 6.12: Expected numbers of ν_e candidates at the ND280 for Run 2, as a function of the short baseline oscillation parameters. The top plot shows the standard selection, with $E > 400$ MeV, and the lower plot shows the extended region, with $E > 200$ MeV.

The total numbers of expected ν_e candidates, as a function of the oscillation parameters, can be seen in Figure 6.12.

6.6 Systematic and Statistical Errors

For each point in the parameter space considered in Figure 6.12, the total uncertainty [2], Δ, on the expected number of ν_e candidates, N_{exp} must be calculated. The largest contributions to these errors come from the uncertainty on the neutrino flux [3]: 15.4% [113] and the neutrino interaction cross-sections [124], shown in Table 6.2.

Interaction Type	% Error ($E_\nu < 2$GeV)	% Error ($E_\nu > 2$GeV)
CC QE	6%	6%
CC RES	30%	20%
CC COH	100%	100%
CC DIS	30%	25%
NC	36%	36%

Table 6.2: Relative cross section uncertainties for different neutrino interaction modes. Table from [124].

There is also a systematic error associated with the Tracker reconstruction and selection cuts. My selection has similar cuts to those presented in [124], so the systematic error associated with that selection, 5.7%, will be used here. There is also a statistical error on the number of events expected, which is just the Poisson error, $\Delta^2_{\text{stat}} = N_{\text{exp}}$.

When calculating the cross section error, it is necessary to know what fraction of N_{exp} is made up of the different neutrino interaction modes, at each different point in the oscillation parameter space. Since the selection has a high energy cut at 2 GeV, the cross section errors for E $<$ 2 GeV will be used. The total (absolute) cross section error is given, at each point in the oscillation parameter space, by:

[2] Here Δ will be used to denote an absolute error, and σ will be used to denote a relative error.

[3] Here the flux errors will be assumed to be flat in neutrino energy, this is something that could be improved in future analyses.

$$\Delta^2_{\text{x-sec}} = \sum_i (N_i.\sigma_i)^2 \tag{6.7}$$

Where i = CCQE, CC coherent, CC resonant and CC DIS. The total variance in the number of events at each point in the oscillation parameter space is then given by:

$$\Delta^2 = \Delta^2_{\text{x-sec}} + N^2_{\text{exp}}(\sigma^2_{\text{flux}} + \sigma^2_{\text{sel}} + \sigma^2_{\text{eff}}) + N_{\text{exp}} + \Delta^2_{\text{MC stat}} \tag{6.8}$$

Where σ_{sel} is the uncertainty on the selection and reconstruction of ν_e events, and $N_{\text{exp}} = \Delta^2_{\text{stat}}$. Errors due to the finite MC statistics used also need to be taken into account, $\Delta_{\text{MC stat}}$ is the statistical error on the number of expected ν_e events for the MC, and $\sigma_{\text{eff}} = 3\%$ is the binomial error on the ν_e selection efficiency due to the finite MC statistics.

The absolute errors, Δ, on the expected number of ν_e candidates, at each point in the oscillation parameter space, can be seen in Figure 6.13. In the background only case, the $\Delta = 22.2$ for the standard selection, $E > 400$ MeV, and $\Delta = 44.9$ for the extended search region, $E > 200$ MeV.

6.7 Results

In both the standard ($E > 400$ MeV) and the extended ($E > 200$ MeV) ν_e appearance searches, no excesses of ν_e candidates are seen, and the observed number of ν_e candidate events is within $1\,\sigma$ of the expected number of ν_e candidate events. The expected and observed numbers of ν_e candidates, as a function of reconstructed neutrino energy, were shown in Figure 6.8.

The ν_e appearance data can then be used to place a limit on the possible values of the short baseline oscillation parameters θ and Δm^2. The standard log-likelihood maximisation procedure, including systematic errors, from [133]

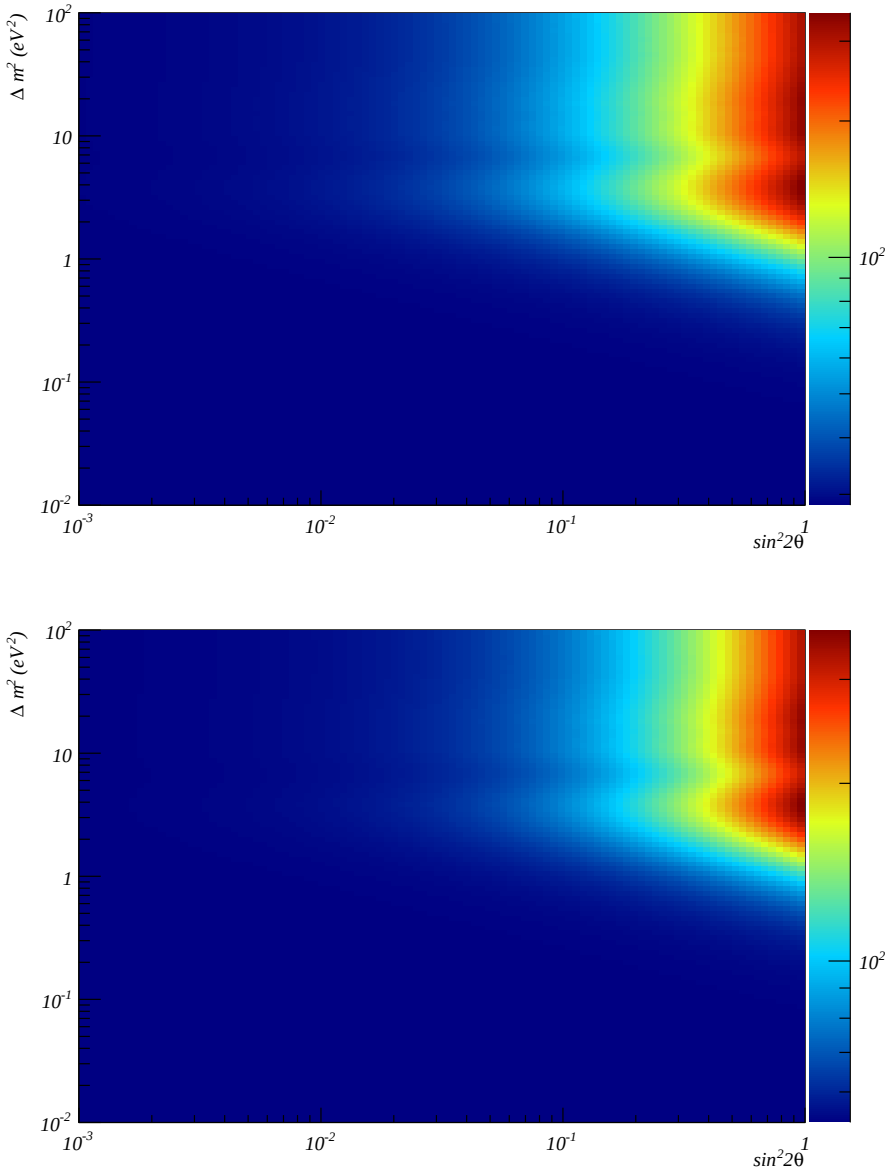


Figure 6.13: The absolute uncertainty in the expected number of ν_e candidates at different points in the short baseline oscillation parameter space. The top plot shows the standard selection, $E > 400$ MeV, and the bottom plot shows the extended region, $E > 200$ MeV.

will be followed here. The function to be minimised is $-2\log\mathcal{L}$:

$$-2\log\mathcal{L} = 2\left(N_{\text{exp}} - N_{\text{obs}}\log N_{\text{exp}}\right) + \frac{s^2}{\sigma^2} \tag{6.9}$$

Where N_{obs} is the observed number of ν_e candidates in the counting experiment, N_{exp} is the expected number of ν_e candidates, at the point in the short baseline oscillation parameter space, σ is the total relative error on N_{exp}, and s is a systematic shift applied to the expected number of ν_e candidates: $N_{\text{exp}} = \mu(1+s)$, where μ is the expected number of events if there were no systematic errors. This means that an alternative way to write equation (6.9) is:

$$-2\log\mathcal{L} = 2\left(\mu(1+s) - N_{\text{obs}}\log\mu(1+s)\right) + \frac{s^2}{\sigma^2} \tag{6.10}$$

In order to minimise this quantity, for each point in the short baseline oscillation parameter space, the value of s required for equation (6.10) to be minimised will be calculated analytically, as suggested in [126]. Differentiating the right hand side of equation (6.10), with respect to s, and setting it equal to zero:

$$\begin{aligned} 0 &= \mu - \frac{N_{\text{obs}}}{1+s} + \frac{s}{\sigma^2} \\ &= s^2 + (1+\mu\sigma^2)s + (\mu - N_{\text{obs}})\sigma^2 \end{aligned} \tag{6.11}$$

Solving equation (6.11) for s:

$$s = \frac{-(1+\mu\sigma^2) \pm \sqrt{(1+\mu\sigma^2)^2 - 4\sigma^2(\mu - N_{\text{obs}})}}{2} \tag{6.12}$$

Both solutions were tried, but it is always the positive root that gives the minimum. After the minimum value of the log-likelihood is found, at each point in the oscillation parameter space, the overall minimum log-likelihood is found [4].

[4] In order to definitely find the global minimum, a linear grid is created in addition to the

This value is then subtracted from the minimum log-likelihood value at each point in the oscillation parameter space.

Confidence levels are then drawn by including any points for which the difference in log-likelihood from the global minimum is less than a certain value. For the 90% CL in two dimensions, the difference in log-likelihood must be less than 4.61 [133] for the point in the oscillation parameter space to be included.

The 90% confidence level measurement, for the standard $E > 400$ MeV selection, is shown in Figure 6.14. The excluded region is to the upper right hand side of the contour. If the extended search region is used, the limit is weaker. The current sensitivity is not competitive with MiniBooNE; the future sensitivity is considered in Section 6.8.

6.8 Future Sensitivity and Possible Improvements

In this section I consider the future sensitivity, assuming this ν_e selection can be improved to get a ν_e selection efficiency improved by 10%. I also assume that the PØD can be included in this ν_e selection, doubling the fiducial volume of the search [5]. The full T2K expected running period, consisting of a total of 5 $\times 10^{21}$ pot, is assumed. Due to the increased statistics, instead of doing a counting experiment, the ν_e candidate events are binned in reconstructed neutrino energy, in 200 MeV bins. For the oscillation signals, this requires that the true neutrino energies be converted to reconstructed neutrino energies using the histograms in Figure 6.7.

For the systematic errors, it is possible to constrain the flux and neutrino interaction cross-section errors using the ν_μ events in the ND280. Such a tech-

log-log grid that the results are shown on. This is necessary, for example, in the case where there are no, or very small, short baseline oscillations and the global best fit point will be close to zero.

[5] It has yet to be seen whether the PØD will be able to perform such a selection with the assumed efficiencies and purities.

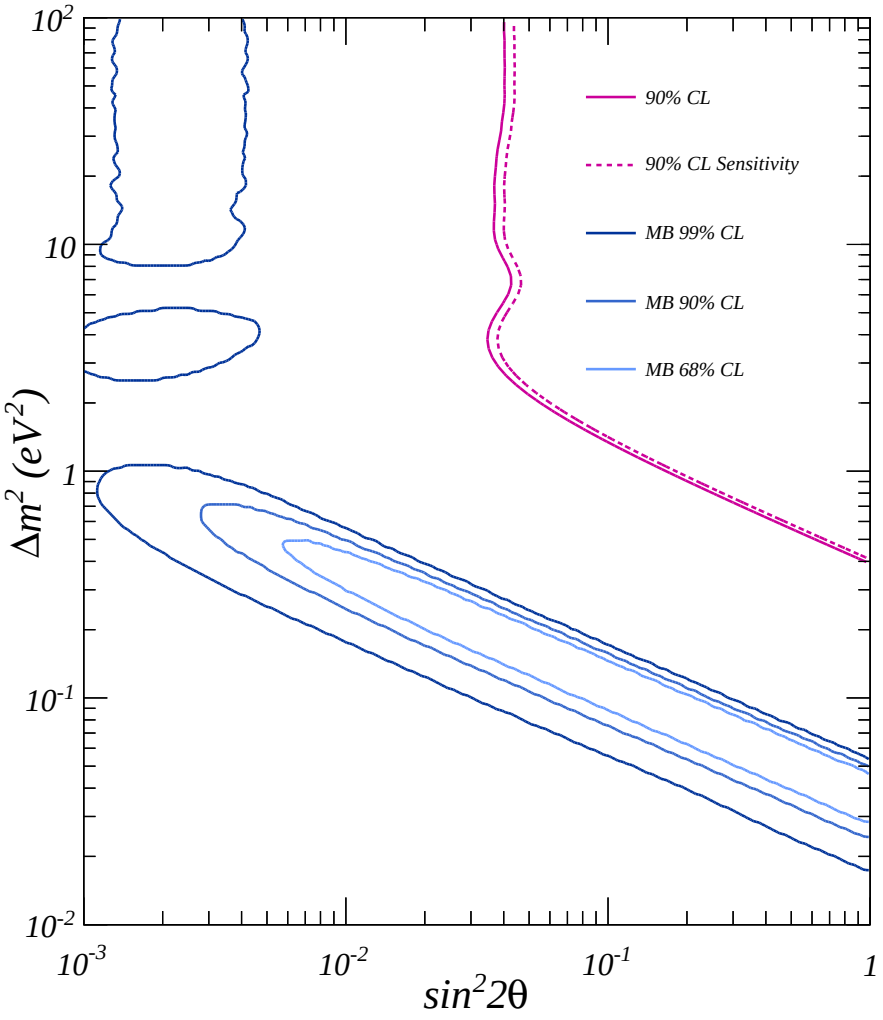


Figure 6.14: Limit on short baseline oscillations $\nu_\mu \rightarrow \nu_e$ from T2K ND280 ν_e appearance. The region to the upper right hand side of the contour is excluded at 90% CL. Also shown are the current ND280 90% CL sensitivity, and the MiniBooNE preferred region of the parameter space from [120].

nique was used by MiniBooNE [120] to give a total systematic error of less than 5%. In the sensitivity plots in this section I will assume that the total systematic error on each energy bin is 5% (red) and 10% (orange). I will also assume that these errors are uncorrelated between the bins, since the ν_μ measurement should largely remove the uncertainty due to the overall normalisation [6]. Figure 6.15 shows the 90% CL sensitivity prediction, with all of the above assumptions, and Figure 6.16 shows the 99% CL sensitivity prediction.

The sensitivity for this predicted ND280 analysis is good enough to exclude some regions of the MiniBooNE 99% CL preferred regions at the higher values of Δm^2. As previously mentioned, the ND280 tracker region has the major advantage of being able to distinguish between electrons and photons. Ideally both ν_e CC and single γ searches would be performed to look for possible event excesses that could be compatible with the MiniBooNE low energy excesses. Although it is much harder to separate e-like from γ-like tracks in the PØD, a MiniBooNE-style search would be possible.

[6] If these measurements are actually to be made then the covariances between the bins would need to be properly calculated and included.

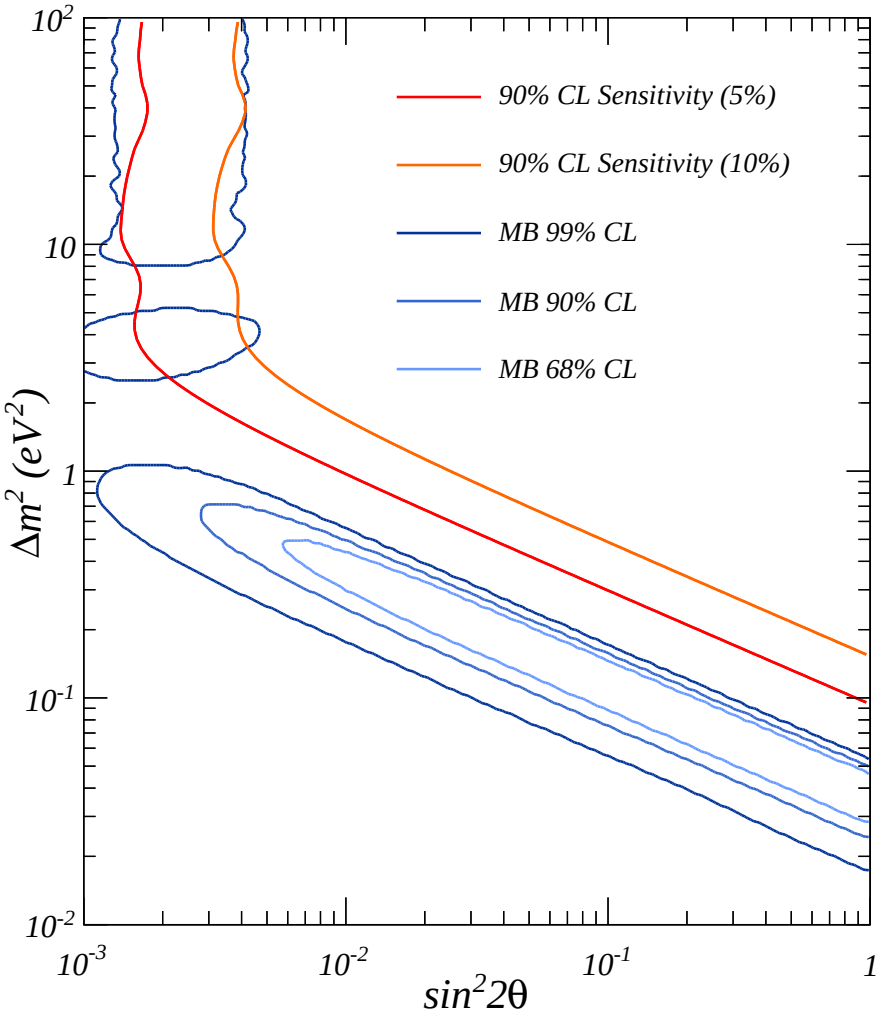


Figure 6.15: ND280 future sensitivity prediction for 5 $\times 10^{21}$ pot, 10% efficiency improvement and inclusion of the PØD. The 90% CL exclusion contours are shown for different values of the systematic error on the flux and cross-sections. The MiniBooNE preferred region of the parameter space from [120] is also shown.

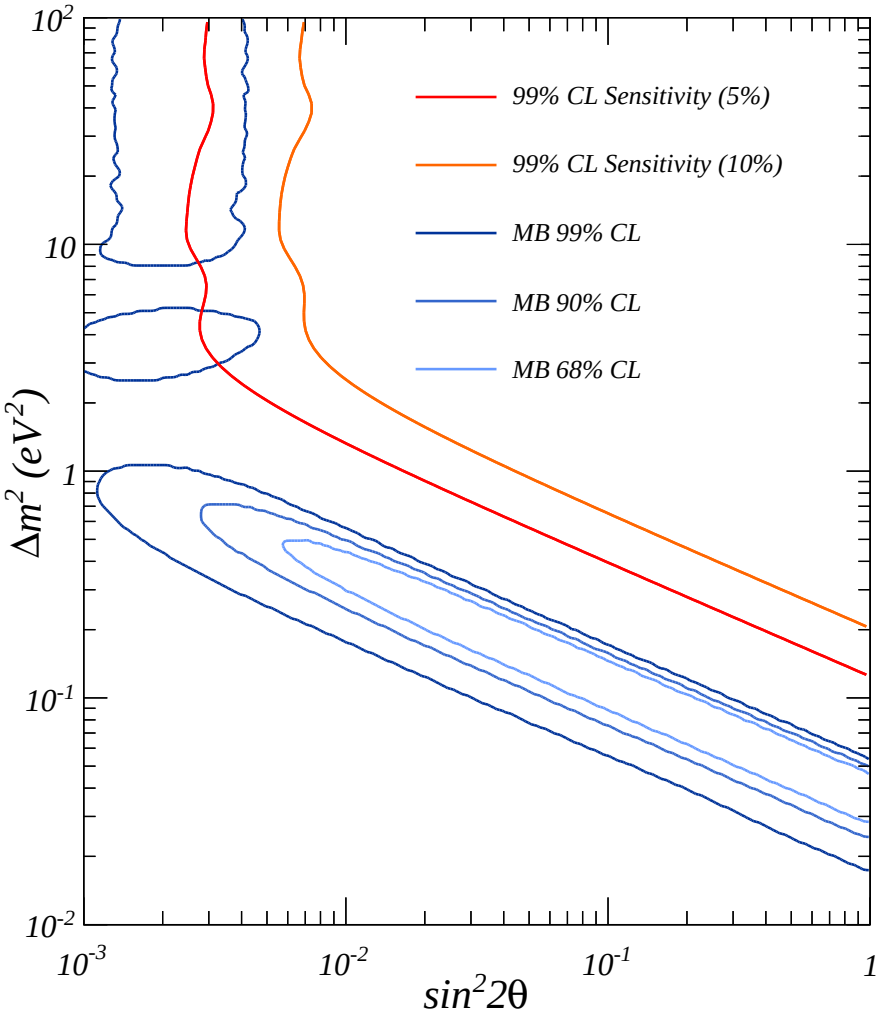


Figure 6.16: ND280 future sensitivity prediction for 5 $\times 10^{21}$ pot, 10% efficiency improvement and inclusion of the PØD. The 99% CL exclusion contours are shown for different values of the systematic error on the flux and cross-sections. The MiniBooNE preferred region of the parameter space from [120] is also shown.

Chapter 7

Combined MINOS and T2K Standard ν_e Appearance Analysis

In this chapter the electron neutrino appearance measurements of two long-baseline neutrino oscillation experiments: T2K and MINOS, will be combined to give improved limits on the neutrino oscillation parameters θ_{13} and δ from appearance measurements. This combination is performed using the method of Feldman and Cousins [127].

This chapter begins with a description of the two experiments' electron neutrino appearance measurements, followed by a description of the Feldman-Cousins Method in Section 7.4. Following this the technical details of the combination, including the possibility of correlated systematic errors, are discussed. Finally, prospects for including other neutrino experiments in such a combination are outlined in Section 7.8.

7.1 Motivation

In order to increase our knowledge of θ_{13}, the results of multiple experiments that are sensitive to this parameter can be combined. Such combinations can be

performed in different ways, depending on how much information is available about the original measurements.

In this chapter, the results of two long-baseline electron neutrino appearance experiments, MINOS and T2K, will be combined to give improved limits on θ_{13} and δ from $\nu_\mu \rightarrow \nu_e$. Somewhat detailed information is needed from the two experiments, due to the use of the Feldman-Cousins method to define acceptance regions for each point in the parameter space. It is particularly important to use the Feldman-Cousins method in this combination as the parameter θ_{13} is known to be small; the Feldman-Cousins technique was developed to deal with such cases, since conventional methods for determining acceptance regions can produce incorrect coverage or null contours if parameter values are near to physical boundaries.

7.2 The T2K ν_e Appearance Measurement

The T2K Experiment looks for ν_e appearance in a predominantly ν_μ beam. This experiment is described in detail in Chapter 3 of this thesis. The ν_e analysis is conducted by looking for an excess of electron-like Čerenkov rings in the far detector, Super-Kamiokande. The procedure for selecting ν_e candidates at SK, and the normalisation using near detector ν_μ charged current interactions, is described in detail in Chapter 5.

T2K released their first electron neutrino appearance results from the first two run periods [113]. Six ν_e candidates were observed, against an expected background of 1.5 ± 0.3 events. This was inconsistent with the $\theta_{13} = 0$ hypothesis at $2.5\ \sigma$ (99.3% CL). Allowed values for $\sin^2 2\theta_{13}$ and δ, at 90% and 68% confidence levels, can be seen in Figure 7.1.

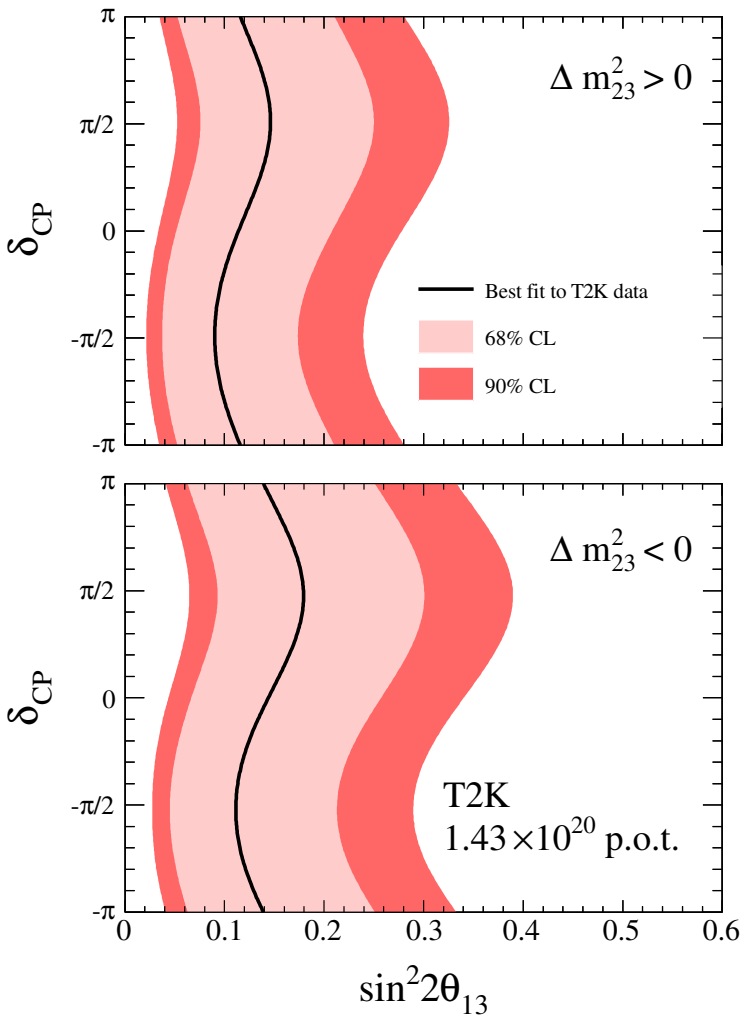


Figure 7.1: The Feldman Cousins allowed regions for the parameters $\sin^2 2\theta_{13}$ and δ at 90% and 68% confidence levels from the first two T2K run periods. Plot from [110]

7.3 The MINOS ν_e Appearance Measurement

MINOS is also a long baseline accelerator neutrino experiment, whose baseline can be seen in Figure 7.2, at similar L/E to T2K, in which a predominantly ν_μ beam is created by colliding protons onto a target, then magnetically focusing the resultant charged mesons and allowing them to decay. The neutrino beam thus produced is sampled at source by a near detector 1 km away, and then by a far detector at a distance of 735 km [128]. The beam energy is peaked at 3 GeV, slightly above the energy of the maximum oscillation probability. The two

MINOS detectors are almost identical in technology to minimise the systematic errors on their measurement: both are magnetised steel scintillator tracking detectors, the main difference is that the far detector is 5.4 kton whereas the near detector is only 0.98 kton to account for the difference in neutrino flux. The steel planes are 2.54 cm thick and are interspersed with 1cm planes of plastic scintillator. The MINOS far detector can be seen from the front in Figure 7.3. The neutrino interactions are predominantly deep inelastic scattering events due to their high energy, with ν_μ charged current (CC) interactions being distinguished from neutral current (NC) interactions by their long muon track, in addition to the hadronic shower.

MINOS has made a significant contribution, in particular, to our understanding of the mass squared splitting associated with atmospheric neutrino oscillations, with World-leading measurements in both ν_μ [38] and $\overline{\nu}_\mu$ [39] disappearance channels.

To search for electron neutrino appearance, it is necessary to identify the superimposed electro-magnetic and hadronic showers created by a deep inelastic electron neutrino CC interaction, against a large background of hadronic showers from NC interactions. This difficulty in particle identification (PID) is overcome using a Library Event Matching (LEM) technique. In this method, each ν_e candidate is compared to a library of 5×10^7 Monte Carlo events (signal and background) to decide on the PID. The reconstructed neutrino candidates are binned into five different energy ranges, and three bins of LEM, and the number of observed ν_e candidates relative to that predicted in each bin, in the case $\theta_{13} = 0$, as can be seen in Figure 7.4, is used to give confidence contours to constrain $2\sin^2 2\theta_{13}\sin^2\theta_{23}$. The MINOS confidence intervals constraining θ_{13} can be seen in Figure 7.5. MINOS have found a slight excess of ν_e-like events, excluding $\theta_{13} = 0$ at 89% CL [129] (1.2 σ).



Figure 7.2: The MINOS experiment sends a mostly ν_μ beam 735 km from Fermilab to the Soudan mine. Image from [131]

7.4 The Feldman-Cousins Method

When we try to produce confidence intervals for physical parameters, in general some log-likelihood function, $\log \mathcal{L}$ [1], will be constructed, and the value of this quantity at all points in the parameter space will be calculated using the experimental data. The minimum value of $-\log \mathcal{L}$ will be found and subtracted from all the other points in the parameter space to give a surface in elevations of $\Delta \log \mathcal{L}$. To give confidence intervals, contours will then be drawn at fixed

[1] In this thesis, $\log$ will always denote the natural logarithm.



Figure 7.3: The MINOS far detector is a steel/scintillator tracking calorimeter. Image from [132]

$\Delta \log \mathcal{L}$ elevations appropriate to the confidence levels of interest [133] [2].

After we have conducted our experiment, what we really want to know is the region of parameter space that the true values of the oscillation parameters are contained in at some given confidence level (CL). Following the procedure of constructing contours at fixed $\Delta \log \mathcal{L}$ elevations, we are told rather the region of parameter space that any experiment's best fit point will be contained in at that confidence level, if the true values of the oscillation parameters are at our experiment's best fit point.

There are two options to resolve this issue, the fixed-elevation contours can be inverted in their meaning, using Bayes' theorem, or we can use the Feldman-Cousins method. If Bayes' theorem is used to find the probability of some theory (in our case the physical parameters governing neutrino oscillations) A,

[2] Actually, the function used for these confidence levels is $\Delta 2 \log \mathcal{L}$.

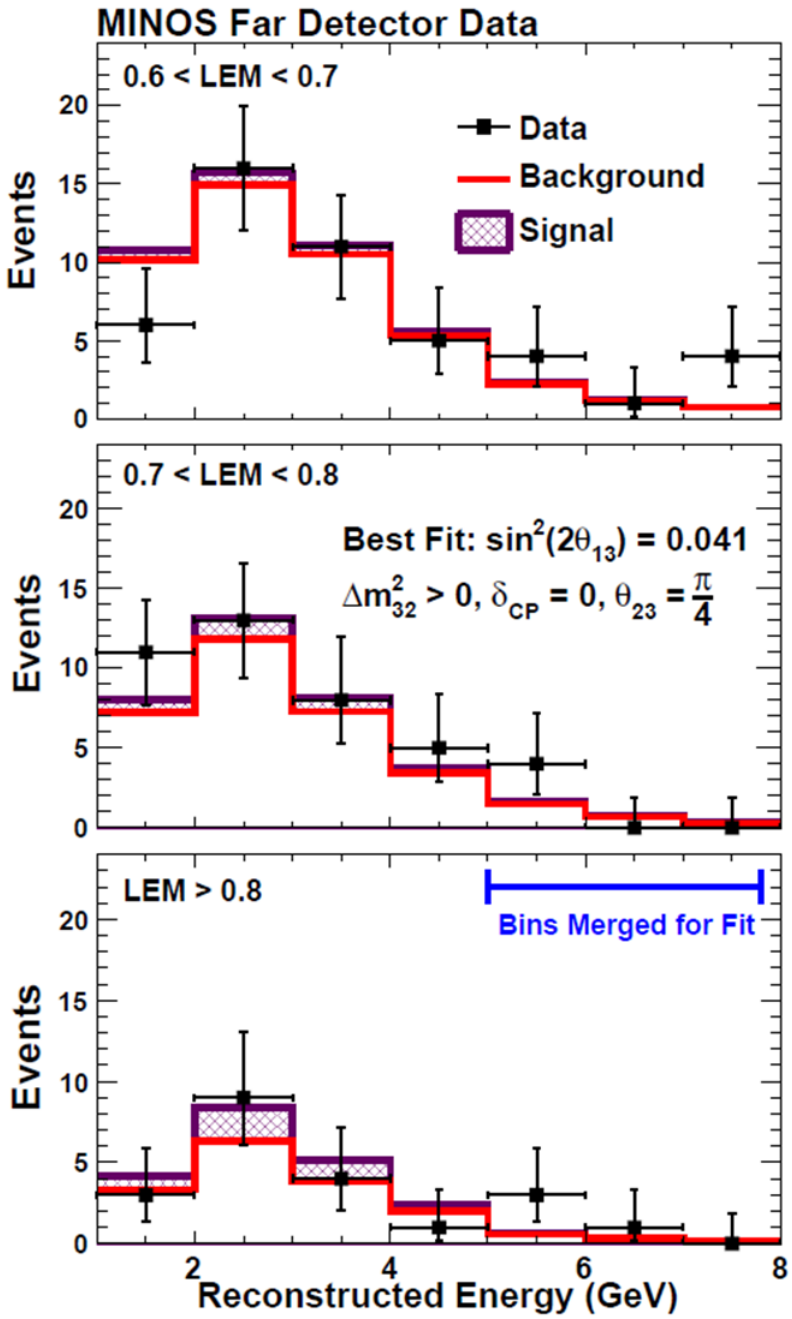


Figure 7.4: The MINOS ν_e candidates in bins of reconstructed energy and library event matching parameter (LEM). The red line shows the expected number of ν_e candidates in each bin if $\theta_{13} = 0$, and the purple shaded region shows the signal expected from the MINOS best fit value of $\sin^2 2\theta_{13} = 0.041$. Figure from [129].

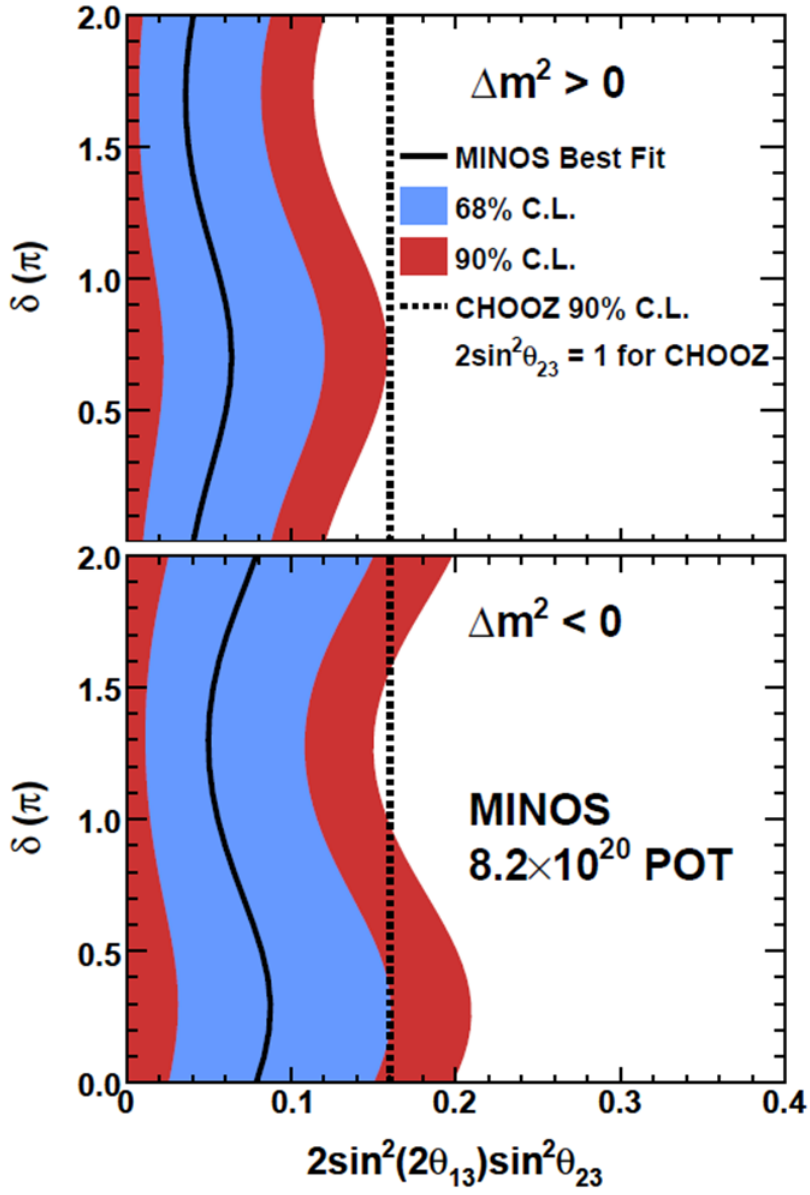


Figure 7.5: The MINOS 68% and 90% confidence level Feldman-Cousins allowed regions for $2\sin^2 2\theta_{13}\sin^2\theta_{23}$ as a function of δ. The top plot is for the normal neutrino mass hierarchy and the bottom plot is for the inverted neutrino mass hierarchy. Figure from [129].

given we have observed some experimental result B, denoted $P(A|B)$, when our measurement actually tells us $P(B|A)$, prior probability distributions need to be assumed for the two variables, $P(A)$ and $P(B)$:

$$P(A|B) = \frac{P(B|A)\,P(A)}{P(B)} \tag{7.1}$$

These prior distributions will in general not be known and the result will depend on the choice of prior. In order to get around these unknowns we can instead follow the procedure of Feldman and Cousins to construct confidence intervals.

In this combination the Feldman-Cousins method will be used, as it is in both of the individual experiments' analyses, since $\sin^2 2\theta_{13}$ is known to be close to the physical boundary (zero).

The crucial point to the Feldman-Cousins method is that at each point in the possible parameter space *i.e.* for all values of (θ_{13},δ), a critical value of the $\Delta\log\mathcal{L}$, $\Delta\log\mathcal{L}_{\text{crit}}$, must be calculated. In fact, one must be calculated for each CL of interest, for example the 90% CL $\Delta\log\mathcal{L}_{\text{crit}}$ is defined as:

$$\begin{aligned}\Delta\log\mathcal{L}_{\text{crit(90\%CL)}}(\theta_{13},\delta) \;\equiv\; & \Delta\log\mathcal{L}(\theta_{13},\delta) : \\ & P(\Delta\log\mathcal{L}_{\text{toy}}(\theta_{13},\delta) < \Delta\log\mathcal{L}(\theta_{13},\delta)) = 0.9\end{aligned} \tag{7.2}$$

That is to say that 90% of the toy experiments (more on this in Section 7.4.2), generated about a point in (θ_{13},δ) space, will have a value of $\Delta\log\mathcal{L}(\theta_{13},\delta)$ that is less than or equal to the critical value of delta log-likelihood at that point in the parameter space. To summarise, the Feldman-Cousins method goes as follows:

- A large number of toy experiments are generated at each point in the

parameter space. For each toy experiment, the log-likelihood is calculated at all points under consideration in the parameter space (θ_{13}, δ). The value of delta log-likelihood is then found by taking the difference between the log-likelihood at the true oscillation parameters (those the toy experiment was generated assuming) and the log-likelihood at the best fit to the toy experiment. For each toy experiment all of the values of delta log-likelihood are recorded, and this is done individually for each point in the parameter space we are considering.

- The $\Delta \log \mathcal{L}$, for a given point in the parameter space, are then ordered, so that a value $\Delta \log \mathcal{L}_{\text{crit}}$ can be calculated, as defined in Equation 7.2. This is done for each point under consideration in the parameter space, and for each confidence level of interest. In this way maps of different values of $\Delta \log \mathcal{L}_{\text{crit}}$ are built up covering the entire parameter space.

- A map of $\Delta \log \mathcal{L}_{\text{data}}$ across the whole parameter space is then calculated, for the data, by subtracting the best fit log-likelihood to the data from the log-likelihood at each point in the parameter space.

- Finally, for each point in the parameter space, if $\Delta \log \mathcal{L}_{\text{data}}$ is less than $\Delta \log \mathcal{L}_{\text{crit}}$, then that point is included in the allowed region at the given confidence level, otherwise it is excluded.

7.4.1 Inputs from MINOS and T2K

The parameter space chosen for the combined analysis is $\sin^2 2\theta_{13} \in [0, 1]$ and $\delta \in [0, 2\pi)$. The inputs needed from the two experiments are the expected number of ν_e-like events in each bin, $\mu_i(\theta_{13}, \delta)$, at each point in the parameter space (θ_{13}, δ), the observed number of ν_e candidates in each bin, N_i, and a covariance matrix $\{V_{ij}(\theta_{13}, \delta)\}$, at each point in the parameter space (θ_{13}, δ). The covariance

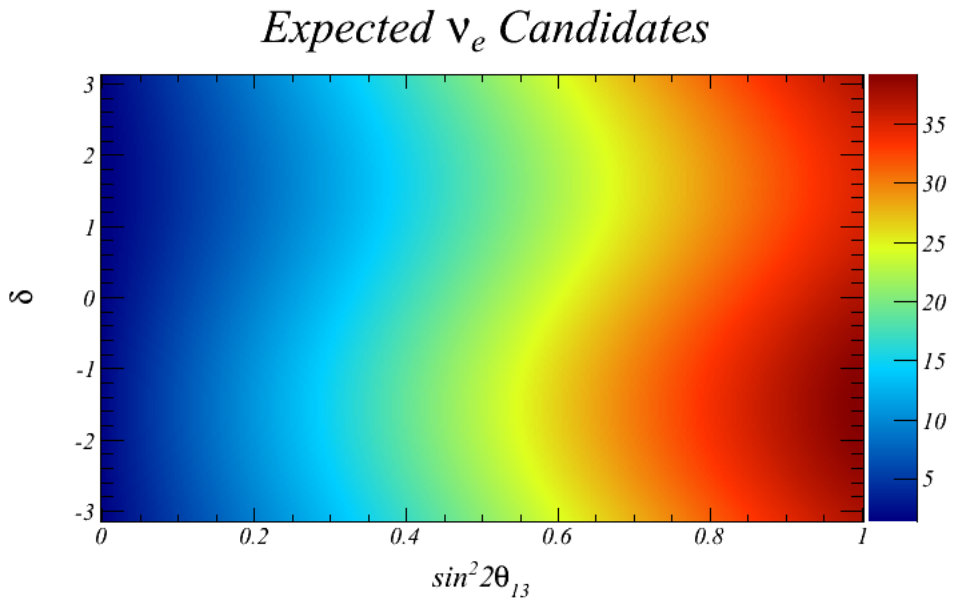


Figure 7.6: Expected number of ν_e-like events in the T2K far detector as a function of $\sin^2 2\theta_{13}$ and δ.

matrix is defined, in terms of the expected number of events in each bin, μ_i, as:

$$V_{ij} \equiv \left\langle (\mu_i - \overline{\mu}_i)\left(\mu_j - \overline{\mu}_j\right)\right\rangle \tag{7.3}$$

Examples of such inputs are shown in Figures 7.6 and 7.7. Note that these covariance matrices will only be internal to each experiment, covariances between errors for the two experiments will be discussed in Section 7.5.3.

7.4.2 Toy Experiment Generation

The two experiment system is treated like a single experiment with different bins, fifteen bins from MINOS corresponding to their different energy and LEM bins, and one bin from T2K. At each point in the parameter space, 10^4 "toy" experiments are generated for the purpose of finding $\Delta \log \mathcal{L}_{\text{crit}}$. The first stage in the toy experiment generation is to apply a shift in the expected number of events due to the total statistical plus systematic uncertainty in the expected

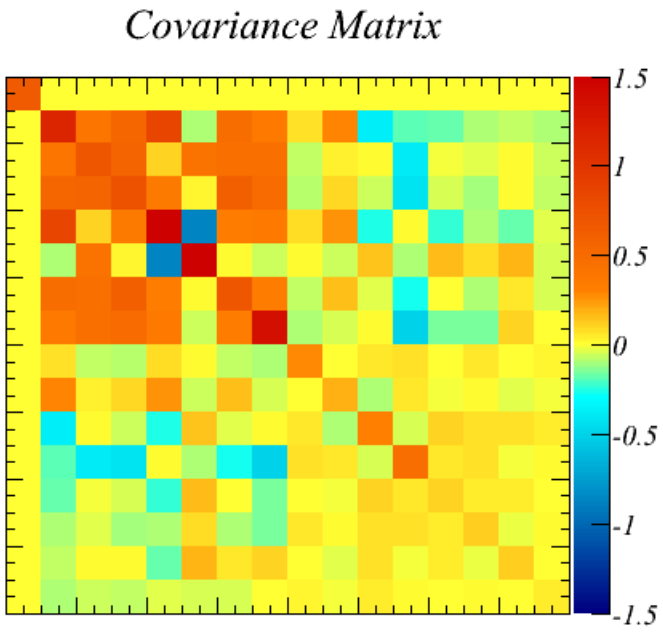


Figure 7.7: Example of a combined covariance matrix for the two experiment system, taken at $\sin^2 2\theta_{13} = 0.09$ and $\delta = 0.56$. The bin $(0,0)$ contains the T2K σ^2. The bins $(0,i)$ and $(i,0)$ are empty when there are no correlated systematic errors between the experiments. The MINOS covariance matrix fills the remainder — bins are ordered according to energy and LEM as $(\mathrm{E}_1, \mathrm{LEM}_1)$, $(\mathrm{E}_1, \mathrm{LEM}_2)$, $\ldots$, $(\mathrm{E}_5, \mathrm{LEM}_2)$, $(\mathrm{E}_5, \mathrm{LEM}_3)$.

number of events. We can express this as:

$$n_i^{\mathrm{exp}} \rightarrow n_i^{\mathrm{exp}} + x_i \tag{7.4}$$

where n_i^{exp} is the expected number of events in the ith bin, and x_i is a shift due to the total error. Since there may be correlations between the errors in different bins, these need to be considered when calculating the shifts. We assume that the shifts due to the errors follow a multi-variate normal distribution, $\mathrm{x} \sim \mathcal{N}(\mathbf{0}, V)$, so their joint probability density function satisfies:

$$f(\mathbf{x}) \propto e^{-\frac{1}{2}\mathbf{x}^\top V^{-1}\mathbf{x}} \tag{7.5}$$

where V is the covariance matrix. To generate the vector of correlated shifts, $\mathbf{x}$, we can use a vector of independent, normally distributed random variables, $\mathbf{y}$, and a transformation matrix, $L^\top$:

$$\mathbf{x} = L^\top \mathbf{y} \tag{7.6}$$

Now, $\mathbf{y}$ follows a multivariate normal distribution, with $\mu = \mathbf{0}$ and $\sigma_i = 1$ (*i.e.* the covariance matrix is the identity), for ease in our use of the random number generation, $\mathbf{y} \sim \mathcal{N}(\mathbf{0}, \mathbb{1})$. The transformation matrix has no effect on the expectation since $L^\top \mathbf{0} = \mathbf{0}$. The covariance matrix will be changed however:

$$\begin{aligned} V_{ij} &= \left\langle y_i y_j^\top \right\rangle - \left\langle y_i \right\rangle \left\langle y_j \right\rangle^\top \\ &= \left\langle y_i y_j^\top \right\rangle \\ &\to \left\langle L^\top y_i y_j^\top L \right\rangle \\ &= L^\top \mathbb{1} L \end{aligned} \tag{7.7}$$

So we can write:

$$\mathbf{x} \sim \mathcal{N}(\mathbf{0}, L^\top \mathbb{1} L) \tag{7.8}$$

Since the distribution that $\mathbf{x}$ actually follows is just a multi-variate normal distribution:

$$\mathbf{x} \sim \mathcal{N}(\mathbf{0}, V) \tag{7.9}$$

We need to find a matrix $L^\top$ such that:

$$V = L^\top L \tag{7.10}$$

To find this transformation matrix, we use the fact that any symmetric, positive-definite matrix (such as a covariance matrix), can be expressed in this way in terms of a single upper-diagonal matrix, L, using the method of Cholesky decomposition. Now we can write:

$$V_{ij} = \sum_{k=0}^{i} L_{ki} L_{kj} \tag{7.11}$$

Where the sum stops at $k = i$ as L is upper-diagonal. Now if we split this into two cases, first $i = j$:

$$\begin{aligned} \sum_{k=0}^{i} L_{ki}^2 &= V_{ii} \\ L_{ii}^2 + \sum_{k=0}^{i-1} L_{ki}^2 &= V_{ii} \\ L_{ii} &= \left(V_{ii} - \sum_{k=0}^{i=1} L_{ki}^2 \right)^{\frac{1}{2}} \end{aligned} \tag{7.12}$$

Now the case $i \neq j$:

$$\begin{aligned} L_{ii} L_{ij} + \sum_{k=0}^{i-1} L_{ki} L_{kj} &= V_{ij} \\ L_{ij} &= \frac{1}{L_{ii}} \left(V_{ij} - \sum_{k=0}^{i-1} L_{ki} L_{kj} \right) \end{aligned} \tag{7.13}$$

The equations 7.12 and 7.13 can then be used to build up the matrix L. This is implemented using an algorithm from [134].

Once a random shift has been calculated, this new number of expected events is used to draw a Poisson random number to work out the number of ν_e candidates in each bin of the toy experiment.

The toy experiments must then be ordered in terms of the difference between their log-likelihood with the true oscillation parameters that they were generated from, and that with the toy experiment's best fit point. The likelihood function is described in Section 7.4.3. After the toy experiments have been ordered, the different values of $\Delta \log \mathcal{L}_{\text{crit}}$, for the different confidence levels of interest, can be found by counting the number of experiments from zero until the correct fraction is reached. An example of this ordering for the combination can be seen in Figure 7.8. The values of $\Delta \log \mathcal{L}_{\text{crit}}$ for the 90% CL, at different points in the parameter space, can be seen in Figure 7.9. The fact that the critical values of $\Delta \log \mathcal{L}$ are lower near to $\sin^2 2\theta_{13} = 0$ can be understood by thinking about the physical boundary at $\sin^2 2\theta_{13} = 0$. If a toy experiment is generated using parameters near to $\sin^2 2\theta_{13} = 0$ then it may prefer a value of $\sin^2 2\theta_{13}$ that is unphysical for its best fit point. Since this is not allowed, the difference between the values of the log-likelihood at the best fit point and the point the toy experiment was generated from will be reduced, leading to a lower value of the critical $\Delta \log \mathcal{L}$.

In the case where experiments have very discrete outcomes, so for T2K in particular when the number of ν_e candidates is expected to be small, it may be impossible to get the correct coverage. When this is the case we will always over-cover, waiting until we have at least the stated fraction of toy experiments with their $\Delta \log \mathcal{L}$ less than the critical value.

7.4.3 The Likelihood Function

The likelihood function for a multi-bin experiment is the product of the probability density functions for each bin. Since the number of events in a bin is a discrete quantity the Poisson probability density function is used, along with a multivariate normal probability density function describing the continuous

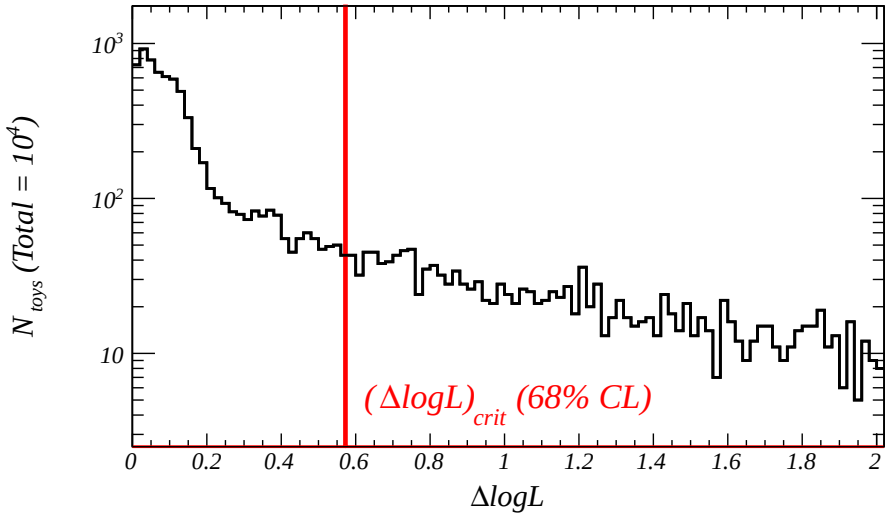


Figure 7.8: After the toy experiments are ordered in terms of their $\Delta \log \mathcal{L}$, critical values are found at the point where a certain fraction of the toy experiments have lower $\Delta \log \mathcal{L}$ than the critical value.

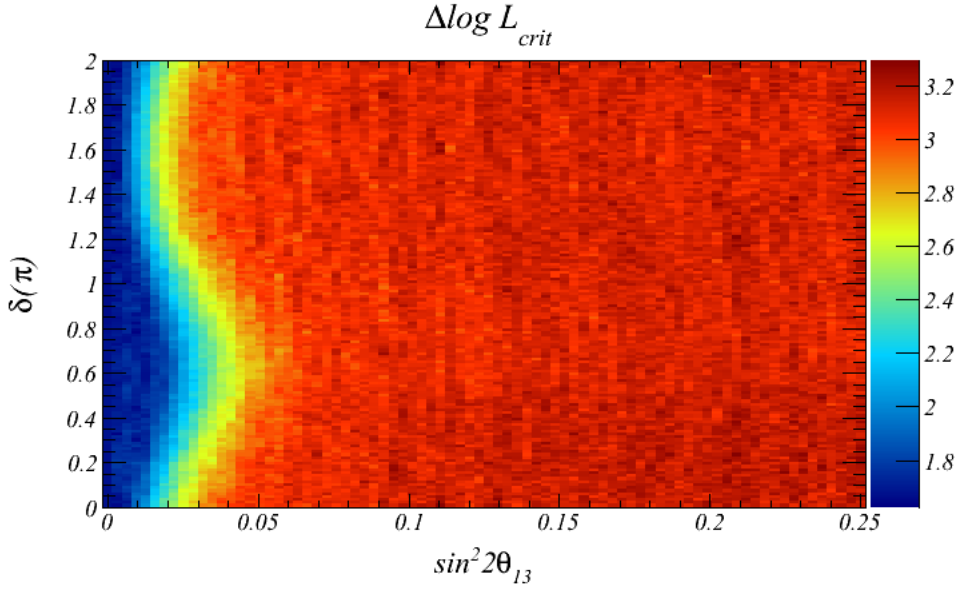


Figure 7.9: The values of $\Delta \log \mathcal{L}_{\text{crit}}$ for the 90% CL, at different values of $\sin^2 2\theta_{13}$ and δ. The values shown are for the combination of MINOS and T2K.

distribution in the expected number of events due to systematic errors:

$$\mathcal{L} = \prod_{i=0}^{n-1} \left(\frac{\mu_i(\theta_{13}, \delta, \mathbf{y})^{N_i} e^{-\mu_i(\theta_{13},\delta,\mathbf{y})}}{N_i!} \right) \frac{1}{(2\pi)^{\frac{n}{2}}} e^{-\frac{1}{2}\mathbf{y}^\top \mathbf{y}} \tag{7.14}$$

Where μ_i is the expected number of events in the ith bin, N_i is the observed number of events in the ith bin, n is the total number of bins and $\mathbf{y}$ is a vector of independent random numbers as before. Taking the natural logarithm as it simplifies the function and doesn't affect the location of the minimum:

$$\begin{aligned} \log \mathcal{L} \;\; = \;\; & \sum_{i=0}^{n-1} \left(N_i \log \mu_i(\theta_{13}, \delta, \mathbf{y}) - \mu_i(\theta_{13}, \delta, \mathbf{y}) - \log(N_i!) \right) \\ & -\frac{n}{2} \log(2\pi) - \frac{1}{2}\mathbf{y}^\top \mathbf{y} \end{aligned} \tag{7.15}$$

Also dropping the constant terms as they affect neither the location of the minimum nor the log-likelihood differences:

$$\log \mathcal{L} = \sum_{i=0}^{n-1} \left(N_i \log \mu_i(\theta_{13}, \delta, \mathbf{y}) - \mu_i(\theta_{13}, \delta, \mathbf{y}) \right) - \frac{1}{2}\mathbf{y}^\top \mathbf{y} \tag{7.16}$$

We also multiply by -2 to give the final expression for the log-likelihood function:

$$-2 \log \mathcal{L} = 2 \sum_{i=0}^{n-1} \left(\mu_i(\theta_{13}, \delta, \mathbf{y}) - N_i \log \mu_i(\theta_{13}, \delta, \mathbf{y}) + \frac{1}{2} y_i^2 \right) \tag{7.17}$$

To minimise the function $-2 \log \mathcal{L}$ the `MINUIT` minimiser is used via the `ROOT` framework [135]. The values of $\Delta \log \mathcal{L}$ for the combined MINOS and T2K dataset are shown in Figure 7.10.

The final step is to subtract the surface of critical $\Delta \log \mathcal{L}$ points from the $\Delta \log \mathcal{L}$ surface of the data. This can be seen in Figure 7.11. Contours are then drawn for the different confidence levels of interest at the point at which the

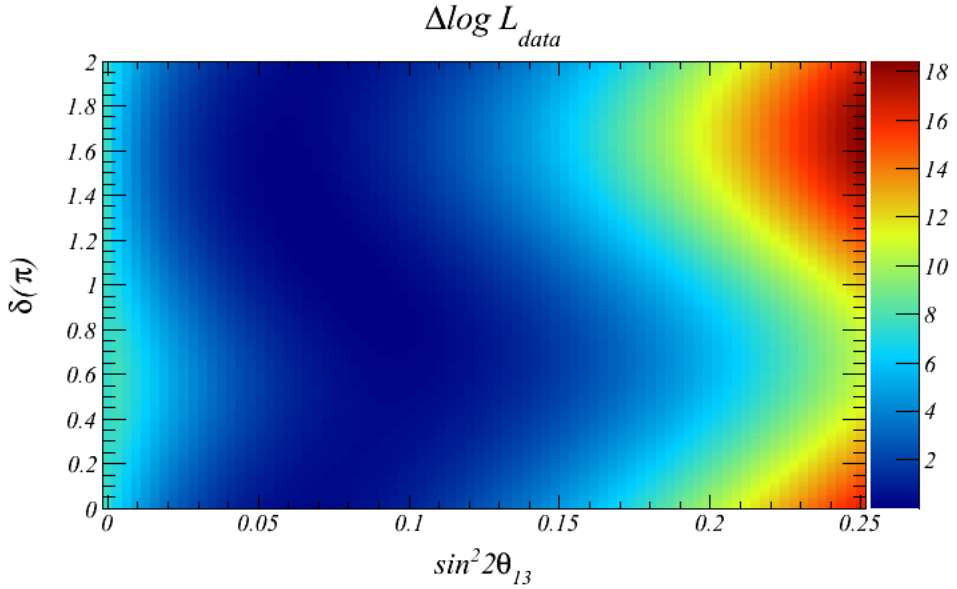


Figure 7.10: The values of $\Delta \log \mathcal{L}_{\text{data}}$ at different values of $\sin^2 2\theta_{13}$ and δ. The values shown are for the combination of MINOS and T2K.

surface crosses zero [3].

7.5 Considerations for the Combination

Performing the combined fit is not simply a case of treating the two experiments as a single experiment, as there are some differences in the way the two experiments perform their analyses that must be taken into account when performing the combination.

7.5.1 Oscillation Parameters and the Choice of x-Axis

One important difference is that MINOS allow all the oscillation parameters, used when calculating the expected numbers of events in each bin, to vary within their uncertainty as nuisance parameters in the fit. T2K, however, quote their measurement as being at fixed values of the other oscillation parameters.

[3] The contours are actually fitted for to remove the effects of the binning.

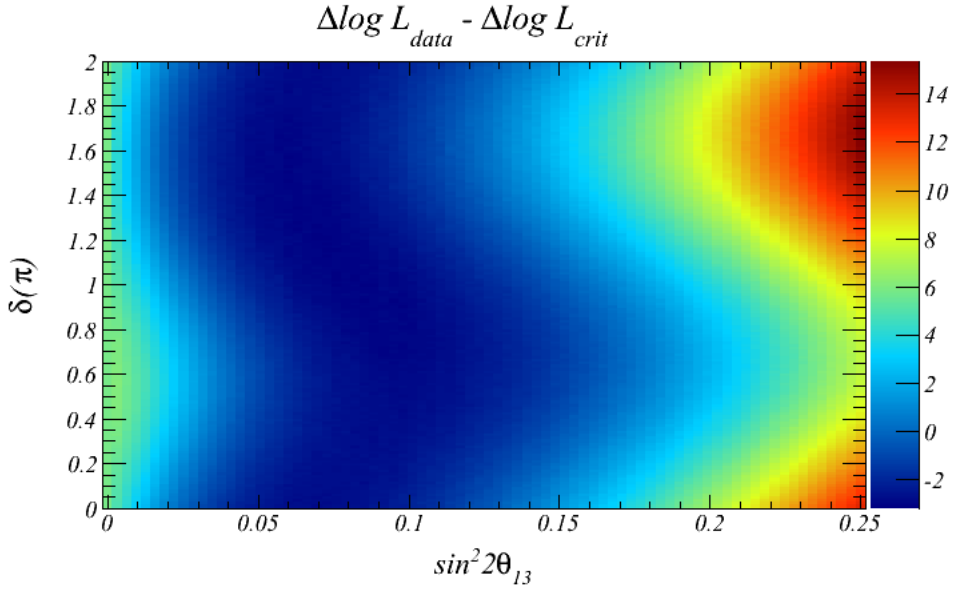


Figure 7.11: The values of $\Delta \log \mathcal{L}_{\text{data}} - \Delta \log \mathcal{L}_{\text{crit}}$, for the 90% CL, at different values of $\sin^2 2\theta_{13}$ and δ. The values shown are for the combination of MINOS and T2K.

The expected numbers of ν_e candidates in each bin at all points in the parameter space, and the corresponding covariance matrices, provided to us by MINOS, however, do not contain the effects of these uncertainties.

Another difference is that T2K show their results for $\sin^2 2\theta_{13}$ at a fixed value of $2\sin^2\theta_{23} = 1$, whereas MINOS show the combination $2\sin^2\theta_{23}\sin^2 2\theta_{13}$, by throwing θ_{23} between its errors and then choosing θ_{13} to keep this quantity fixed in each toy experiment. The systematic errors that MINOS have provided us with, however, do not include any uncertainty in the oscillation parameters (a fixed value of $2\sin^2\theta_{23} = 1$ is used). This means that our combination can be interpreted as constraining $\sin^2 2\theta_{13}$ at $2\sin^2\theta_{23} = 1$.

7.5.2 Systematic Errors in the Likelihood Function

There are some slight differences in the ways in which the two experiments perform their analyses, which must be considered when validating our method,

and when making a combination of their results. One difference is that MINOS minimise over the systematic errors contained in their likelihood function. T2K, however, define the likelihood function with only the Poisson probability density function so do not minimise over systematic errors. Since in general it may be advantageous to minimise over the systematic errors, we do include the systematic errors in the likelihood function for our example fit.

7.5.3 Combining Correlated Systematic Errors

In order to combine the errors from both experiments into a single covariance matrix, we need to consider the systematic errors that may be correlated between them. In the case of our example, most of the sources of error cited in [129, 113] can be assumed to be uncorrelated between experiments, due to the different experimental set-ups and different neutrino energies involved. However, cross section uncertainties between the single T2K bin (energies up to 1.25 GeV) and the MINOS low energy (1-2 GeV) bins are potentially correlated.

To assess the necessity of including this correlation, a worst-case estimate of its effect was made, by assuming complete correlation between the T2K cross-section error, and the total MINOS cross-section plus flux error, chosen as it is publicly available in [130].

To see how these correlated errors fit into the covariance matrix, the number of expected events in each bin can be re-defined to include a number of correlated systematic errors as follows:

$$\mu_i = \overline{\mu}_i + \sigma_i^{\text{uncorr}} y_i + \sum_{\alpha} c_{i\alpha} z_{\alpha} \tag{7.18}$$

Where α is an index running over all the correlated systematic errors, the z_α are normally distributed random numbers with mean zero and $\sigma = 1$ and the $c_{i\alpha}$ parametrise the size of the effect of correlated error α on bin i. Substituting this

into the definition of the covariance matrix:

$$\begin{aligned} V_{ij} &\equiv \left\langle (\mu_i - \overline{\mu}_i)\left(\mu_j - \overline{\mu}_j\right)\right\rangle \\ &= \left\langle \left(\sigma_i^{\text{uncorr}} y_i + \sum_\alpha c_{i\alpha} z_\alpha\right)\left(\sigma_j^{\text{uncorr}} y_j + \sum_\beta c_{j\beta} z_\beta\right)\right\rangle \\ &= \left\langle \sigma_i^{\text{uncorr}} y_i \sigma_j^{\text{uncorr}} y_j\right\rangle + \left\langle \sum_\alpha c_{i\alpha} z_\alpha \sigma_j^{\text{uncorr}} y_j\right\rangle + \\ &\qquad \left\langle \sigma_i^{\text{uncorr}} y_i \sum_\beta c_{j\beta} z_\beta\right\rangle + \left\langle \sum_\alpha c_{i\alpha} z_\alpha \sum_\beta c_{j\beta} z_\beta\right\rangle \end{aligned} \tag{7.19}$$

The terms that contain products $\langle y_i z_\alpha\rangle$ as well as those containing $\langle y_i y_j\rangle$, for $i \neq j$, or $\langle z_\alpha z_\beta\rangle$, for $\alpha \neq \beta$, are all zero as they can be split into the product of two distributions having expectation zero. This means that the second and third terms in Equation 7.19 are zero, and the remaining two are only non-zero when the indices are equal:

$$V_{ij} = \delta_{ij}\left(\sigma_i^{\text{uncorr}}\right)^2 \left\langle y_i^2\right\rangle + \sum_\alpha c_{i\alpha} c_{j\alpha} \left\langle z_\alpha^2\right\rangle \tag{7.20}$$

Now since the definition of the variance is $\text{Var}(x) = \langle x^2\rangle - \overline{x}^2$ and both y and z have mean zero and variance one, $\langle y_i^2\rangle = \langle z_\alpha^2\rangle = 1$:

$$V_{ij} = \delta_{ij}\left(\sigma_i^{\text{uncorr}}\right)^2 + \sum_\alpha c_{i\alpha} c_{j\alpha} \tag{7.21}$$

For the possibly correlated cross-section errors in this analysis, the fractional contribution to the bin uncertainty from the cross-section uncertainty was assumed to be constant in θ_{13} and δ, and the largest value published numbers allow. For MINOS, the total uncertainty on the background is 5.4%, from [129], and the uncertainty on flux and cross section (also detector simulations) is 0.7%, from [130]. This means that, for MINOS: $c_{i,\text{xsec}} = 0.1296\,\sigma_i$. Where σ_i here

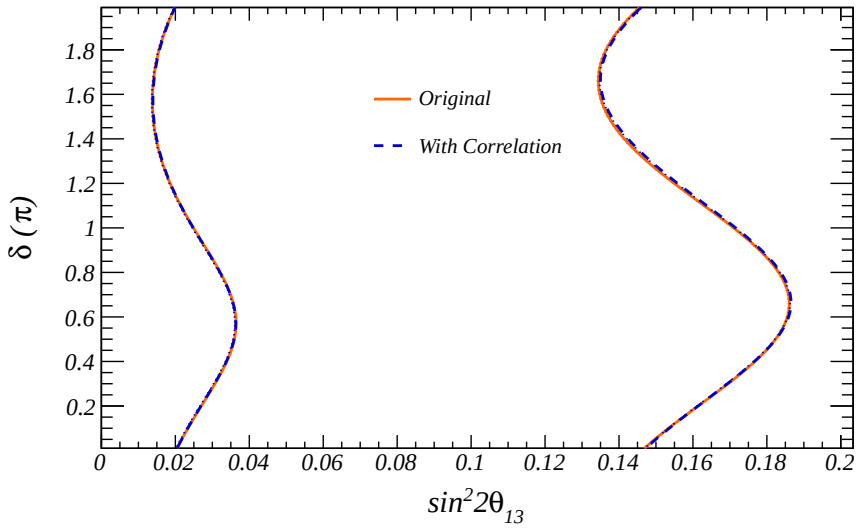


Figure 7.12: The effect of including a correlation between the total cross section error for T2K and the MINOS flux plus cross-section error. The 95% CL contour has a negligible shift.

is the total uncertainty (in number of events) in bin i. For T2K there a slight choice in numbers from [113], the largest fractional contribution is found using the systematic errors at $\sin^2 2\theta_{13} = 0$: total error 22.7% and cross-section error 14.0% giving $c_{\text{xsec}} = 0.617\,\sigma$. The total error that is included for the correlations between the T2K bin and the three (LEM) low energy MINOS bins is thus $0.080\,\sigma^{\text{T2K}}\sigma_i^{\text{MINOS}}$.

Running the analysis with and without these worst-case correlations included, negligible difference in the results were found, as can be seen in Figure 7.12. This means that we can neglect correlated errors for the MINOS-T2K combination at this point, though this may not be true for later data sets, if cross-section errors assume a greater relative importance. For different combinations of experiments, correlated systematic errors may become important, and this is discussed in Section 7.8. In addition, when greater sensitivity is reached, the errors on the other oscillation parameters (which are of course cor-

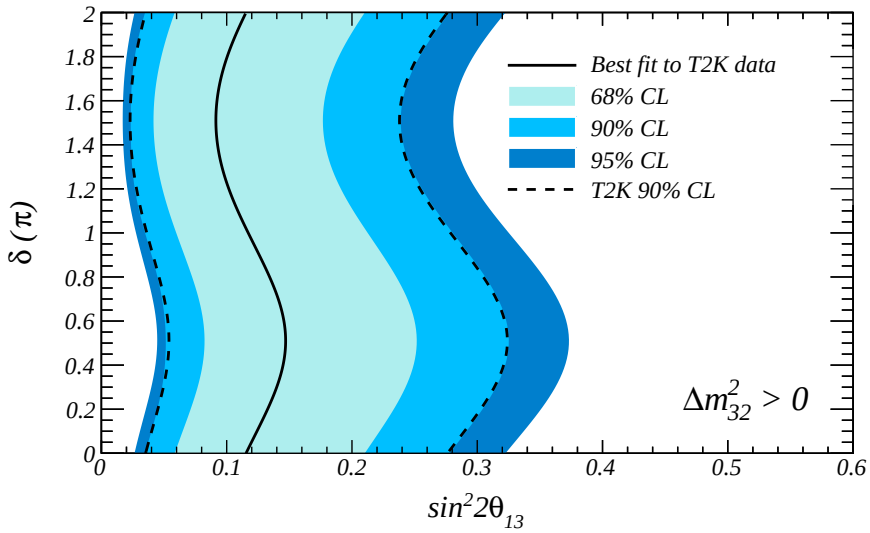


Figure 7.13: Reproduction of the T2K results: we find good agreement with the published contours [113]. In addition, we exclude $\sin^2 2\theta_{13} = 0$ at 2.5σ.

related) must also be considered.

7.6 Reproducing the Individual Results

Before combining the two datasets, the individual results of MINOS and T2K were reproduced by just providing one experiment as the input to the combination code. The validation results are shown in Figures 7.13 and 7.14, for T2K and MINOS respectively. In both cases, there is very good agreement with the published contours.

For the T2K results, neither δ nor the systematic errors are minimised over in the likelihood function, as with the original T2K analysis. Small differences might be expected as T2K do not assume that the error on the number of events is Gaussian, whereas this analysis does; however, these differences appear negligible.

For MINOS, δ was not minimised over, but the systematic errors were min-

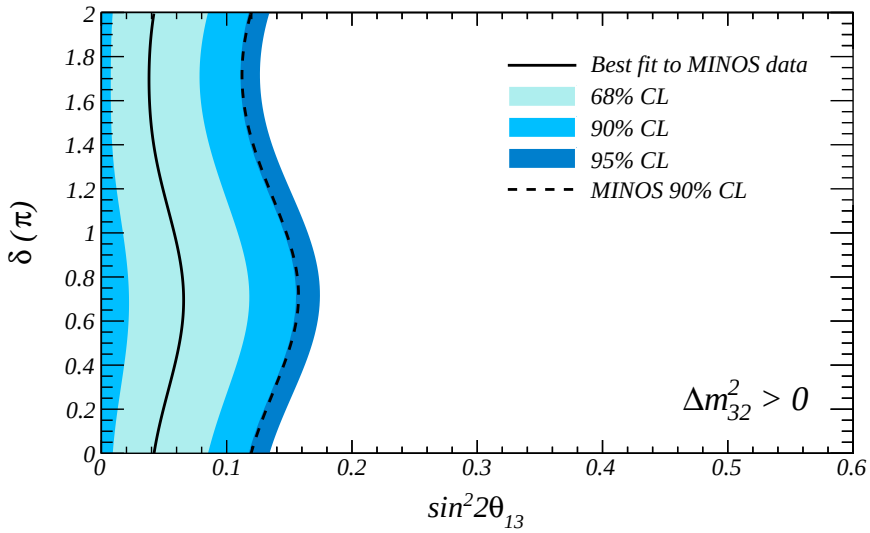


Figure 7.14: Reproduction of the MINOS results: we find good agreement with the published contours [129].

imised in the likelihood function, as in the original MINOS analysis. Differences might be expected as the MINOS 90% contour shown in Figure 7.14 has $2\sin^2\theta_{23}\sin^2 2\theta_{13}$ as its x-axis rather than $\sin^2 2\theta_{13}$, as discussed in Section 7.5.1, and other oscillation parameters are fixed in this analysis. The difference from the published contour is still not significant.

7.7 Combined Fit Results

As previously mentioned, we take the profile likelihood, minimising over systematic errors, in our final fit. We also minimise over δ when calculating the minimum value of our likelihood function, since the combination of the two experiments gives slight sensitivity to $\mathcal{CP}$-violation. Two-dimensional confidence intervals are shown in Figure 7.15. No values of δ can be ruled out at 1σ. The best fit values of the oscillation parameters are $\sin^2 2\theta_{13} = 0.08\,(0.11)$ and $\delta = 1.1\,(2.0)\pi$ for the normal (inverted) neutrino mass hierarchy. Our best fit

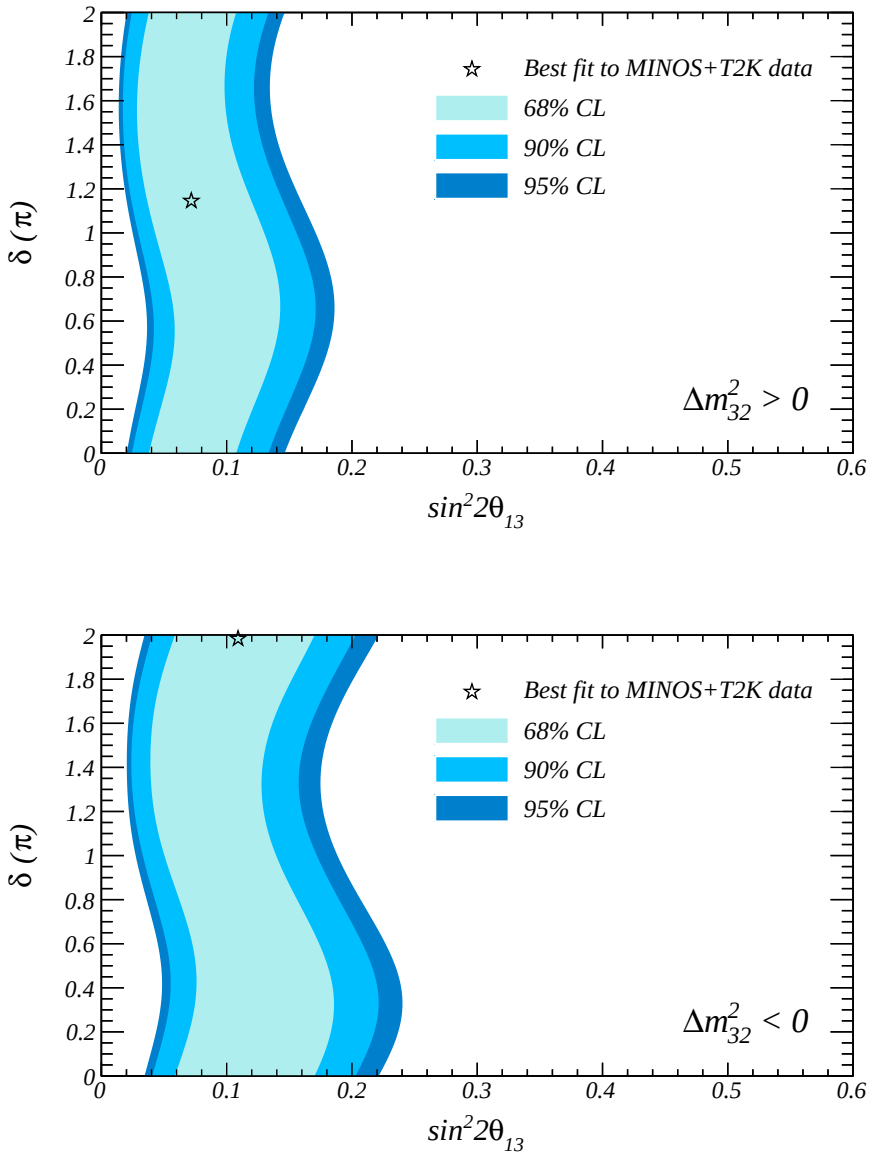


Figure 7.15: The Feldman Cousins 68%, 90% and 95% confidence level contours for the combined electron neutrino appearance measurement of T2K and MINOS, for normal (top) and inverted neutrino mass hierarchies. We exclude $\sin^2 2\theta_{13} = 0$ at 2.7σ, in the normal hierarchy.

value is compatible with the results presented in [136].

7.7.1 Significance of Excluding $\sin^2 2\theta_{13} = 0$

To work out the significance of excluding $\sin^2 2\theta_{13} = 0$, within the Feldman-Cousins method, it is necessary to generate a large number of toy experiments about $\sin^2 2\theta_{13} = 0$ (the oscillation probability is independent of δ if $\theta_{13} = 0$). These toy experiments then have their true and best fit log-likelihoods found in the usual manner, and are ordered in terms of their $\Delta \log \mathcal{L}$. Then the difference in log-likelihood between the best fit point to the data and the log-likelihood at $\theta_{13} = 0$ is used as the cut off in this ordering. The fraction of events below this cut off is the probability that our result is not consistent with $\sin^2 2\theta_{13} = 0$. For illustration, this probability is also converted to a normal quantile (how may standard deviations, σ, away from the mean of a normal distribution correspond to a (one-sided) tail area of one minus the probability of exclusion).

We exclude $\sin^2 2\theta_{13} = 0$ at 2.7σ (99.7% CL) (2.8σ (99.8% CL)) for the normal (inverted) neutrino mass hierarchy.

7.7.2 Finding the Limits on $\sin^2 2\theta_{13}$

In order to find limits on the quantity $\sin^2 2\theta_{13}$, rather than two-dimensional confidence level allowed regions, we need to remove the dependence on δ. This is done by taking the profile likelihood over δ, that is, for every value of $\sin^2 2\theta_{13}$, the value of the log-likelihood is found by minimising over δ as well as the other nuisance parameters. This procedure must also be followed when calculating the values of the critical delta log-likelihood at each value of $\sin^2 2\theta_{13}$, whilst throwing δ uniformly across $[0, 2\pi)$ in the toy experiments. The new values of $\Delta \log L_{\text{crit}}$ and $\Delta \log L_{\text{data}}$ for the 95% CL can be seen in Figure 7.16.

We find allowed regions of: $0.02\,(0.03) < \sin^2 2\theta_{13} < 0.16\,(0.21)$ at 95% CL, $0.03\,(0.04) < \sin^2 2\theta_{13} < 0.15\,(0.19)$ at 90% CL, and $0.04\,(0.05) < \sin^2 2\theta_{13} < 0.12\,(0.16)$ at 68% CL, for the normal (inverted) neutrino mass hierarchy.

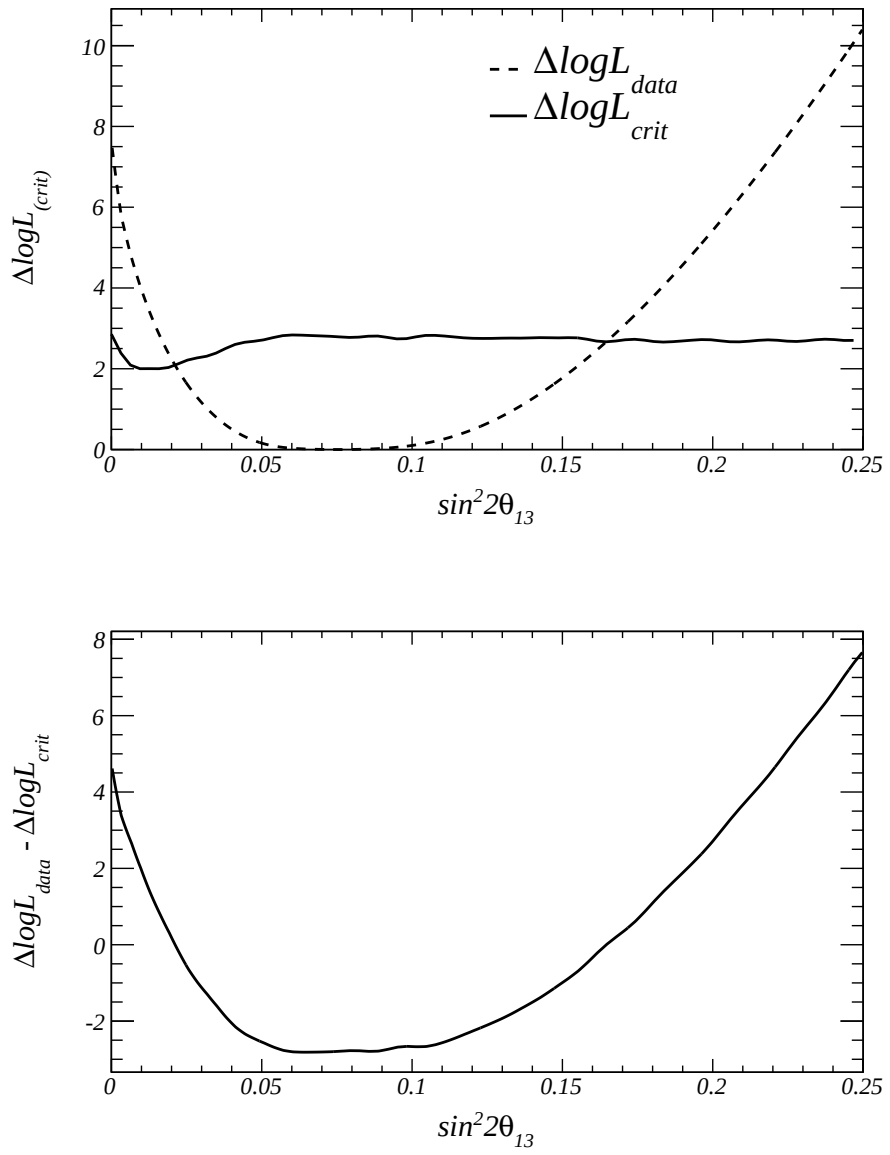


Figure 7.16: The $\Delta \log \mathcal{L}$ curves for the data and the critical values (95% CL) after taking the profile likelihood over δ, for the normal neutrino mass hierarchy. In the top plot both are shown, in the bottom plot the difference between the two is shown. The allowed region for $\sin^2 2\theta_{13}$, at 95% CL, is wherever the difference is below zero.

7.7.3 Working out Significance of Mass Hierarchy Preference

For the MINOS+T2K combined analysis, there are two different best fit points, one assuming the "normal" neutrino mass hierarchy, $\Delta m^2_{32} > 0$ (where $\Delta m^2_{21} > 0$ is assumed), and one for the "inverted" neutrino mass hierarchy, with $\Delta m^2_{32} < 0$. In this combination, the best fit point assuming the inverted neutrino mass hierarchy is actually slightly lower in $\Delta \log L$. To work out whether this measurement has any significance, a large number of toy experiments were generated about the best fit point, assuming the inverted neutrino mass hierarchy. Each of these toy experiments was then fit to the normal and inverted neutrino mass hierarchies, to see which was preferred. The fraction of the time that a better fit to the toy experiment was found using the inverted mass hierarchy was found to be almost exactly equal to that using the normal mass hierarchy, therefore the significance of the mass hierarchy preference is negligible.

7.7.4 Comparison to fixed $\Delta \log \mathcal{L}$ Elevation Contours

For comparison, in Figure 7.17 we show the contours that would be obtained by selecting an allowed region using a fixed value of $\Delta(2 \log \mathcal{L})$. The regions obtained using the Feldman-Cousins approach are significantly narrower than those from the fixed log-likelihood contours. Differences in the critical values of $\Delta(2 \log \mathcal{L})$ from the fixed elevation approximations can be seen in Figure 7.18. One of the reasons for these differences is that the value of $\sin^2 2\theta_{13}$ is close to the physical boundary at zero. Another reason for the differences could be that there is only a very weak dependence on δ, which means that the fixed $\Delta \log \mathcal{L}$ elevation contours could instead by drawn at the one rather than two dimensional values.

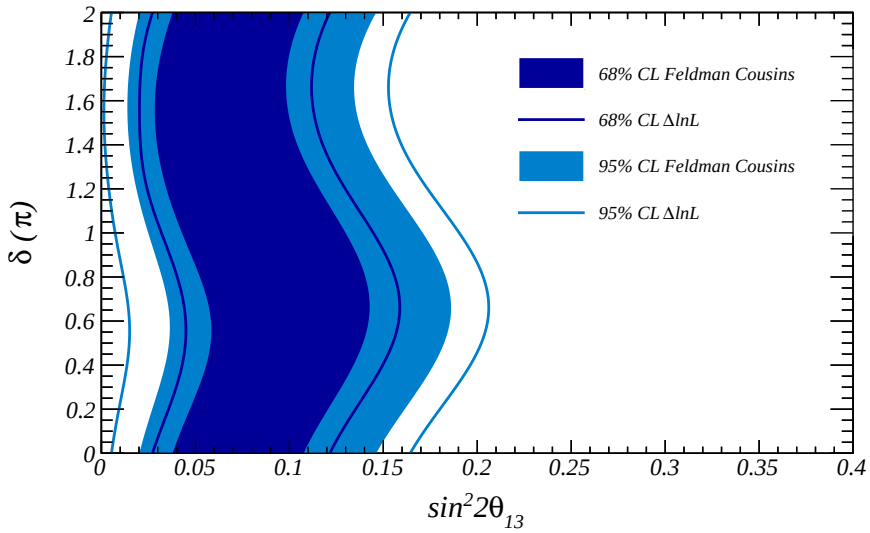


Figure 7.17: The Feldman-Cousins confidence intervals and those obtained by placing the contour at a fixed $\Delta(2\log\mathcal{L})$ elevation. Shown here are the 95% CL allowed region (and corresponding $\Delta(2\log\mathcal{L}) = 5.99$ contour) and 68% CL allowed region (and corresponding $\Delta(2\log\mathcal{L}) = 2.30$ contour). The Feldman-Cousins allowed regions are significantly narrower than those formed using fixed $\Delta(2\log\mathcal{L})$ elevations.

7.8 Inclusion of Other Experiments

It should be noted for the future that whilst one reactor experiment could be combined with MINOS and T2K without needing to account for correlations (very different energies, flux, baseline *etc.*), if multiple reactor experiments were to be included some effort would be needed to calculate the correlations between their errors. The same would be true if another long-baseline neutrino experiment with similar peak neutrino energy as either MINOS or T2K were to be included. In addition, as the measurement of θ_{13} improves, the errors on the measurement of the other oscillation parameters, which are of course correlated between all experiments, may start to become significant and would need to be included.

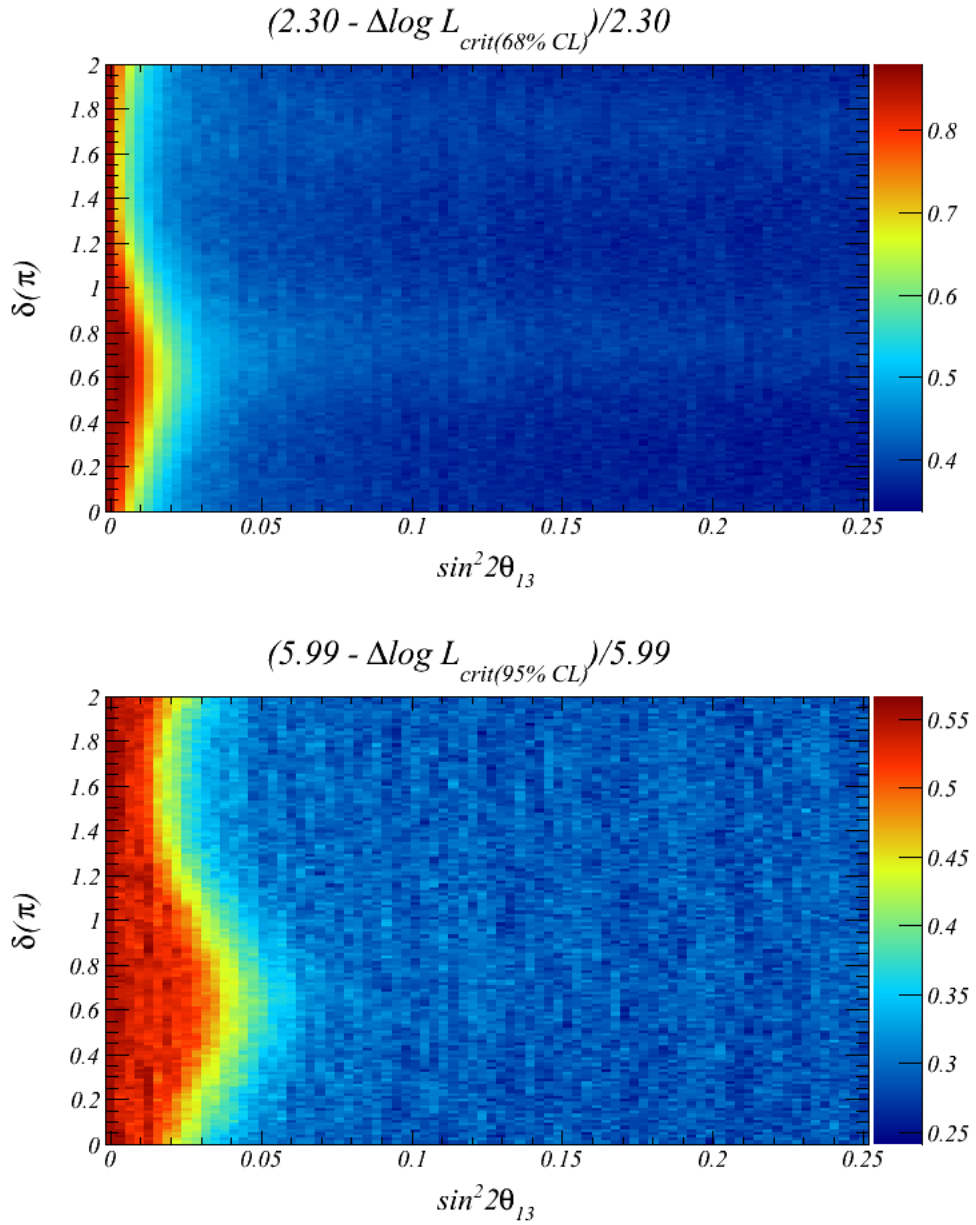


Figure 7.18: The extent to which the critical values are not equal to their fixed elevation approximations. The top plot is for 68% confidence level, and the bottom plot is for 95% confidence level.

Chapter 8

Summary and Outlook

In this thesis, a number of different analyses using the T2K ν_e appearance data have been presented. In Chapter 5 the T2K far detector ν_e appearance results were used to limit neutrino oscillations involving an additional sterile neutrino in a 3+1 model. This analysis excludes part of the MiniBooNE/LSND preferred region of the short baseline oscillation parameter space, including the MiniBooNE best fit point, at 3 σ. This analysis is something that could be improved with more statistics from T2K. At the time of writing, no other such measurements had been performed. However, since this analysis was performed, another long-baseline neutrino oscillation experiment, ICARUS, has made a similar measurement [125]. In general, long-baseline neutrino oscillation experiments with wider beams in neutrino energy than T2K, will be better suited to this kind of measurement. This is due the fact that the entire high energy tail can participate in rapid oscillations driven by θ_{14}, causing a far larger signal than would be seen in a narrow-band beam.

In Chapter 6, the ND280 Tracker was used to perform a ν_e appearance measurement. The sensitivity with the current statistics is not competitive with MiniBooNE. The future sensitivity of the ND280 to ν_e appearance was also discussed. A number of improvements, especially using the ν_μ interactions in the

ND280 to constrain flux and cross-section errors, and including the PØD in the ν_e search, could be made. The ND280 is especially interesting for this search since events containing a single electron track can be distinguished from events containing a single γ in the tracker region.

In Chapter 7, the long-baseline ν_e appearance results of two experiments: MINOS and T2K, were combined using the Feldman-Cousins method. This resulted in tighter constraints on the allowed regions of the $(\sin^2 2\theta_{13}, \delta)$ parameter space, at the confidence levels considered. $\sin^2 2\theta_{13} = 0$ was excluded at $2.7\,\sigma$, for the normal neutrino mass hierarchy. This result has been published in [137].

The T2K Experiment will continue to take data, aiming to reach 5×10^{21} protons on target. The main T2K analyses: ν_e appearance and ν_μ disappearance, will be improved with more data. The future sensitivity to the neutrino mass hierarchy and $\mathcal{CP}$-violation is also currently being investigated.

Looking to the future, a number of long-baseline accelerator neutrino oscillation experiments have been proposed with the goal of searching for $\mathcal{CP}$-violation in neutrino oscillations in mind: LBNE [139], LAGUNA/LBNO [140] and Tokai to Hyper-Kamiokande [141]. These experiments propose more intense neutrino beams and massive (either water Čerenkov or liquid argon) far detectors. The sensitivity of such an experiment to $\mathcal{CP}$-violation is considered, specifically for Tokai to Hyper-Kamiokande, in [142]. With the discovery of non-zero θ_{13} and the possibility of $\mathcal{CP}$-violation, the physics of neutrino oscillations is entering an exciting era.

Bibliography

[1] W. Pauli, *"Liebe Radioaktive Damen und Herren"*, letter to physicists at Tübingen (1930), cited by A. Franklin, *"Are there really Neutrinos?"*, p. 71 (2000)

[2] J. Chadwick, *"Possible Existence of a Neutron"*, Nature 129, 312 (1932)

[3] J. Chadwick, *"The Existence of a Neutron"*, Proc. Royal Soc. A136, 692 (1932)

[4] E. Fermi, *"Versuch einer Theorie der β-Strahlen. I."*, Zeitschrift für Physik 88, 161 (1934)

[5] F. Reines and C. Cowan, *"Detection of the Free Neutrino"*, Phys. Rev. 92, 830 (1953)

[6] C. L. Cowan, F. Reines, F. B. Harrison, H. W. Kruse and A. D. McGuire, *"Detection of the Free Neutrino: A Confirmation"*, Science 124, 103 (1956)

[7] M. Goldhaber, L. Grodzins and A. W. Sunyar, *"Helicity of Neutrinos"*, Phys. Rev. 109, 1015 (1958)

[8] G. Danby *et al.*, *"Observation of High-Energy Neutrino Reactions and the Existence of Two Kinds of Neutrinos"*, Phys. Rev. Lett. 9, 36 (1962)

[9] The ALEPH, DELPHI, L3, OPAL Collaborations *et al.*, *"Precision Electroweak Measurements on the Z Resonance"*, Phys. Reports 427, 257 (2006)

[10] M. L. Perl *et al.*, *"Evidence for Anomalous Lepton Production in e^+e^- Annihilation"*, Phys. Rev. Lett. 35, 1489 (1975)

[11] K. Kodama *et al.* (DONUT Collaboration), *"Observation of Tau Neutrino Interactions"*, Phys. Lett. B 504, 218 (2001)

[12] J. N. Bahcall, *"Solar Neutrinos. I. Theoretical"*, Phys. Rev. Lett. 12, 300 (1964)

[13] R. Davis, D. S. Harmer and K. C. Hoffman, *"Search for Neutrinos from the Sun"*, Phys. Rev. Lett. 20, 1205 (1968)

[14] B. T. Cleveland *et al.*, *"Measurement of the Solar Neutrino Flux"*, The Astrophysical Journal 496, 505 (1998)

[15] National Research Council, *"Neutrino Astrophysics: A Research Briefing"*, Washington, DC: The National Academies Press 1 (1995)

[16] B. Pontecorvo, *"Inverse Beta Processes and Nonconservation of Lepton Charge"*, Sov. Phys. JETP 7, 172 (1958)

[17] Z. Maki, M. Nakagawa and S. Sakata, *"Remarks on the Unified Model of Elementary Particles"*, Prog. Theor. Phys. 28, 870 (1962)

[18] The SNO Collaboration, *"Direct Evidence for Neutrino Flavor Transformation from Neutral-Current Interactions in the Sudbury Neutrino Observatory"*, Phys. Rev. Lett. 89, 011301 (2002)

[19] The SNO Collaboration, *"The Sudbury Neutrino Observatory"*, Nucl. Instr. Meth. A 449, 172 (2000)

[20] Image from `http://www.lbl.gov/Science-Articles/archive/sudbury/sno2.html`

[21] C. Giunti and C. W. Kim, *"Fundamentals of Neutrino Physics and Astrophysics"*, p245, Oxford University Press (2007)

[22] C. Amsler *et al.*, *"Review of Particle Physics"*, Phys. Lett. B 667, 1 (2008)

[23] E. Akhmedov and J. Kopp, *"Neutrino Oscillations: Quantum Mechanics vs. Quantum Field Theory"*, Phys. Rev. D 82, 093003 (2010)

[24] L.-L. Chau and W.Y. Keung, *"Comments on the Parametrization of the Kobayashi-Maskawa Matrix"*, Phys. Rev. Lett. 53, 1802 (1984)

[25] L. Wolfenstein, *"Neutrino Oscillations in Matter"*, Phys. Rev. D 17, 2369 (1978)

[26] S. P. Mikheyev and A. Y. Smirnov, *"Resonance Amplification of Oscillations in Matter and Spectroscopy of Solar Neutrinos"*, Sov. J. Nucl. Phys. 42, 913 (1985)

[27] E. K. Akhmedov, *"Neutrino Oscillations: Theory and Phenomenology"*, arXiv:hep-ph/0610064v2, talk given at Neutrino 2006 (2006)

[28] C. Giunti and C. W. Kim, *"Fundamentals of Neutrino Physics and Astrophysics"*, p322 (2007)

[29] SNO Collaboration, *"Electron Energy Spectra, Fluxes, and Day-Night Asymmetries of ^8B Solar Neutrinos from the 391-Day Salt Phase SNO Data Set"*, Phys. Rev. C 72, 055502 (2005)

[30] S. Abe *et al.* (KamLAND Collaboration), *"Precision Measurement of Neutrino Oscillation Parameters with KamLAND"*, Phys. Rev. Lett. 100, 221803 (2008)

[31] The Super-Kamiokande Collaboration, *"Evidence for Oscillation of Atmospheric Neutrinos"*, Phys. Rev. Lett. 81, 1562 (1998)

[32] The Super-Kamiokande Collaboration, *"Evidence for an Oscillatory Signature in Atmospheric Neutrino Oscillation"*, Phys. Rev. Lett. 93, 101801 (2004)

[33] The Super-Kamiokande Collaboration, *"A Measurement of Atmospheric Neutrino Oscillation Parameters by Super-Kamiokande I"*, Phys. Rev. D 71, 112005 (2005)

[34] Y. Itow, *"Atmospheric Neutrinos: Results from Running Experiments"*, Talk at Neutrino 2012, Kyoto

[35] The Super-Kamiokande Collaboration, *"A Measurement of the Appearance of Atmospheric Tau Neutrinos by Super-Kamiokande"*, arXiv:1206.0328v1 [hep-ex] (2012)

[36] The OPERA Collaboration, *"Results from OPERA"*, Talk at Neutrino 2012, Kyoto

[37] The K2K collaboration, *"Measurement of Neutrino Oscillation by the K2K Experiment"*, Phys. Rev. D 74, 072003 (2006)

[38] P. Adamson *et al.* (MINOS Collaboration), *"Measurement of the Neutrino Mass Splitting and Flavor Mixing by MINOS"*, Phys.Rev.Lett. 106, 181801 (2011)

[39] P. Adamson *et al.* (MINOS Collaboration), *"First Direct Observation of Muon Antineutrino Disappearance"*, Phys. Rev. Lett. 107, 021801 (2011)

[40] R. Nichol for the MINOS Collaboration, *"Final MINOS Results"*, Talk at Neutrino 2012, Kyoto

[41] F. P. An *et al.* (Daya Bay Collaboration), *"Observation of Electron-Antineutrino Disappearance at Daya Bay"*, arXiv:1203.1669v1

[42] J. K. Ahn *et al.* (RENO Collaboration), *"Observation of Reactor Electron Antineutrino Disappearance in the RENO Experiment"*, arXiv:1204.0626v2

[43] T. Nakaya for the T2K Collaboration, *"New Results from T2K"*, Talk at Neutrino 2012, Kyoto

[44] D. Dwyer on behalf of the Daya Bay Collaboration, *"Improved Measurement of Electron-antineutrino Disappearance at Daya Bay"*, Talk at Neutrino 2012, Kyoto

[45] M. Ishitsuka for the Double Chooz Collaboration, *"Double Chooz Results"*, Talk at Neutrino 2012, Kyoto

[46] W. Pauli, *"Exclusion Principle, Lorentz Group and Reflection of Space-Time and Charge"*, from *"Niels Bohr and the Development of Physics"* Pergamon Press (1955)

[47] A. D. Sakharov, *"Violation of CP Invariance, C Asymmetry, and Baryon Asymmetry of the Universe"*, Pis'ma Zh. Eksp. Teor. Fis. 5, 32 (1967)

[48] C. Athanassopoulos *et al.* (LSND Collaboration), *"The Liquid Scintillator Neutrino Detector and LAMPF Neutrino Source"*, Nucl. Instrum. Meth. A 338, 149 (1997)

[49] A. Aguilar *et al.* (LSND Collaboration), *"Evidence for Neutrino Oscillations from the Observation of Electron Anti-neutrinos in a Muon Anti-Neutrino Beam"*, Phys. Rev. D 64, 112007 (2001)

[50] G. Drexlin, *"Final Neutrino Oscillation Results from LSND and KARMEN"*, Nucl. Phys. B (Proc. Suppl.) 118, 146 (2003)

[51] KARMEN Collaboration, *"Upper Limits for Neutrino Oscillations Muon-Antineutrino to Electron-Antineutrino from Muon Decay at Rest"*, Phys. Rev. D 65, 112001 (2002)

[52] E. D. Church *et al.*, *"Statistical Analysis of Different Muon-antineutrino $\rightarrow$ Electron-antineutrino Searches"*, Phys. Rev. D 66, 013001 (2002)

[53] MiniBooNE Collaboration, *"Event Excess in the MiniBooNE Search for $\overline{\nu}_\mu \rightarrow \overline{\nu}_e$ Oscillations"*, Phys. Rev. Lett. 105, 181801 (2010)

[54] C. Polly for the MiniBooNE Collaboration, *"Updated Oscillation Results from MiniBooNE"*, talk at Neutrino 2012, Kyoto

[55] G. Mention *et al.*, *"The Reactor Antineutrino Anomaly"*, Phys. Rev. D 83, 073006 (2011)

[56] F. Kaether *et al.*, *"Reanalysis of the* GALLEX *Solar Neutrino Flux and Source Experiments"*, Phys. Lett. B 685, 47 (2010)

[57] J. N. Abdurashitov *et al.*, *"Measurement of the Response of a Ga Solar Neutrino Experiment to Neutrinos from an ^{37}Ar Source"*, Phys. Rev. C 73, 045805 (2006)

[58] J. N. Abdurashitov *et al.* (SAGE Collaboration), *"Measurement of the Response of a Gallium Metal Solar Neutrino Experiment to Neutrinos from a ^{51}Cr Source"*, Phys. Rev. C 59, 2246 (1999)

[59] K. N. Abazajian *et al.*, *"Light Sterile Neutrinos: A White Paper"*, arXiv:1204.5379v1 [hep-ph]

[60] K. Assamagan *et al.*, *"Upper Limit of the Muon-Neutrino Mass and Charged-Pion Mass from Momentum Analysis of a Surface Muon Beam"*, Phys. Rev. D 53, 6065 (1996)

[61] ALEPH Collaboration, *"An Upper Limit on the τ Neutrino Mass from Three- and Five-Prong Tau Decays"*, Eur. Phys. J. C 2, 395 (1998)

[62] Ch. Kraus *et al.*, *"Final Results from Phase II of the Mainz Neutrino Mass Search in Tritium β Decay"*, Eur. Phys. J. C 40, 447 (2005)

[63] V. N. Aseev *et al.*, *"Upper Limit on the Electron Antineutrino Mass from the Troitsk Experiment"*, Phys. Rev. D 84, 112003 (2011)

[64] A. Osipowicz *et al.*, *"KATRIN: A Next Generation Tritium Beta Decay Experiment with sub-eV Sensitivity for the Electron Neutrino Mass"*, KATRIN Letter of Intent, arXiv:hep-ex/0109033v1

[65] J. Wilkerson, *"A Review of the Direct Neutrino Mass Experiments"*, Talk at Neutrino 2012, Kyoto

[66] C. Giunti and C. W. Kim, *"Fundamentals of Neutrino Physics and Astrophysics"*, p484, Oxford University Press (2007)

[67] H. V. Klapdor-Kleingrothaus, A. Dietz, H. L. Harney and I. V. Krivosheina, *"Evidence for Neutrinoless Double Beta Decay"*, Mod. Phys. Lett. A 16, 2409 (2001)

[68] H. V. Klapdor-Kleingrothaus, I. V. Krivosheina, A. Dietz and O. Chkvorets, *"Search for Neutrinoless Double Beta Decay with Enriched ^{76}Ge in Gran Sasso 1990-2003"*, Phys. Lett. B 586, 198 (2004)

[69] H. V. Klapdor-Kleingrothaus and I. V. Krivosheina, *"The Evidence for the Observation of $0\nu\beta\beta$ Decay: the Identification of $0\nu\beta\beta$ Events from the Full Spectra"*, Mod. Phys. Lett. A 21, 1547 (2006)

[70] C. E. Aalseth *et al.*, *"Comment on "Evidence for Neutrinoless Double Beta Decay" "*, Mod. Phys. Lett. A 17, 1475 (2002)

[71] H. L. Harney, *"Reply to the Comment on "Evidence for Neutrinoless Double Beta Decay" "*, Mod. Phys. Lett. A 16, 2409 (2001)

[72] A. M. Bakalyarov *et al.*, *"Results of the Experiment on Investigation of Germanium-76 Double Beta Decay. Experimental Data of the Heidelberg-Moscow Collaboration November 1995 - August 2001"*, Phys. Part. Nucl. Lett. 2, 77 (2005)

[73] C. E. Aalseth *et al.*, *"The IGEX ^{76}Ge Neutrinoless Double Beta Decay Experiment: Prospects for Next Generation Experiments"*, Phys. Rev. D 65, 092007 (2002)

[74] KamLAND-Zen Collaboration, *"Limits on Majoron-Emitting Double-Beta Decays of Xe-136 in KamLAND-Zen"*, arXiv:1205.6372v1 [hep-ex]

[75] M. Auger *et al.* (EXO Collaboration), *"Search for Neutrinoless Double-Beta Decay in ^{136}Xe with EXO-200"*, arXiv:1205.5608v1 [hep-ex]

[76] F. Alessandria *et al.* (CUORE Collaboration), *"Sensitivity of CUORE to Neutrinoless Double-Beta Decay"*, arXiv:1109.0494v2 [nucl-ex]

[77] I. Abt *et al.*, *"A New ^{76}Ge Double Beta Decay Experiment at LNGS"*, The GERDA Letter of Intent, arXiv:hep-ex/0404039v1

[78] C. Giunti and C. W. Kim, *"Fundamentals of Neutrino Physics and Astrophysics"*, p511 (2007)

[79] K. S. Hirata *et al.*, *"Observation in the Kamiokande-II Detector of the Neutrino Burst from Supernova SN1987A"*, Phys. Rev. D 38, 448 (1988)

[80] T. Haines *et al.* (IMB Collaboration), *"Neutrinos from SN1987A in the IMB Detector"*, Nucl. Instr. Meth. A 264, 28 (1988)

[81] A. E. Chudakov, Y. S. Elensky and S. P. Mikheev, *"Characteristics of the Neutrino Emission from Supernova SN1987A"*, JETP Lett. 46, 373 (1987)

[82] T. J. Loredo and D. Q. Lamb, *"Bayesian Analysis of Neutrinos Observed from Supernova SN 1987A"*, Phys. Rev. D 65, 063002 (2002)

[83] M. J. Longo, *"Tests of Relativity from SN1987A"*, Phys. Rev. D 36, 3276 (1987)

[84] T. Adam *et al.* (OPERA Collaboration), *"Measurement of the Neutrino Velocity with the OPERA Detector in the CNGS Beam"*, arXiv:1109.4897v2 [hep-ex] (2011)

[85] P. Adamson *et al.* (MINOS Collaboration), *"Measurement of Neutrino Velocity with the MINOS Detectors and NuMI Neutrino Beam"*, Phys. Rev. D 76, 072005 (2007)

[86] P. Adamson, *"Neutrino Velocity: Results and Prospects of Experiments at other Beamlines"*, talk at Neutrino 2012, Kyoto

[87] M. Dracos for the OPERA Collaboration, *"The Neutrino Velocity Measurement by OPERA Experiment"*, talk at Neutrino 2012, Kyoto

[88] G. R. Kalbfleisch *et al.*, *"Experimental Comparison of Neutrino, Antineutrino, and Muon Velocities"*, Phys. Rev. Lett. 43, 1362 (1979)

[89] Y. Itow *et al.*, *"The JHF-Kamioka Neutrino Project"*, arXiv:hep-ex/0106019v1

[90] Y. Hayato *et al.*, *"Letter of Intent: Neutrino Oscillation Experiment at JHF"*, T2K LOI `http://neutrino.kek.jp/jhfnu/loi/-loi.v2.030528.pdf`

[91] K. Abe *et al.* (T2K Collaboration), *"The T2K Experiment"*, Nucl. Instrum. Meth. A 659, 1, 106-135 (2011)

[92] A.Vacheret *et al.*, *"The Front End Readout System for the T2K-ND280 Detectors"*, NSS '07 IEEE, 6 (2007)

[93] Hamamatsu Photonics, Japan, `http://jp.hamamatsu.com/products/sensor-ssd/4010/index_en.html`

[94] A. Vacheret *et al.*, *"Characterization and Simulation of the Response of Multi Pixel Photon Counters to Low Light Levels"*, Nucl. Instrum. Meth. A 656, 69 (2011)

[95] D. Beavis, A. Carroll, I. Chiang *et al.*, *"Long Baseline Neutrino Oscillation Experiment at the AGS. Physics Design Report"*, Proposal E889, BNL 52459 (1995)

[96] A. K. Ichikawa, private communications

[97] D.G. Michael *et al.* (MINOS Collaboration), *"Observation of Muon Neutrino Disappearance with the MINOS Detectors in the NuMI Neutrino Beam"*, Phys. Rev. Lett. 97, 191801 (2006)

[98] N. Abgrall *et al.*, *"Time Projection Chambers for the T2K Near Detectors"*, Nucl. Instrum. Meth. A 637, 25 (2011)

[99] P.-A. Amaudruz, *et al.*, *"The T2K Fine-Grained Detectors"*, Nucl. Instrum. Meth. A 2012.08.020 (2012)

[100] N. Abgrall *et al.*, *"Report from the NA61/SHINE Experiment at the CERN SPS"*, Technical Report CERN-SPSC-2010-025. SPSC-SR-066, CERN, Geneva (2010)

[101] N. Abgrall *et al.*, *"Measurements of Cross Sections and Charged Pion Spectra in Proton-Carbon Interactions at 31 GeV/c"*, CERN-PH-EP-2011-005 (2011)

[102] FLUKA version 2008.3c, `http://www.fluka.org/fluka.php` (2008)

[103] GEANT3, A detector description and simulation tool, Application Software Group, Computing and Networks Division, CERN, Geneva (1993)

[104] R. Brun, A. Gheata and M. Gheata, *"The ROOT Geometry Package"*, Nucl. Instrum. Meth. A 502, 676 (2003)

[105] C. Andreopoulos *et al.*, *"The GENIE Neutrino Monte Carlo Generator"*, Nucl. Instrum. Meth. A 614, 87 (2010)

[106] Y. Hayato, *"A Neutrino Interaction Simulation Program Library NEUT"*, Acta Phys. Polon. B 40, 2477 (2009)

[107] C. Zeitnitz and T. Gabriel, *"The GEANT-CALOR Interface and Benchmark Calculations of ZEUS Test Calorimeters"*, Nucl. Instrum. Meth. A 349, 106 (1994)

[108] M. Nakahata *et al.*, *"Atmospheric Neutrino Background and Pion Nuclear Effect for KAMIOKA Nucleon Decay Experiment"*, J. Phys. Soc. Jap. 55, 3786 (1986)

[109] T2K Collaboration, Blessed Plots `http://www.t2k.org/docs/-plots/001/` (2010)

[110] T2K Collaboration, Blessed Plots `http://www.t2k.org/docs/-plots/011/nue/nueoscillation` (2011)

[111] T2K Collaboration, Blessed Plots `http://www.t2k.org/docs/-plots/011/numu/numuruthoxlan`

[112] T2K Collaboration, *"First Muon Neutrino Disappearance Study with an Off-Axis Beam"*, arXiv:1201.1386v1 [hep-ex]

[113] K. Abe *et al.* (T2K Collaboration), *"Indication of Electron Neutrino Appearance from an Accelerator-produced Off-axis Muon Neutrino Beam"*, Phys.Rev.Lett.107:041801 (2011)

[114] P. Rubinov, *"D-Zero Central Fiber Tracker AFEII Analog Front End Board Design Specification"*, D0 note (2005)

[115] L. Bellantoni and P. Rubinov, *"Bench Test of TRIP-t"*, D0 note

[116] M. Noy, *"Trip-T Front End Board Documentation"*, http://www.hep.ph.ic.ac.uk/∼dmray/TFB_documentation/

[117] The MINOS Collaboration, *"Search for Sterile Neutrino Mixing in the MINOS Long-Baseline Experiment"*, Phys. Rev. D 81, 052004 (2010)

[118] P. Huber, M. Lindner and W. Winter, *"Simulation of Long-Baseline Neutrino Oscillation Experiments with GLoBES"*, Comput. Phys. Commun. 167, 195, arXiv:hep-ph/0407333 (2005)

[119] P. Huber *et al.*, *"New Features in the Simulation of Neutrino Oscillation Experiments with GLoBES 3.0"*, Comput. Phys. Commun. 177, 432, arXiv:hep-ph/0701187 (2007)

[120] A. A. Aguilar-Arevalo *et al.* (MiniBooNE Collaboration), *"A Combined $\nu_\mu \rightarrow \nu_e$ and $\overline{\nu}_\mu \rightarrow \overline{\nu}_e$ Oscillation Analysis of the MiniBooNE Excesses"*, arXiv:1207.4809v1 [hep-ex] (2012)

[121] C. Giganti and M. Zito, *"Particle Identification with the T2K TPC"*, T2K Technical Note 1 (2009)

[122] E. J. Moniz *et al.*, *"Nuclear Fermi Momenta from Quasielastic Electron Scattering"*, Phys. Rev. Lett. 26, 8, 445 (1971)

[123] G. Zandt and C. J. Ammon, *"Continental Crust Composition Constrained by Measurements of Crustal Poisson's Ratio"*, Nature 374, 152 (1995)

[124] J. Caravaca *et al.*, *"Measurement of the ν_e Beam Component using the ND280 Tracker"*, T2K Technical Note 94 (2012)

[125] M. Antonello *et al.*, *"Experimental Search for the LSND Anomaly with the ICARUS LAr TPC Detector in the CNGS Beam"*, arXiv:1209.0122v1 [hep-ex] (2012)

[126] C. J. Backhouse, private communications.

[127] G. J. Feldman and R. D. Cousins, *"Unified Approach to the Classical Statistical Analysis of Small Signals"*, Phys. Rev. D 57:3873-3889 (1998)

[128] P. Adamson *et al.* (MINOS Collaboration), *"The Magnetized Steel and Scintillator Calorimeters of the MINOS Experiment"*, Nucl. Instrum. Meth. A 596, 2, 190-228 (2008)

[129] P. Adamson *et al.* (MINOS Collaboration), *"Improved Search for Muon-neutrino to Electron-neutrino Oscillations in MINOS"*, Phys. Rev. Lett. 107, 181802 (2011)

[130] P. Adamson *et al.* (MINOS Collaboration), *"New Constraints on Muon-neutrino to Elecron-neutrino Transitions in MINOS"*, Phy.Rev.(Rapid Communications) D82:051102 (2010)

[131] The UCL MINOS webpage, `http://www.hep.ucl.ac.uk/minos/`

[132] MINOS Press Releases, `http://www.fnal.gov/pub/presspass/-press_releases/NuMI_photos/`

[133] Particle Data Group, *"Review of Particle Physics"*, Phys. Lett. B 667, 1-5, Section on Statistics, p320 (2008)

[134] W.H. Press, S.A. Teukolsky, W.T. Vetterling and B.P. Flannery, *"Numerical Recipes in C++ (Second Edition)"*, 99-101 (2002)

[135] R. Brun and F. Rademakers, *"ROOT - An Object Oriented Data Analysis Framework"*, Proc. AIHENP'96 Workshop, Lausanne, Sep. 1996, Nucl. Instrum. Meth. in Phys. Res. A 389 81-86 (1997), see also `http://root.cern.ch/`

[136] T. Schwetz, M. Tórtola and J. W. F. Valle, *"Where we are on θ_{13}: Addendum to "Global Neutrino Data and Recent Reactor Fluxes: Status of Three-Flavour Oscillation Parameters" "*, arXiv:1108.1376v1 [hep-ph] (2011)

[137] A. V. Waldron, M. D. Haigh and A. Weber, *"Combining Neutrino Oscillation Experiments with the Feldman-Cousins Method"*, New J. Phys. 14, 063037 (2012)

[138] NOνA Collaboration, *"NuMI Off-Axis ν_e Appearance Experiment: Technical Design Report"*, `http://www-nova.fnal.gov/nova_cd2_review/tdr_oct_23/tdr.htm`

[139] LBNE Collaboration, *"CDR: The LBNE Project"*, `http://lbne.fnal.gov/papers.shtml`

[140] LAGUNA Collaboration, *"The LAGUNA Design Study- Towards Giant Liquid based Underground Detectors for Neutrino Physics and Astrophysics and Proton Decay Searches"*, arXiv:1001.0077v1 [physics.ins-det]

[141] Hyper-Kamiokande Working Group, *"Letter of Intent: The Hyper-Kamiokande Experiment — Detector Design and Physics Potential —"*, arXiv:1109.3262v1 [hep-ex]

[142] T. Schwetz, *"What is the Probability that θ_{13} and CP Violation will be Discovered in Future Neutrino Oscillation Experiments?"*, Phys. Lett. B 648, 54 (2007)